Assessing quantitative methane leak monitoring capabilities using geostationary satellite data

Master of Science Thesis Report

Ties Maarten Rozema

Delft University of Technology | SRON

TU Delft

SRON
Netherlands Institute for Space Research

Front cover artwork:
Methane Leaks - Seeking Accurate Reports by Alisa Singer, www.environmentalgraphiti.org © 2021 Alisa Singer.

Assessing quantitative methane leak monitoring capabilities using geostationary satellite data

Master of Science Thesis Report

by

Ties Maarten Rozema

to obtain the degree of Master of Science
at the faculty of Aerospace Engineering
of Delft University of Technology,
to be defended publicly on February 4, 2025.

Student number:	4672496	
Project duration:	January 2024 – February 2025	
Assessment committee:	Prof. dr. J.G. De Teixeira da Encarnacao	TU Delft supervisor
	Dr. M. Dogniaux	SRON supervisor
	Dr. J.D. Maasakkers	SRON supervisor
	Prof. dr. L.L.A. Vermeersen	Chair
	Ir. M.C. Naije	Examiner
	Ir. L.H. Svedhem	External

This thesis is confidential and cannot be made public until February 4, 2027.

TU Delft

SRON
Netherlands Institute for Space Research

Acknowledgements

My Master's thesis marks the end of my journey as a student at TU Delft and as a thesis student at SRON. My student career started seven and a half years ago and it is safe to say it has been a transformational adventure. At the start of my Master's, I felt a desire to work on a relevant and valuable topic for my thesis, and I feel thankful to have had this opportunity at SRON. Being part of a world-class scientific research institute has been an invaluable and rewarding experience. Looking ahead, I am filled with the belief that my time at TU Delft has prepared me to be an engineer who can solve pressing problems. Whatever the future holds, new doors will always open when others close.

I would like to use this space to express my profound gratitude to those people who have played a crucial role in my journey, and without whom this work could not have been completed. First, I want to sincerely thank Dr. Matthieu Dogniaux. I am glad I have had the opportunity to learn from you, and your methodological approach to dissecting complex problems has taught me valuable lessons that I will take with me in all my future endeavors. Your guidance and insight have been incredibly helpful in navigating any issues during my thesis. I also want to express my deep gratitude to Dr. Bram Maasakkers. Your in-depth understanding of all aspects that make methane detection and quantification possible has repeatedly amazed me and your insights have always steered me to valuable steps. I am also grateful to Prof. Dr. João De Teixeira da Encarnacao for his guidance and support. You took me on as a thesis student even though you had no prior knowledge of methane detection, for which I am grateful. Your in-depth feedback has been invaluable to my thesis. I also want to thank all my fellow interns and colleagues in SRON's Earth group for the conversations and discussions during coffee breaks and lunches that helped me contextualize the field of methane remote sensing. A special thanks to Berend Schuit, Tobias de Jong, Shubham Sharma, Xin Zhang and Clayton Roberts of the L4 team.

Next, I want to thank all my friends who I met in Delft. You are all brilliant, motivating, hard-working and visionary people who have helped me grow as a person. I have been blessed to meet all of you. Thank you for being great people and amazing friends.

Lastly, I want to thank my father, mother and two brothers. Thank you for raising, helping, guiding, motivating and supporting me since day one. You are always there for me, no matter the circumstances, and your support means the world to me. I would never have been able to do this without you. Thank you for everything.

Lastly, I hope all interested readers find this report insightful and useful. If you plan on continuing methane leak monitoring with geostationary satellites, I wish you luck!

Ties Rozema
Leiden & Delft, January 2025

"It seems to me that the natural world is
the greatest source of excitement;
the greatest source of visual beauty,
the greatest source of intellectual interest.
It is the greatest source of so much in
life that makes life worth living."

— SIR DAVID ATTENBOROUGH (1926)

Abstract

Methane is a strong yet short-lived greenhouse gas that is responsible for roughly one-quarter of total global warming since preindustrial times. It is emitted by various natural and anthropogenic sources, including oil & gas facilities, coal mines, biomass burning, ruminants and rice paddies. It is the primary constituent of natural gas and frequently leaks from oil & gas infrastructure through deteriorating pipelines, oil wells, storage facilities and processing plants. These leaks form areas of enhanced methane concentrations that travel with the wind direction away from a point source called plumes. Due to its potency, preventing methane emissions from anthropogenic sources presents an opportunity for effective climate change mitigation.

Methane strongly absorbs infrared radiation, which allows methane-sensitive satellite instruments to detect and quantify methane plumes by observing reflected sunlight. The current satellite fleet is almost entirely in sun-synchronous, low-Earth orbits with constant overpass times between 09:30 and 14:30 (local time) and one overpass per day. This means that emissions after 14:30 and emissions from intermittent sources cannot be detected or quantified. In November 2023, [1] demonstrated the ability of NASA's geostationary weather satellite GOES-16 to detect methane leaks. GOES-16 has five-minute coverage of the contiguous United States, which, in principle, allows for detecting brief emissions from intermittent sources. However, GOES-16 was not designed for methane detection and thus has a very low sensitivity, which makes detecting emissions challenging.

Since GOES-16 is a new instrument in the field of methane emission detection, its methane detection and quantification capabilities are not yet characterized in detail. The objectives of this thesis are to assess how accurately GOES can quantify methane emissions and to investigate how its detection limit varies under environmental conditions. This provides an in-depth understanding of when and where GOES-16 can be used to detect methane emissions. The novelty of this thesis is not in inventing a new methodology to detect and quantify methane emissions, but rather in verifying the existing methodologies and applying them to characterize, quantify and understand the methane-sensing capabilities of a repurposed satellite.

Methane plume simulations are created using an atmospheric transport modeling tool. By applying a forward radiative transfer model, the simulated concentrations are converted into radiances in the spectral bands of GOES-16. These simulated radiances are then used to retrieve back the methane concentrations. By comparing the simulated and retrieved enhancements, GOES-16's methane retrieval capabilities are assessed. The total methane mass and source rate of the plumes are also quantified and compared to the simulation. By determining which simulated plumes are successfully detected and which are missed with empirically defined detectability metrics, a probability of detection curve is derived that describes the probability of detecting a plume under certain environmental conditions. This is important to understand GOES' efficacy for methane plume detection by determining which plumes it is likely and unlikely detect.

The results show that GOES-16 can accurately retrieve and quantify methane concentrations under realistic conditions, with high probabilities of detection at low wind speeds under favorable environmental conditions (small pixel size and bright albedo). However, masking the plume from the retrieved enhancements is very challenging for low to medium source rates due to high noise levels. These noise levels increase for unfavorable conditions and make plume masking a limiting factor in the quantification accuracy. The automated detectability metrics, which directly influence the derived probabilities of detection, sometimes incorrectly assess the detection success, leading to non-physical probabilities under unfavorable conditions. The plume detectability was also determined by visual inspection. This resulted in physical probability of detection curves that showed a trend of decreasing probability for increasing pixel size. A similar trend was expected but not observed for darkening albedo due to complex retrievals with significant artefacts and high noise levels. The synthetic probability of detection curves were validated by comparing them to real-life source rate quantifications of methane leaks by TROPOMI and by GOES. These comparisons demonstrated a strong agreement between both.

These results imply that GOES-16 can be used to accurately quantify and observe temporal variability in methane emissions under favorable conditions. An important area of improvement in the methodology is to decrease the sensitivity of the retrieval to the selected reference day and plume masking thresholds. This opens up possibilities for other research questions, such as comparing the quantification results of methane plumes to other satellites to reduce uncertainties and, eventually, developing a near-real-time plume detection capability in the contiguous United States.

Contents

List of Figures

List of Tables

Nomenclature

Abbreviations

Abbreviation	Definition
ABI	Advanced Baseline Imager
AGAGE	Advanced Global Atmospheric Gases Experiment
AWS	Amazon Web Services
B5	(Spectral) Band 5
B6	(Spectral) Band 6
CDF	Cumulative distribution function
CH_4	Methane
CONUS	Contiguous United States
COP	Conference of the Parties
CSF	Cross-sectional flux
CSIRO	Commonwealth Scientific and Industrial Research Organization
ECMWF	European Centre for Medium-Range Weather Forecasts
Enh.	Enhancement(s)
ERA5	ECMWF Reanalysis Version 5
ESA	European Space Agency
EU	European Union
FOV	Field of view
GHG	Greenhouse gas
GOES	Geostationary Operational Environmental Satellites
GWP	Global Warming Potential
HITRAN2016	HIgh-resolution TRANsmission molecular absorption database
HYSPLIT	Hybrid Single-Particle Lagrangian Integrated Trajectory
IME	Integrated mass enhancement in tonnes
IME_{ret}	Retrieved integrated mass enhancement in tonnes
IME_{sim}	Simulated integrated mass enhancement in tonnes
ISS	International Space Station
L1B	Level 1B
L4	Level 4
LEO	Low Earth orbit
LES	Large eddy simulation
LSQ	Least-squares
MBMP	Multi-band-multi-pass
MBSP	Multi-band-single-pass
MLE	Maximum likelihood estimation
m_{CH_4}	Molar mass of methane
m_{MBSP}	Fractional absorption model for MBSP methane column retrieval
NIR	Near-infrared
NOAA	National Oceanic and Atmospheric Administration
NO_2	Nitrogen dioxide
NWO	Dutch Research Council
OE	Optimal Estimation
O&G	Oil and gas
OSSE	Observing System Simulation Experiment
POD	Probability of detection
ppb	Parts per billion

Abbreviation	Definition
RT	Radiative transfer
S5P	Sentinel-5 Precursor
Sim.	Simulated/simulation
SWIR	Short-wave infrared
TIR	Thermal infrared
TOA	Top-of-atmosphere
TROPOMI	TROPOspheric Monitoring Instrument
TSIS-1	Total and Spectral Solar Irradiance Sensor-1
US	United States
UV	Ultraviolet
UVIS	Ultraviolet-visible

Symbols

Symbol	Definition	Unit
$\mathrm{A_M}$	Plume mask area	$\mathrm{m^2}$
$\bar{\mathrm{A}}$	Mean pixel area	$\mathrm{m^2}$
C	Cost function	-
c	Least-squares scaling factor on target day	-
c_{ref}	Least-squares scaling factor on reference day	-
$\mathrm{D_{i,m,n}}$	Binary detectability of plume i for location m and albedo background n	-
F	Continuous inverse link function	-
f	Radiative transfer model	-
g	Predictor function	-
L	Plume length	m
ℓ	Loglikelihood function of the Bernoulli distribution	-
M_{CH_4}	Methane molar mass	$\mathrm{g\ mol^{-1}}$
Q	Source rate	$\mathrm{t\ h^{-1}}$
$\mathrm{Q_{der}}$ or $\hat{\mathrm{Q}}$	Derived source rate	$\mathrm{t\ h^{-1}}$
$\mathrm{Q_p}$	Minimum source rate for a p% probability of detection	$\mathrm{t\ h^{-1}}$
$\mathrm{Q_{sim}}$	Simulated source rate	$\mathrm{t\ h^{-1}}$
R	Radiance	$\mathrm{W\ m^{-2}\ sr^{-1}}\ \mu\mathrm{m^{-1}}$
$\mathrm{R_0}$	Top-of-atmosphere solar radiance	$\mathrm{W\ m^{-2}\ sr^{-1}}\ \mu\mathrm{m^{-1}}$
$\mathrm{R_5}$	Band 5 radiance on target day	$\mathrm{W\ m^{-2}\ sr^{-1}}\ \mu\mathrm{m^{-1}}$
$\mathrm{R'_5}$	Band 5 radiance on reference day	$\mathrm{W\ m^{-2}\ sr^{-1}}\ \mu\mathrm{m^{-1}}$
$\mathrm{R_6}$	Band 6 radiance on target day	$\mathrm{W\ m^{-2}\ sr^{-1}}\ \mu\mathrm{m^{-1}}$
$\mathrm{R'_6}$	Band 6 radiance on reference day	$\mathrm{W\ m^{-2}\ sr^{-1}}\ \mu\mathrm{m^{-1}}$
$\mathrm{T_N}$	Modelled top-of-atmosphere radiance in band N	$\mathrm{W\ m^{-2}\ sr^{-1}}\ \mu^{-1}$
$\mathrm{U_{10}}$	Wind speed at ten meters altitude	$\mathrm{m\ s^{-1}}$
$\mathrm{U_{eff}}$	Effective wind speed	$\mathrm{m\ s^{-1}}$
$\boldsymbol{x}_{m,n}$	POD variable vector for location m and albedo background n	-
z	Location	-
α	Albedo	-
γ_{SZA}	Solar zenith angle	rad or °

Symbol	**Definition**	**Unit**
γ_{VZA}	Viewing zenith angle	rad or °
ΔR	Target day reflectance difference	W m^{-2} sr^{-1} μm^{-1}
$\Delta R'$	Reference day reflectance difference	W m^{-2} sr^{-1} μm^{-1}
$\Delta\Omega$	Enhanced methane column concentration	mol m^{-2}
$\Delta\Omega'$	Enhanced methane column concentration on reference day	mol m^{-2}
$\boldsymbol{\theta}_{m,n}$	Continuous inverse link function coefficients for location m and albedo background n	-
λ	Wavelength	nm or μm
σ_i	Absorption coefficient of atmospheric gas i	m^2 mol^{-1}
$\boldsymbol{\phi}_{m,n}$	Predictor function coefficients for location m and albedo background n	-
Ω	Nominal methane column concentration	mol m^{-2} or ppb

Part I

Background

1

Introduction

Methane is a potent greenhouse gas that is responsible for roughly one-quarter of total global warming since preindustrial times. It is emitted by various natural and anthropogenic sources, including oil & gas (O&G) facilities, coal mines, biomass burning, ruminants and rice paddies. The strong greenhouse gas (GHG) is the primary constituent of natural gas and frequently leaks from O&G infrastructure through deteriorating pipelines, oil wells, storage facilities and processing plants. It is predominantly removed from the atmosphere by oxidation by OH radicals in the troposphere. Its global warming potential (GWP) reduces drastically over time, from 83 ± 26 over 20 years to 30 ± 11 over 100 years, due to its short atmospheric lifetime. This presents an opportunity for effective climate change mitigation by preventing the emission of methane from anthropogenic sources.

When methane leaks from a point source and atmospheric concentrations reach significantly above the background concentration downwind of this source, the resulting cloud is called a plume. Different complementary approaches exist to detect plumes but satellites are frequently used due to their large spatial coverage. Satellites can observe back-scattered solar radiance at the top of the atmosphere in the shortwave infrared, and an inverse radiative transfer model can be used to retrieve back the methane enhancements. The current satellite fleet used to observe methane is entirely based in low-Earth orbit (LEO) and can only revisit a location at most once per day with a constant overpass time. This makes it impossible to detect most intermittent and brief emissions or any diurnal variation in methane emissions.

In 2023, [1] published the first study that demonstrated the ability of the geostationary GOES-16 weather satellite to detect and quantify large methane leaks from intermittent sources by taking advantage of its five-minute revisit time over the contiguous United States. This thesis will continue in the field of geostationary methane detection and quantification, and aims to assess GOES-16's quantitative methane leak monitoring capabilities. The novelty of this thesis is in the application of existing methodologies to characterize, quantify and assess GOES' methane-sensing capabilities to enhance understanding of its efficacy in detecting methane emissions.

This thesis is structured as follows. Chapter 2 provides background theory on the important concepts behind this research, such as methane's role as a climate change driver, satellite remote sensing of GHGs and the current satellite fleet for space-based methane monitoring. Chapter 3 defines the research questions and contextualizes the significance of the research. Chapter 4, Chapter 5 and Chapter 6 introduce the methodology that is used to detect methane leaks and quantify their emissions. Chapter 7 presents the verification and sensitivity analysis of GOES' retrieval and quantification model. Chapter 8 then presents the results of this thesis and their validation. Chapter 9 concludes the findings of this thesis, and, lastly, Chapter 10 provides recommendations for future work.

2

Theoretical background

This chapter serves as an introduction to the theoretical background behind important concepts of this thesis. Section 2.1 discusses methane in the context of anthropogenic climate change, methane's role in the atmosphere and the global methane budget. Next, Section 2.2 discusses the principles behind measuring atmospheric methane using satellite remote sensing and different approaches to methane flux retrievals. Lastly, an overview of the current satellite fleet with methane-observing capabilities is given in Section 2.3.

2.1. Methane's potency as a greenhouse gas

To understand why methane monitoring and detection is important, the contribution of atmospheric methane to global warming must be understood. Identifying methane sinks and sources is important to understand which areas are relevant to mitigate its climate effects. This section introduces these topics and highlights the political initiatives aiming to reduce anthropogenic methane emissions.

2.1.1. Anthropogenic climate change

Since the start of the Industrial Revolution, large amounts of burned fossil fuels have resulted in anthropogenic GHG emissions. The accumulation of GHGs in the atmosphere, such as carbon dioxide (CO_2), methane (CH_4) and nitrous oxide (N_2O), has lead to a rapid increase in global temperature, unprecedented over at least the past ten thousand years. Figure 2.1 shows the observed increase in global surface temperature since the start of the Industrial Revolution, along with four climate model simulations that account for different temperature forcers. The observed warming trend is only reproduced in simulations that include human and natural causes, whereas any other simulation does not match the observed trend. This is one of the reasons behind a global scientific consensus that global warming is unequivocally caused by human influence. [2–4]

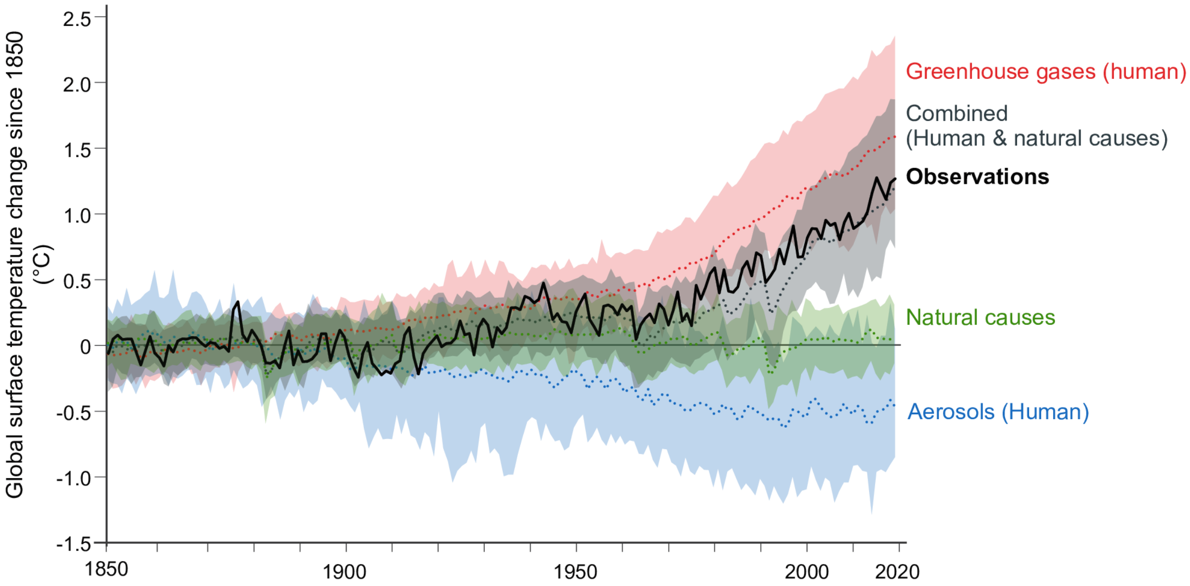

Figure 2.1: Global surface temperature rise between 1850 and 2019 for different simulations. The observed temperature rise (annual average) matches simulations that include anthropogenic and natural influences, whereas simulations with only natural forcing do not. The shaded regions indicate the 5-95% confidence interval. [2]

If current levels of GHG emissions continue, Earth's atmosphere will very likely heat up by multiple degrees Celsius by the turn of the century. This will destabilize weather patterns, crop production, biodiversity, ecosystems, global health, glacier extent and more. Approximately 3.3 to 3.6 billion people and a large portion of all animal and plant species live in areas that are highly vulnerable to climate change. If global warming can be limited to 1.5°C, losses to ecosystems and human systems can be reduced significantly compared to higher temperature increases. [2]

2.1.2. Atmospheric methane as a climate change driver

Methane is one of the major GHGs that is driving climate change so its emission must be detected, quantified and, eventually, reduced. After carbon dioxide, it is the second most important GHG and is responsible for roughly 25% of the total warming since preindustrial times. The National Oceanic and Atmospheric Administration (NOAA) has measured atmospheric methane concentrations since 1983 with a global network of measurement sites [5]. Figure 2.2 shows the globally-averaged values that are calculated once per month. The latest trend shows a strong rise in atmospheric methane concentrations of about 166% in approximately the last 250 years, from 722 ± 25 parts per billion (ppb) in 1750 (start of the Industrial Revolution) to 1922 ± 0.6 ppb in 2023. Atmospheric concentrations are now the highest in at least the past 800,000 years. Methane is also a large contributor to the formation of ozone, a harmful air pollutant that caused approximately 423,000 deaths in 2019. [4, 6–8]

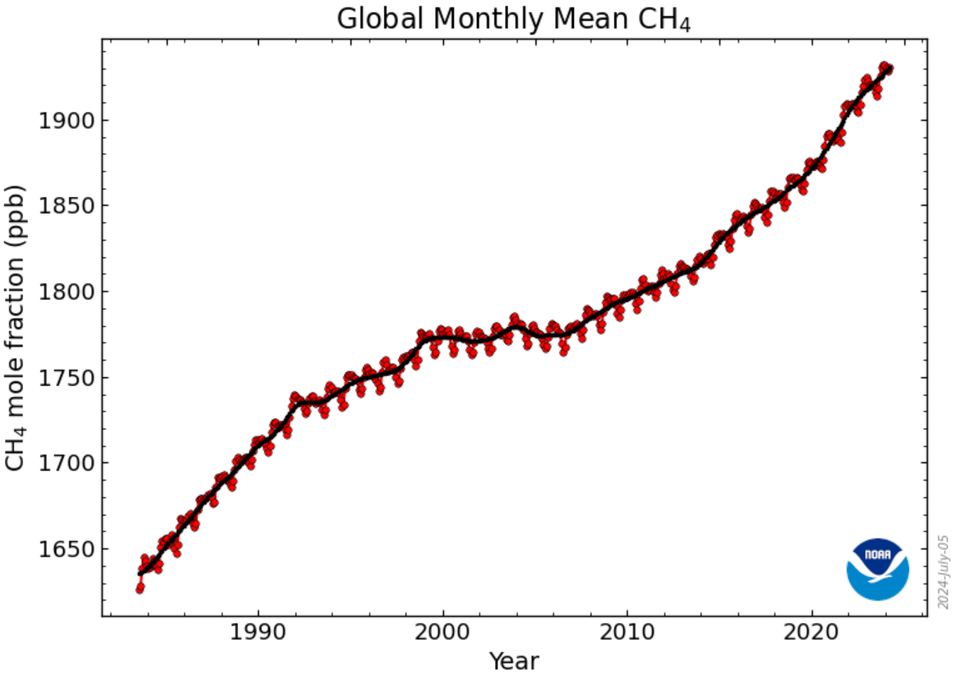

Figure 2.2: Rise in globally-averaged atmospheric methane concentrations in recent decades. Values are monthly averages taken from ocean-based measurement stations since 1983. [5]

Methane is a short-lived GHG and lasts about a decade on average, before oxidizing with hydroxyl radicals (OH·) or in dry soils. Its Global Warming Potential (GWP) is 83 ± 26 over 20 years, where GWP is a measure of a molecule's warming potential relative to CO_2 over different periods. Due to methane's short atmospheric lifetime, its GWP reduces to 30 ± 11 over 100 years. Methane's short lifetime presents an opportunity for effective climate change mitigation by preventing its emission from anthropogenic sources. [9–11]

2.1.3. Global methane budget

Methane is emitted by natural and anthropogenic sources, and is absorbed by natural sinks. Fluxes measure the amount of emitted or absorbed methane mass over time. Sources contribute an influx (positive flux), whereas sinks contribute an outflux (negative flux). A variable imbalance between the influx and outflux has existed since at least 1980, causing atmospheric concentrations to increase. The magnitude of the imbalance directly determines the growth rate of atmospheric methane concentration, as shown in Figure 2.3 by the slope of the black line and imbalance per decade.

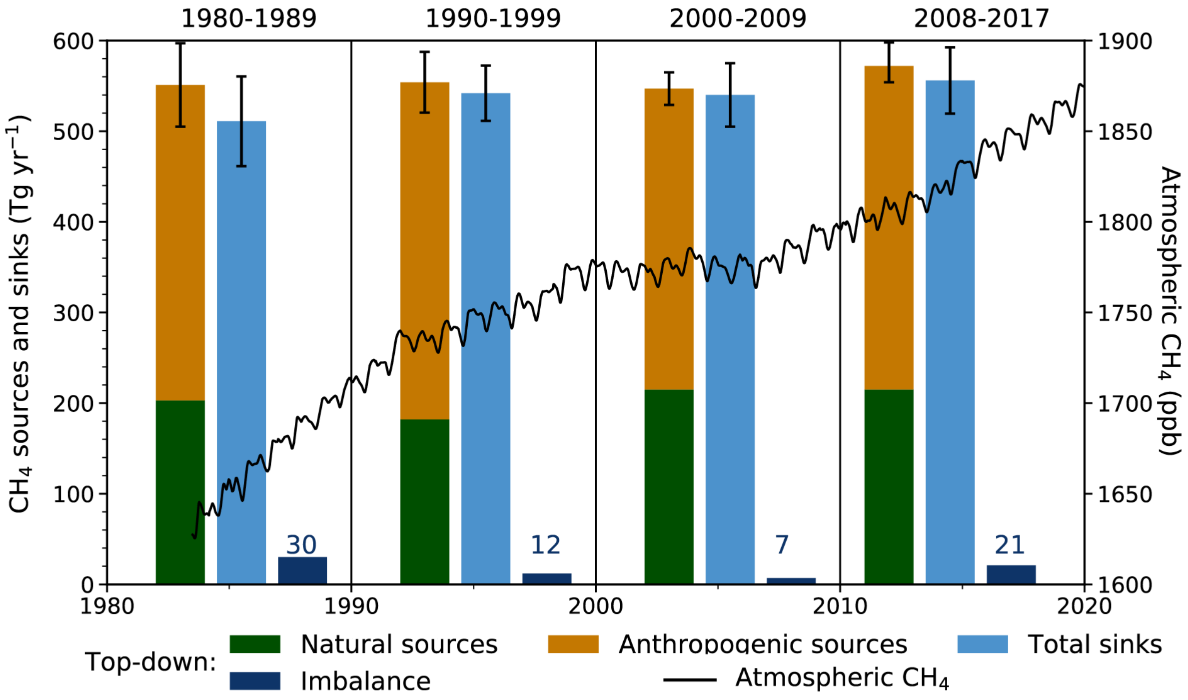

Figure 2.3: Methane sinks and sources with the budget imbalance over the past forty years. The histograms show the flux of sources (natural and anthropogenic), sinks and the imbalance per decade on the left vertical axis, as determined by satellite measurements. The error bars indicate the one-sigma uncertainties. The black line shows monthly averages of concentration values since 1983 on the right vertical axis. [4]

2.1.3.1. Natural sources

Natural sources include wetlands, permafrost soils, lakes, termites, geological sources and biomass burning. Wetlands, permafrost soils and lakes store animal and plant material, where microorganisms called methanogens produce methane as a byproduct of their metabolism by decomposing the organic matter in an anaerobic environment. This process is called methanogenesis and forms the predominant biogenic methane source [12]. Termites also expel methane as a byproduct of digesting plant material. Geological sources, such as geothermal vents and volcanoes, release fossil methane gas that is formed in the same Earth layers as coal and oil. In the case of biomass burning, incomplete combustion of hydrocarbons results in methane and other non-CO_2 species. [6]

2.1.3.2. Anthropogenic sources

Anthropogenic sources include agriculture, oil and gas (O&G) facilities, coal mines, landfills and biomass burning. Agriculture is the largest anthropogenic source and includes emissions from livestock (mostly ruminants) and rice cultivation. Ruminants release methane from the enteric fermentation of organic matter in their stomach and the controlled flooding of rice paddies leads to methanogenesis in the soil [13, 14]. In landfills, decaying organic matter in anaerobic conditions also creates methane, which may not be captured to be utilized as an energy source. The energy sector is methane's second largest anthropogenic source and is responsible for around 40% of total yearly anthropogenic emissions due to leaking O&G infrastructure and venting coal mines. Natural gas (90% methane by volume) is often extracted alongside oil and coal due to the presence of decaying organic matter [15]. Natural gas can be vented or flared for economic, safety and regulatory reasons, releasing methane into the atmosphere [16]. O&G infrastructure is particularly susceptible to unintended methane leaks due to poorly maintained pipelines, oil wells, storage facilities and processing plants. In total, the O&G industry emitted 82 million tonnes of methane in 2019, equivalent to the total annual CO_2-equivalent emissions of almost 600 coal-fired power plants. These leaks may result in methane plumes: areas with atmospheric concentrations significantly above the background as caused by an upwind point source. [17, 18]

2.1.3.3. Natural sinks

Methane's most important natural sink is oxidation by OH radicals in the troposphere, which reaction is shown in Equation 2.1:

$$CH_4 + OH\cdot \rightarrow CH_3 \cdot + H_2O \tag{2.1}$$

After multiple subsequent reactions, CO_2 and H_2O are the final reaction products. OH radicals have been dubbed as an "atmospheric detergent" for their role in breaking down methane [19]. Biological oxidation in dry soils and methane loss to the stratosphere are the second and third largest methane sinks, respectively. [20, 21]

A breakdown of the global methane cycle with the source and sink fluxes is visualized in Figure 2.4.

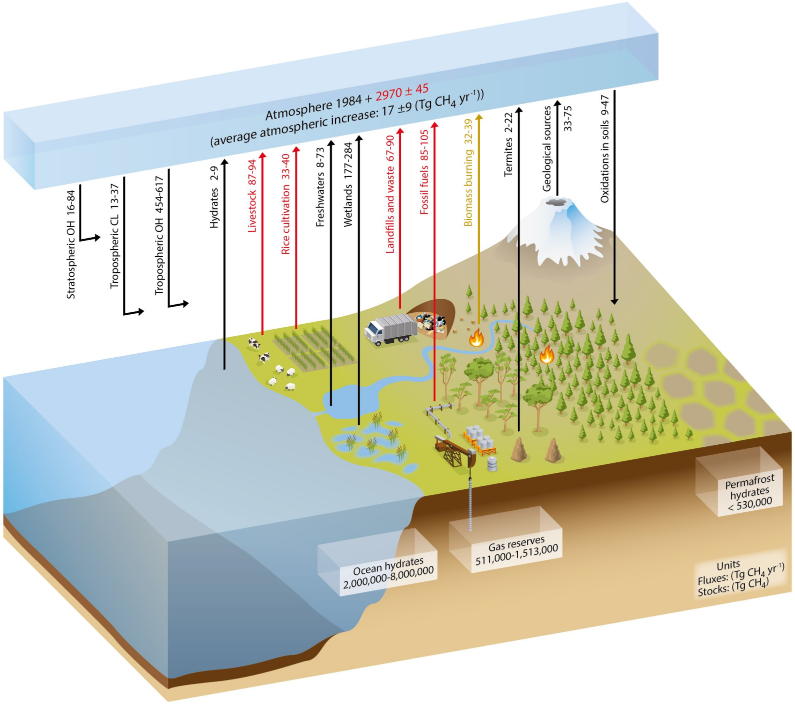

Figure 2.4: Global methane cycle with major sources, sinks and reservoirs. Black arrows represent natural fluxes, red arrows denote anthropogenic fluxes and the light brown arrow denotes a combined natural and anthropogenic flux. [6]

2.1.4. Approaches to methane flux estimation

Studying methane fluxes is critical to understanding where and how much methane is emitted. Two complementary approaches exist to determine these emissions: (1) bottom-up and (2) top-down. The definitions presented here hold for the scientific remote sensing industry but note that the definition of these approaches varies per industry and application.

1. **Bottom-up:** This approach works by collecting representative emission or absorption measurements from a small, representative sample of sinks or sources and extrapolating these samples to larger populations. More representative and more inclusive samples lead to more accurate estimates. Relevant input data includes fossil fuel production, organic waste production, cattle headcounts, soil types, vegetation types, wildfire frequencies, waterbody maps, meteorological data and hydroxyl radical concentrations. An example is to collect yearly fossil fuel production data from a local oil refinery and multiply this data by an emission factor that describes the amount of

methane mass emitted per unit of produced fossil fuel. This yields the total amount of methane emitted by that refinery per year. Extrapolating this number to all oil refineries in the world yields global yearly emissions. Bottom-up measurements are accurate in identifying sources or sinks due to their in-situ measurements, but a downside is the challenge of collecting a measurement sample that is representative of a large, diverse population. [22, 23]

2. **Top-down:** This approach relies on measurements of atmospheric methane concentrations at different locations from various sources. This concentration data is then used to estimate the corresponding emissions using an atmospheric transport inversion model. This model uses an initial methane flux estimate and atmospheric transport to simulate fluxes such that the differences between the measured concentrations and the modelled concentrations are minimized. The atmospheric methane measurements aggregate flux contributions from all sources so they can be used to compare to bottom-up measurements to reveal missing sources, but the aggregation makes top-down measurements unfit to isolate individual sources. [22, 24]

The bottom-up and top-down methods are visualized in Figure 2.5.

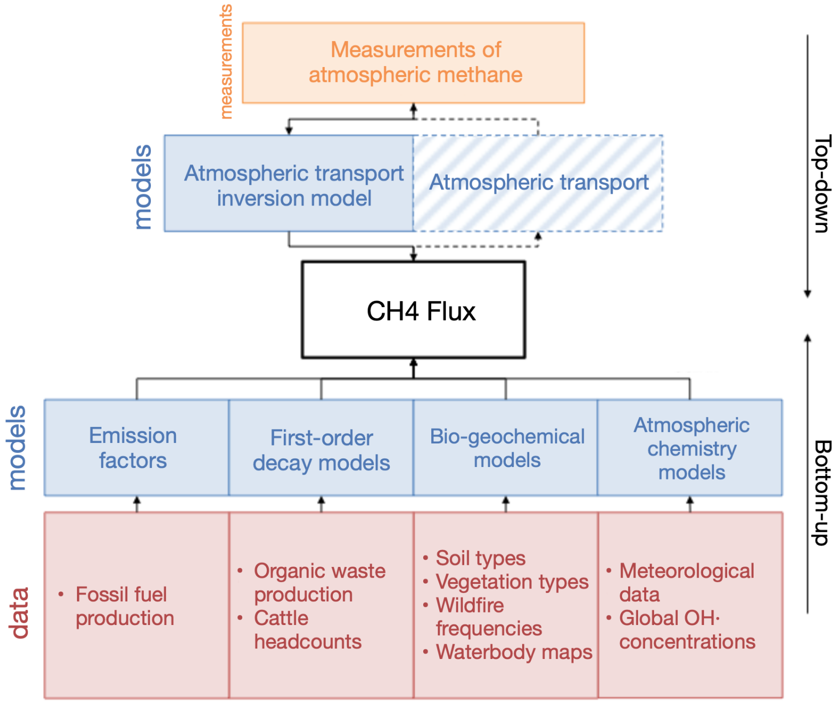

Figure 2.5: Overview of bottom-up and top-down approaches to determine methane flux. Adapted from [23].

Space-based methane measurements fit within the top-down approach. The main advantage of the top-down approach is that it provides a constraint on total methane emissions, whereas the bottom-up approach can face issues with the accuracy, availability and completeness of the input data. To mitigate methane emissions, it is important that recent leaks are discovered quickly and the top-down method is best suited for that.

2.1.5. Mitigating methane emissions

Mitigation of methane emissions represents a major opportunity to slow near-term global warming due to methane's short atmospheric lifetime and potency as a GHG [1, 2, 25]. Methane leaks from O&G infrastructure and other anthropogenic sources can be reduced with available and affordable mitigation measures, and various political initiatives have pledged to reduce emissions in the past five years, such as the Global Methane Pledge (2021), the US Inflation Reduction Act (2022) and the European Union

Methane Strategy (2024) [26, 27].

Table 2.1 presents an overview of possible mitigation measures per emission sector. These measures are technically feasible with no to minimal up-front investments. [26]

Table 2.1: Examples of possible methane emission mitigation measures per sector.

Sector	Possible mitigation measures	Source
Oil & gas	Local leak detection, methane capture during intentional venting, replacing leaking pumps and pipelines	[28]
Coal	Pre-mining coal degasification, flooding unused mines, oxidising methane in ventilation air of underground mines	[29], [30]
Livestock	Antimethanogen vaccines, manure treatment in biogas digesters, improved feed conversion efficiency	[31], [29], [32]
Rice	Dry cultivation instead of wet, soil amendments, no tilling	[26], [33], [34]
Landfills	Methane flaring, gas recovery and utilization, improved organic waste separation	[33]
Wastewater	Gas recovery and utilization, constructing aerobic wastewater treatment plants, improving sanitation infrastructure to prevent open-air sewers	[33]

2.2. Measuring atmospheric methane concentrations

Atmospheric methane concentrations can be measured in-situ or remotely. Multiple complementary methods to collect these measurements exist, including ground-based measurement stations, aircraft, drones, ships and satellites. Ground-based monitoring stations measure almost real-time and are highly accurate but lack spatial coverage since they are confined to a single location. Aircraft and ships have better spatial coverage than ground-based stations but lack temporal coverage. Drones have the advantage of quick deployment time and low operating costs but are more limited in deployment duration and maximum mass of the measurement device than other methods. Satellites have the advantage of large spatial coverage and long mission durations but may have slow revisit times, depending on their orbit. [35–37]

Two different approaches to determining methane fluxes are introduced in Section 2.1.4. Section 2.2.1 introduces the concepts behind satellite remote sensing.

2.2.1. Satellite remote sensing

Methane is a colorless gas which is invisible in the visible part of the electromagnetic spectrum. Its detection relies on its absorption of specific wavelengths of infrared light. The field of study that analyses the absorption and emission of light by matter is called spectroscopy. Spectroscopy is a useful technique in remote sensing since it allows remote objects to be studied based on how they interact with light.

The general principle behind methane detection is infrared (700 nm - 1 mm) spectroscopy. Infrared spectroscopy exploits the fact that molecules absorb certain frequencies in the infrared part of the spectrum, as determined by the molecule's shape. Methane has an asymmetric, tetrahedral shape with four covalent C-H bonds. These bonds can stretch and bend (much like springs), allowing the molecule to vibrate and rotate at many different frequencies. The frequencies at which a molecule can vibrate or rotate are called their vibrational or rotational modes. If the frequency of incident infrared radiation from a beam source matches a resonance frequency of a molecule's vibrational or rotational mode, the photon is absorbed by the molecule and the photon's energy is converted into vibrational or rotational energy. If the photon's frequency does not match a resonance frequency, it is transmitted through the medium unabated. Comparing the wavelengths of the transmitted radiation to the incident radiation yields the absorption spectrum, which shows an absorption peak at the corresponding wavelengths. The larger a molecule and the more asymmetric its shape, the more vibrational and rotational modes it will have. This explains why methane can absorb so many different wavelengths of light and why it is such a powerful GHG. Figure 2.6 presents an overview of infrared spectroscopy. [38]

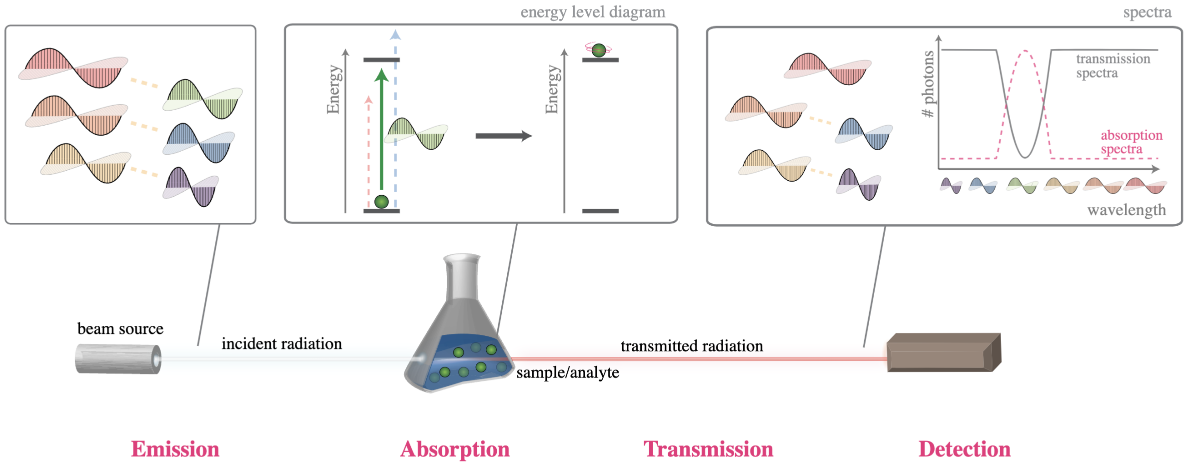

Figure 2.6: Overview of absorption of electromagnetic radiation. When multiple wavelengths of incident radiation (shown here as white light) are emitted by a beam source (left) and passed through a sample (center), a wavelength is absorbed if it matches a resonance frequency of that molecule. This increases the energy of the molecule. The absorption spectrum of the remaining radiation, now of different color (shown here as green light), shows a peak at the absorbed wavelength. After absorption, five of the original six wavelengths remain and a peak at the missing wavelength is present in the absorption spectrum. [39]

To estimate total columns of methane, the incident radiation is all wavelengths in sunlight and the transmitted radiation is reflected sunlight at the top of the atmosphere (TOA), where it can be detected by a satellite. Methane strongly absorbs wavelengths in the shortwave infrared (SWIR; 1400-3000 nm) range of the spectrum, with peaks around 1650 and 2200 nm. Since the absorbing wavelengths are known, an absorption spectrum is similar to a gas' fingerprint. Detection of the unabated wavelengths can thus be used to detect that gas and deduce its original concentrations in the atmosphere. This is called a retrieval. To this end, methane-observing satellites with SWIR-sensitive instruments will have their range of observed wavelengths, called spectral bands, centered around absorbing wavelengths for optimal methane detection [1]. Figure 2.7 shows the absorption spectra of methane, carbon dioxide, water vapor, nitrous oxide and carbon monoxide between 1500 and 2500 nm. The optical depth (vertical axis) is a measure of absorption and is defined as the natural logarithm of the ratio of incident to transmitted radiation flux. The apparent chaotic nature of the absorption spectrum of each gas shows that resonance frequencies of each molecule's vibrational or rotational mode absorb strongly whilst other frequencies are transmitted unabated.

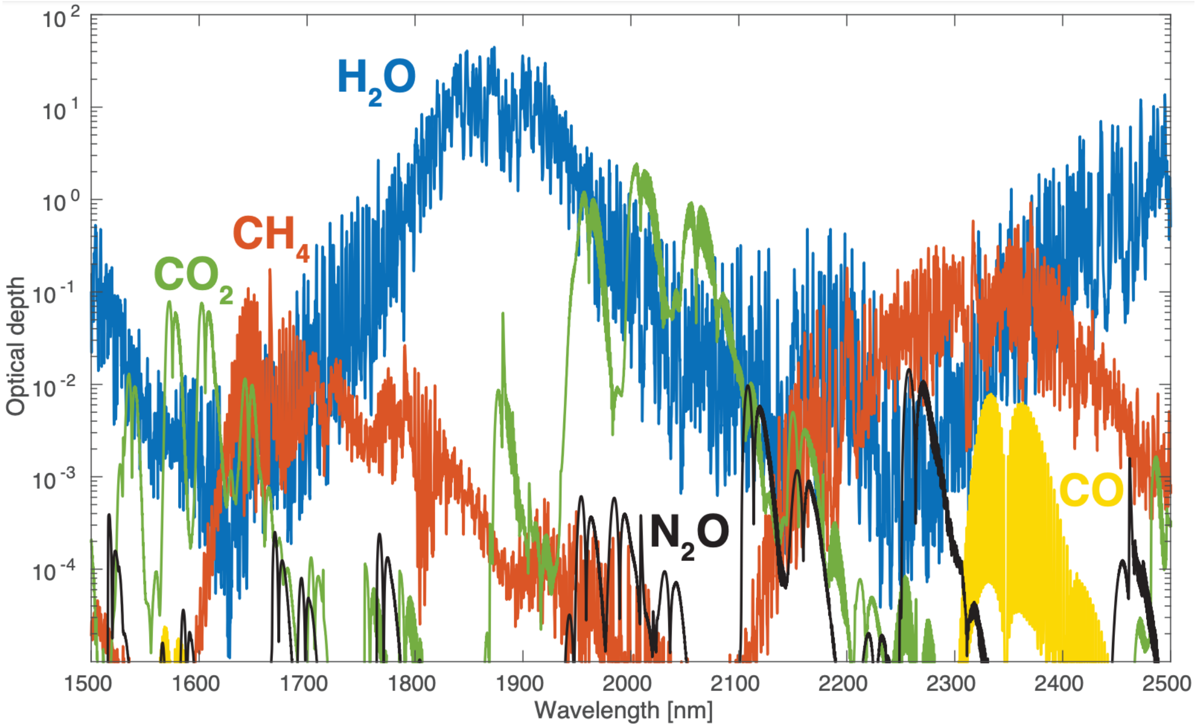

Figure 2.7: Absorption spectra of different atmospheric trace gasses in the SWIR range. High optical depth means high absorption. Methane absorption peaks at around 1650 and 2200 nm. Values are for the US Standard Atmosphere and are smoothed with a resolution of 0.1 nm. [40]

The amount of spectral absorption depends on the optical path of the photons through the atmosphere. Using the geometry from Figure 2.8, large solar zenith angles (γ_{SZA}) and viewing zenith angles (γ_{VZA}) result in a longer optical path through the atmosphere. The solar zenith angle is the angle between the local zenith and the line of sight to the Sun. The viewing zenith angle is the angle between the local zenith and the line of sight to the satellite. The airmass is defined as the sum of the vertical components of the optical path, as given by Equation 2.2.

$$\text{airmass} = \frac{1}{cos(\gamma_{SZA})} + \frac{1}{cos(\gamma_{VZA})} \tag{2.2}$$

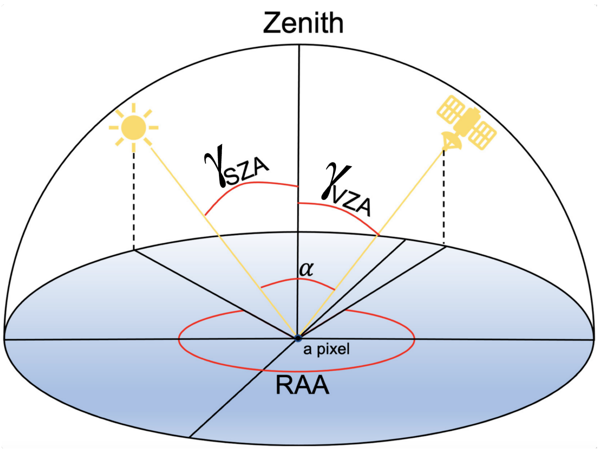

Figure 2.8: Schematic of Sun-satellite geometry. The Sun's photons travel downwards to Earth's surface (1), are reflected at an observation location (2) and travel back to space (3). The solar zenith angle and viewing zenith angle are defined as γ_{SZA}, γ_{VZA}, respectively. The other angle definitions are not relevant for this thesis. Adapted from [41].

2.2.2. Satellite instrument design and characteristics

Spectrometers are optical instruments that measure the intensity of incoming light at different wavelengths. Spectrometers use a dispersive element, such as a prism or a diffraction grating, to separate the incoming light in its different constituent wavelengths. Lenses and mirrors are then used to direct the separated wavelengths onto a sensor, where the light is converted to electrical signals. Spectrometers are the most commonly used instruments for remote sensing with satellites.

A satellite's methane sensitivity refers to the emission rate of a methane leak (also called the source rate) that can be detected by the satellite. Highly sensitive satellites can detect emissions with low source rates, whereas low sensitivity only allows the detection of emissions with high source rates. The sensitivity is a result of the satellite's spectral resolution, which defines the capability of the instrument to separate different wavelengths. A higher spectral resolution (narrower bands) would reduce the overlap between different absorption features and make methane's absorption more pronounced. This is why satellites that are most sensitive to methane have high spectral resolution [42]. A satellite's detection capability is the result of its spatial resolution (higher spatial resolutions facilitate the detection of the potential source) and its methane sensitivity.

2.3. Satellite fleet for space-based methane observations

Various space agencies, scientific institutes and commercial companies have launched satellites in recent years to detect and monitor methane emissions from space. This section presents an overview of different satellite instruments that form a large part of the methane-observing satellite fleet and highlights two instruments, TROPOMI and GOES-16, in further detail.

2.3.1. Overview of active instruments

Table 2.2 presents an overview of twelve SWIR satellite instruments that measure atmospheric methane concentrations from space. The instruments are ranked based on their methane sensitivity as a result of their spectral resolution (high: <1 nm, medium: 1-20 nm, low: >20 nm) and classified as area flux mappers or point source imagers. Area flux mappers are designed to monitor total emissions on a regional and global scale with a coarse spatial resolution (pixel sizes between 0.1-10 km) and large swath width. Point source imagers are designed to detect methane plumes directly on a facility-level scale with a high spatial resolution (pixel sizes typically below 60 m) and narrow swath width. Organization abbreviations include Environmental Defense Fund (EDF), Japanese Aerospace Exploration Agency (JAXA), Japanese Ministry of Environment (MOE), Japanese National Institute for Environmental Studies (NIES), Agenzia Spaziale Italiana (ASI), National Aeronautics and Space Administration (NASA), Deutsches Zentrum für Luft- und Raumfahrt (DLR) and United States Geological Survey (USGS). [43]

All instruments in Table 2.2 observe methane from SWIR reflected sunlight at the top of the atmosphere in the 1.65 μm band (1.63-1.70 μm) or the 2.3 μm band (2.2-2.4 μm). These bands coincide with strong absorption features of methane (see Figure 2.7). Under cloud-free conditions, the satellites in Table 2.2 can retrieve the methane concentration in the entire atmospheric column but the TOA radiances do not provide information on the vertical methane distribution in the atmosphere. [40, 44]

Except for EMIT and GOES-16, all instruments in Table 2.2 are in near-polar, sun-synchronous orbits with constant overpass times in the morning or early afternoon (local time at the ascending node). The EMIT instrument is onboard the International Space Station (ISS) in a 51.6° inclined orbit, which has variable local overpass times, and GOES-16 is a geostationary satellite located above the equator at 75.2°W, with overpass times throughout the day at 30-minute intervals in North and South America and 5-minute intervals in the contiguous United States (CONUS). The early overpass times of the sun-synchronous satellites take advantage of lower chances of cloud cover in mornings and steadier near-surface wind conditions in early afternoons, which is beneficial for retrieving methane plumes. The LEO satellites also have revisit times of 1 day (except for the VIIRS constellation, which consists of three

Table 2.2: Overview of subset of shortwave infrared satellite instruments for atmospheric methane measurements. Unless indicated otherwise, [43].

Instrument	Organization	Launch date	Category	Coverage	Overpass time (local)	Revisit frequency[a]	Nadir spatial resolution	Spectral resolution (nm)	Methane sensitivity	Detection limit [t/h]
TROPOMI	ESA	Oct. 13, 2017	Area flux mapper	Global	13:30 [45]	1 day	5.5x7 km^2	0.23	High	8 [46]
GHGSat	GHGSat	2016-2023[b] [47]	Point source imagers	12x12 km^2 targets	09:30 - 13:08 [48]	2-3 days[c] [49]	25x25 m^2	0.3	High	0.1-3 [50]
MethaneSAT	EDF	Mar. 4, 2024	Area flux mapper	200x200 km^2 targets	13:00 [51]	3-4 days	130x400 m^2	0.3	High	0.5 [40]
GOSAT	JAXA, MOE, NIES	Jan. 23, 2009	Area flux mapper	Global & targets	12:49 [52]	3 days	10 km diameter	0.06	High	Not applicable
PRISMA	ASI	Mar. 22, 2019	Point source imager	30x30 km^2 targets	10:30 [53]	4 days	30x30 m^2	10	Medium	0.5-2 [54]
EMIT	NASA	Jul. 14, 2022	Point source imager	Arid regions	Variable [55]	3 days	60x60 m^2	9	Medium	0.5 [56]
Tanager-1	Carbon Mapper and Planet	Aug. 16, 2024	Point source imager	Targets	11:30 [57]	1-7 days[c]	30x60 m^2	6	Medium	0.1 [56]
EnMAP	DLR	Apr. 1, 2022	Point source imager	30x30 km^2 targets	11:00 [58]	4 days	30x30 m^2	10	Medium	1 [46]
Landsat-8	USGS	Feb. 11, 2013	Point-source imager	Global	10:00 [59]	16 days	30x30 m^2	200	Low	1.8-25 [42, 60]
Sentinel-2	ESA	Jun. 23, 2015	Point source imager	Global	10:30 [61]	2-5 days	20x20 m^2	200	Low	1.8-25 [42, 60]
VIIRS[d]	NASA	2011-2022[e]	Point source imager	Global	12:30 - 14:30 [62]	3 times daily[f]	750x750 m^2	50 [63]	Low	10-15 [64]
GOES-16 [1]	NASA	Nov. 19, 2016	Point source imager	N. & S. America	Geostationary	5 minutes[g]	2x2 km^2	50	Low	**Unknown**

[a] The time between consecutive observations of the same location.

[b] Includes GHGSat-D and GHGSatC1-11 satellites. More launches planned in 2025.

[c] For the whole constellation. Individual satellites revisit every 14 days.

[d] VIIRS instruments are onboard Suomi-NPP, NOAA-20 and NOAA-21. VIIRS plume detections have been shown under favourable conditions. [62]

[e] Suomi-NPP: Oct. 28, 2011; NOAA-20: May 30, 2018; NOAA-21: Nov. 10, 2022.

[f] For the whole constellation. Each instrument has daily coverage.

[g] Revisit frequency depends on scanning mode. Contiguous US has 5-minute coverage.

satellites with daily coverage). Combined, this means the current satellite fleet is generally incapable of detecting intermittent methane emissions and emission variability during the day. [1, 43]

The disparate spatial and spectral resolutions, revisit frequencies, overpass times and coverage areas of individual satellites present an opportunity for synergies between satellites to improve detection capabilities and attribution of plumes to their source. For example, TROPOMI is designed to accurately detect methane over large areas (high spectral resolution and coarse spatial resolution), making attribution only possible for isolated sources. By combining highly accurate reference detections by TROPOMI with high-spatial-resolution detections by GHGSat, PRISMA and Sentinel-2, facility-level emissions sources have been discovered across O&G extraction regions. Another example includes the three active VIIRS instruments, which have consecutive overpasses within one hour of each other. This allows overpasses of the same area to be combined to detect transient emissions and analyze variability in the source rate. These examples illustrate how synergies between satellites can be leveraged to effectively improve the detection capabilities of the current satellite fleet. [62, 65]

Band-imagers, such as GOES-16, VIIRS, Landsat-8 and Sentinel-2, measure the average magnitude of reflectances across a spectral band. Wide spectral bands make it more difficult to resolve methane's absorption. These band-imagers have two to three orders of magnitude coarser spectral resolutions than their hyperspectral counterparts, such as TROPOMI. Despite not being designed for it, these band-imagers have demonstrated the ability to detect large methane plumes under favorable conditions (homogeneous areas with high albedo). [1, 54, 62, 66–68]

Knowing the limitations of the current satellite fleet, the potential for cross-satellite synergies and the ability of band-imagers to detect methane plumes, GOES-16's quick revisit frequency presents an opportunity to detect intermittency and variability in emission rates from pinpointed methane sources. This is impossible with the current LEO satellite fleet. Combining TROPOMI's high methane sensitivity with GOES-16 high temporal resolution creates an opportunity for a synergy between both satellites. Section 2.3.2 and Section 2.3.3 will further elaborate on the role of these instruments within the current satellite fleet.

2.3.2. TROPOMI

The TROPOspheric Monitoring Instrument (TROPOMI, see Figure 2.9) is a hyperspectral imaging spectrometer and the sole instrument onboard the Sentinel-5 Precursor (S5P) satellite. It was launched onboard a Rockot rocket from the Plesetsk Cosmodrome in Russia on October 13, 2017. Its primary purpose is to measure concentrations of various atmospheric trace gases, such as methane, ozone, sulfur dioxide, carbon monoxide, formaldehyde and nitrogen dioxide. TROPOMI was commissioned as part of the European Union's (EU) Copernicus program and developed by a consortium of 30 partners, including ESA and SRON Netherlands Space Research Institute. From design to launch, the mission cost EUR220m (2017). [69]

Figure 2.9: Artist impression of the TROPOMI instrument onboard the Sentinel-5 Precursor satellite. [70]

TROPOMI measures 8 different spectral bands with four different spectrometers, each targeting a separate spectral range: ultraviolet (UV, 100-400 nm), ultraviolet-visible (UVIS, 400-800 nm), NIR and SWIR. Combined with TROPOMI's high spectral resolution, these wavelengths allow for the observation of key atmospheric gasses. TROPOMI's spectral properties are summarized in Table 2.3. TROPOMI has a swath width of 2600 km across 450 pixels, which allows for daily global coverage. It operates in a push-broom configuration with a measurement period of one second, where light from the whole swath is collected simultaneously for one second and dispersed onto the imaging sensor. At TROPOMI's orbital velocity, this results in a pixel size of 7×5.5 km^2. [71]

Table 2.3: Summary of TROPOMI's spectral properties. [72]

TROPOMI band	**Spectral range [nm]**	**Type**	**Product(s)**	**Spectral resolution [nm]**	**Nadir spatial resolution [km^2]**
1	267-300	UV	Ozone, sulfur dioxide	0.45 - 0.5	5.5 x 28
2	300-332	UV	Ozone, formaldehyde	0.45 - 0.5	5.5 x 3.5
3	305-400	UVIS	Ozone, nitrogen dioxide	0.45 - 0.65	5.5 x 3.5
4	400-499	UVIS	Ozone, formaldehyde, nitrogen dioxide	0.45 - 0.65	5.5 x 3.5
5	661-725	NIR	Aerosols	0.34 - 0.35	5.5 x 3.5
6	725-786	NIR	Clouds	0.34 - 0.35	5.5 x 3.5
7	2300-2343	SWIR	Methane, carbon monoxide	0.227	5.5 x 7
8	2343-2389	SWIR	Methane, carbon monoxide	0.225	5.5 x 7

Since the start of data collection in 2018, TROPOMI has been used to study various greenhouse gasses. Examples include mapping the decrease in nitrogen dioxide (NO_2) pollution due to the COVID pandemic in 2020 [73] and global-scale sulfur dioxide emissions due to combustion of fossil fuels [74]. Methane emissions have been quantified on global-, country- [75, 76] and regional-scales, such as the Permian basin (the highest-producing oil field in the US) [77–79]. So-called "super-emitters" (large methane point sources) have been detected from natural gas well blowouts [80, 81] and landfills [82]. In addition, SRON has used TROPOMI data in combination with a machine learning approach to automatically detect methane plumes on a global scale on a weekly basis. Figure 2.10 shows the results of these automated detections for week 37 of 2024. Hotspots are visible along natural gas pipelines in Russia, near the oilfields of Turkmenistan and Kazakhstan, and in the Permian basin in Texas, US.

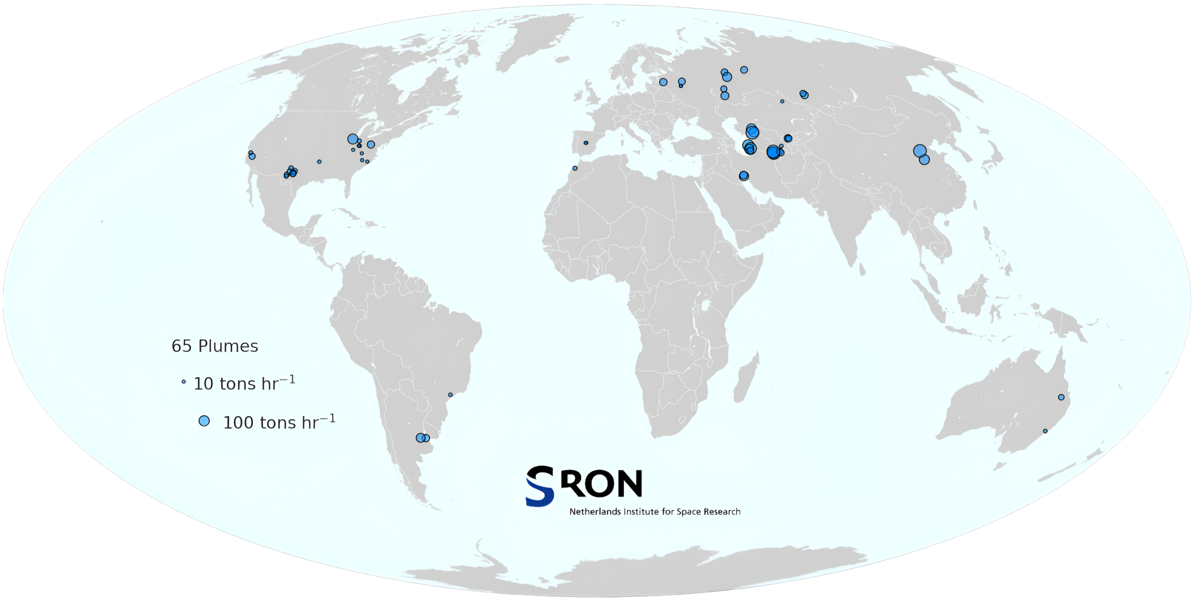

Figure 2.10: TROPOMI-detected methane plumes from 7-13 September, 2024. In total, 65 plumes with source rates between 10 and 100 t/h were detected in week 37 of 2024. [65, 83]

2.3.3. Geostationary Operational Environmental Satellite (GOES)

Built by NASA and operated by NOAA, the GOES program consists of four geostationary Earth-observation satellites (GOES-14: inactive, GOES-15: inactive, GOES-16: active, GOES-17: active) that provide atmospheric monitoring data for hurricane and severe storm tracking, wildfire detection and monitoring, cloud detection, air quality data, vegetation monitoring, lightning strike monitoring and volcanic eruption detection. Combined, the GOES constellation can monitor the entire western hemisphere, as shown in Figure 2.11 GOES-16 (henceforth called GOES, unless otherwise specified) covers almost the entire North and South American continents. GOES' wide range of applications comes courtesy of the Advanced Baseline Imager (ABI) instrument, which views the Earth in 16 separate spectral bands (2 visible, 4 near-infrared and 10 infrared bands). Table 2.4 shows the properties of each band and their use case (nickname). ABI's spectral resolution varies from 0.5 km (band 2) to 2 km (multiple bands) at nadir.

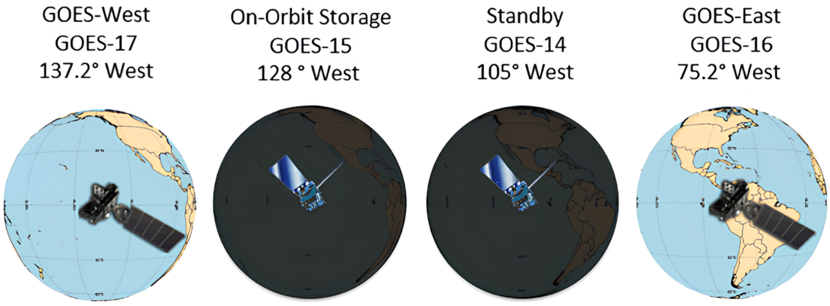

Figure 2.11: Spatial coverage of the GOES constellation. The dark globes for GOES-15 and GOES-14 indicate they are inactive. [84]

Table 2.4: Summary of ABI's spectral properties. [85]

ABI Band	Central Wavelength (µm)	Type	Nickname	Best Spatial Resolution (km)
1	0.47	Visible	Blue	1
2	0.64	Visible	Red	0.5
3	0.86	Near-Infrared	Veggie	1
4	1.37	Near-Infrared	Cirrus	2
5	1.6	Near-Infrared	Snow/Ice	1
6	2.2	Near-Infrared	Cloud particle size	2
7	3.9	Infrared	Shortwave window	2
8	6.2	Infrared	Upper-level water vapor	2
9	6.9	Infrared	Midlevel water vapor	2
10	7.3	Infrared	Lower-level water vapor	2
11	8.4	Infrared	Cloud-top phase	2
12	9.6	Infrared	Ozone	2
13	10.3	Infrared	"Clean" longwave window	2
14	11.2	Infrared	Longwave window	2
15	12.3	Infrared	"Dirty" longwave window	2
16	13.3	Infrared	CO2 longwave	2

The ABI measures incoming electromagnetic radiation energy (radiance) across its 16 spectral bands. When incoming photons strike the ABI's detectors, they generate an electrical current which is proportional to the intensity of the incoming light. ABI's electronics then convert this current into a digital signal, which is transmitted to the Earth using radio antennas. The ABI scans the Earth's surface using two scanning mirrors: one that moves from north to south and one that moves from west to east. These mirrors are shown in Figure 2.12. Once a west-to-east scan is completed, the north-to-south mirror moves downwards to begin a new scan. Depending on ABI's scanning mode, it can provide data of any location in the Western hemisphere between 30 seconds and 10 minutes. This is at least two orders of magnitudes higher than what is possible with LEO satellites. [86, 87]

Using GOES for methane emission detection also comes with a major downside. GOES is a band-imager with a coarse spectral resolution of 40-50 nm so its methane sensitivity is very low. This spectral resolution allows only the detection of the largest methane enhancements. Figure 2.13 shows the overlap between ABI's band 5 (1590-1630 nm) and band 6 (2220-2270 nm) with methane's SWIR absorption lines. [1]

GOES satellites are not the only geostationary Earth-observation satellites in orbit. Notable other examples are Japan's Himawari 8 (coverage over Eastern Asia, Oceania and Australia) and Europe's Meteosat Third Generation constellation (coverage over Europe, Africa and the Middle East). GOES-16 has been specifically selected for this thesis for its spatial coverage above North and South America (75.2°W), where countries like the USA, Canada and Brazil produce 30% of the global O&G supply [88]. This makes it a relevant area to monitor methane emissions. [1]

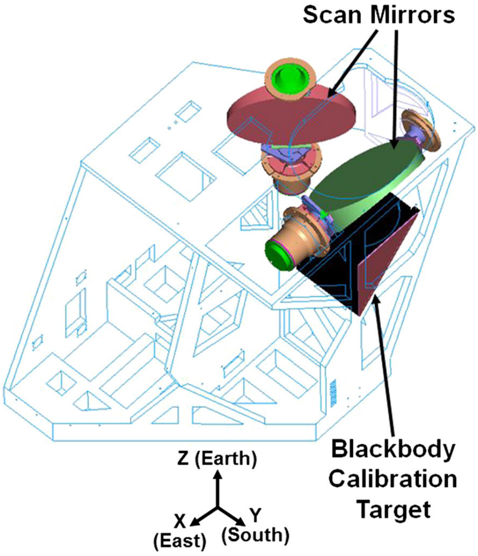

Figure 2.12: GOES' Advanced Baseline Imager double scanning mirror setup. [89]

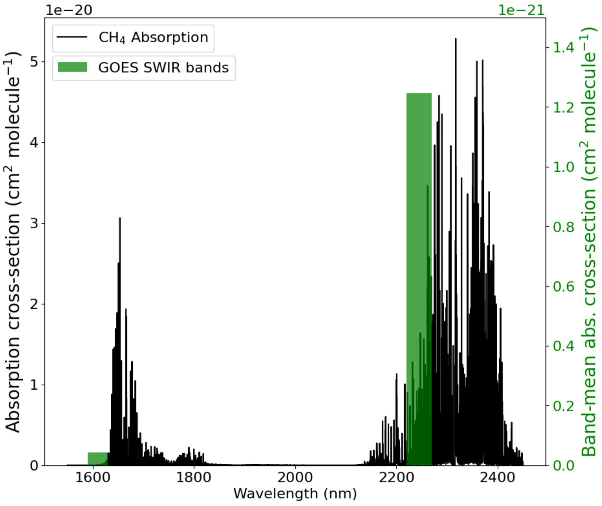

Figure 2.13: Average methane absorption cross-section in GOES bands 5 (1590-1630 nm) & 6 (2220-2270 nm) and methane absorption spectrum in the SWIR range. [1]

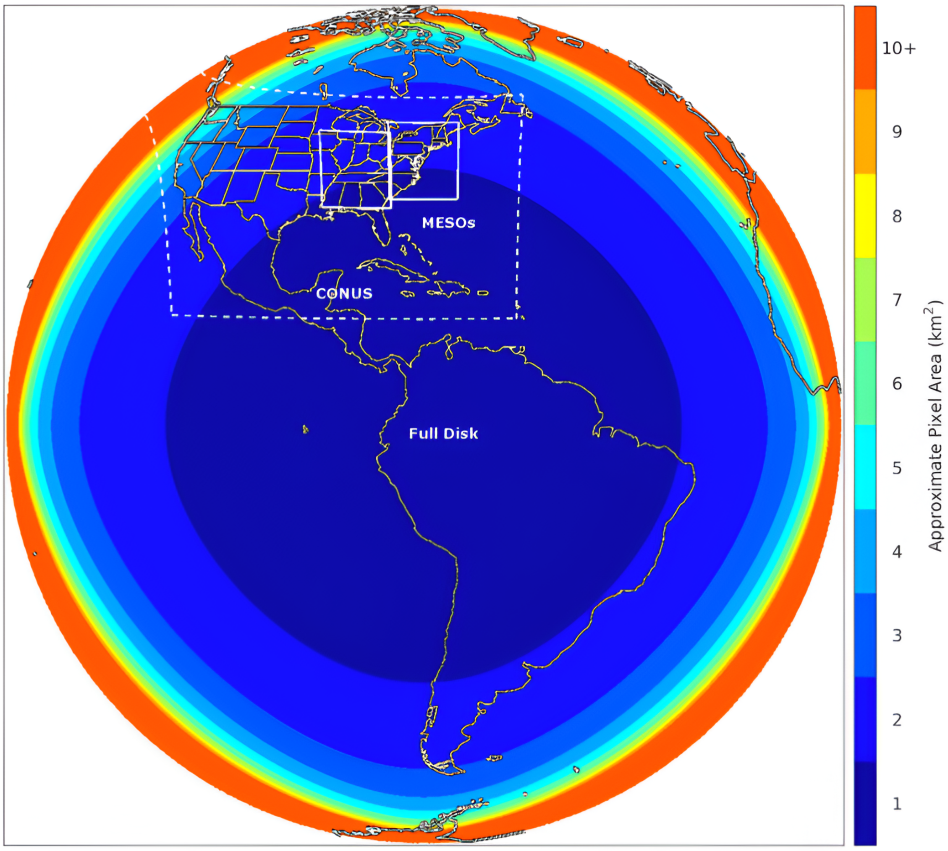

Figure 2.14: Pixel area distribution in GOES' geostationary field of view for band 5 resolution. The differences are caused by the curvature of the Earth and GOES' geostationary perspective. Band-5 and band-6 pixels have 1 x 1 km^2 and 2 x 2 km^2 resolution at nadir, respectively. Hence, band 6 pixel area will be coarser by a factor of 4 than presented here. [90]

3

Research definition

This chapter formulates the main research question and subquestions based on the theoretical background of Chapter 2. The context and significance of the research are also discussed.

3.1. Research context

In November 2023, [1] became the first research group to demonstrate GOES' ability to perform methane leak detection. Since this was the first publication that demonstrated the repurposing of GOES' radiance data to detect methane emissions, gaps in the research field remain. Firstly, GOES' ability to quantify methane plumes under varying environmental conditions remains unclear. In addition, a comprehensive characterization of when and where GOES can be used to detect emissions has also not yet been investigated. This thesis aims to fill in these gaps in the scientific knowledge.

This study is performed at the Earth science group of SRON Netherlands Institute for Space Research in Leiden, Netherlands. SRON is the Dutch national expertise institute for space research, as part of the Dutch Research Council (NWO). SRON has years of experience in atmospheric methane monitoring and is a co-principal investigator of the world-leading TROPOMI instrument.

3.2. Research questions

Main research question:

How can existing geostationary satellite data be used to improve quantitative methane leak monitoring over North America?

Subquestions:

1. **How accurately can GOES quantify methane emissions under varying environmental conditions?**

   GOES is a new instrument in the field of methane emission detection and its ability to quantify methane plumes has not yet been demonstrated at a large scale. Assessing the accuracy of GOES quantifications is important to understand if GOES' estimates are useful in reporting methane emissions. To answer this research question, methane plumes with known source rates are simulated and converted into GOES' B5 and B6 radiances. These radiances can then be used to quantify the original plume. Comparing the simulated source rate to the source rate that is derived from the synthetic radiances will show how accurately GOES can quantify methane emissions.

2. **What is the methane emission detection limit of GOES?**

Another unanswered question is under which conditions GOES can be used to detect emissions and how this compares to other methane-sensing satellites. To this end, a detection limit can be used to describe the smallest source rate that can be detected by GOES. The detection limit depends on environmental conditions such as albedo and wind speed, so it is not a representative metric to be used. Instead, the probability of detecting a methane plume under varying environmental conditions is a more robust metric. Based on a small number of GOES detections of transient point sources, [1] roughly estimated the detection limit to be between 10 to 100 $\mathrm{t\,h^{-1}}$. This thesis aims to refine this estimate and quantify the probability of detecting methane plumes with GOES. This is an important result since it yields the minimum required source rate for a certain probability to be detected. No other estimates have been published on GOES' detection limit and probability of detection. [1]

3.3. Significance and novelty

Due to methane's high GWP and short lifetime, decreasing atmospheric methane emissions is an urgent priority to slow climate change in the near future. The current methane-observing satellite fleet has revisit times in the order of days, which may result in missed emissions from short and intermittent leaks. Using GOES for methane retrievals offers, for the first time, a five-minute temporal resolution in methane emission detections. This creates the potential for increased emissions detections and a better understanding of the temporal variability in the emission rate.

Part II

Methodology

4

Set-up of methodology

The methodology consists of two main components: the forward environment and the inverse environment. This terminology follows the causality of methane concentrations resulting in radiances with absorbed wavelengths (forward direction), which can be used to retrieve back the corresponding methane concentrations (inverse direction). This is visualized in Figure 4.1.

The forward and inverse environments are jointly used in the two main components of this thesis: the Observation System Simulation Experiment (OSSE, see Chapter 7) and the Probability of Detection curves (POD, see Chapter 8). These components largely use the same methodology but focus on answering different research questions. The methodology steps for each component are explained in subsequent chapters.

In the forward environment, the Hybrid Single-Particle Lagrangian Integrated Trajectory model (HYSPLIT, [91]) will be used to model the atmospheric transport of a methane emission event with known source rate $\mathrm{Q_{sim}}$ under predefined meteorological conditions. For each plume, this results in a spatial and temporal distribution of the methane column concentrations $\mathrm{X_{CH_4}}$. After resampling the simulated coordinate grid to GOES' geostationary coordinate grid at a specific target location, a forward radiative transfer (RT) model calculates the integrated radiances in GOES' B5 and B6 that would be caused by the simulated plume. In the inverse environment, these radiances are used to retrieve back the methane enhancements. The accuracy and consistency of this retrieval step are assessed by comparing the retrieved enhancements to the simulated enhancements, which is marked as verification step A in Figure 4.2, and is critical to successfully detecting a plume with GOES. A binary plume mask is then applied to the retrieved enhancements to separate the plume from the background enhancements, and the source rate of the resulting mask can be quantified using a quantification method. The completeness of the plume mask and the accuracy of the quantification method are assessed by comparing the derived source rate Q_{der} to the simulated source rate Q_{sim}, which is marked as verification step B in Figure 4.2.

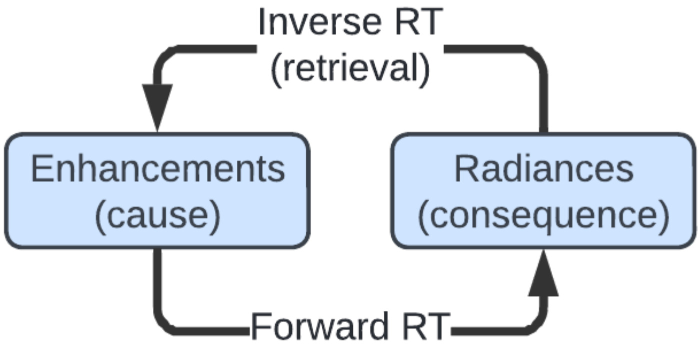

Figure 4.1: Overview of radiative transfer directions and terminology.

Each relevant verification plot will have step A or B in its title for context. In addition, by changing the input parameters to the retrieval (the selected reference day) and the plume masking algorithm (the plume masking thresholds), the sensitivity of the source rate quantification to the input parameters can be assessed. In the case of the POD, many methane plumes are simulated under varying conditions to create probability of detection curves that indicate GOES' probability of detecting a methane plume under certain environmental conditions. These curves are compared to real-life GOES detection results of TROPOMI reference detections. A full overview of the methodology is given in Figure 4.2.

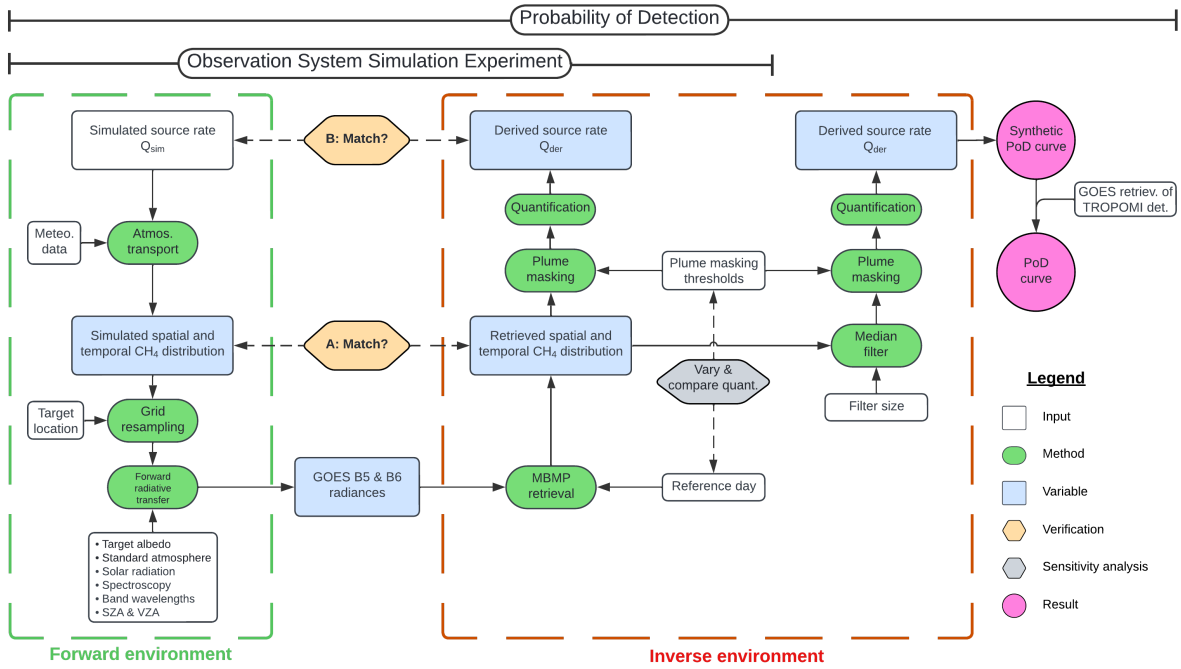

Figure 4.2: Flow diagram of the methodology for the Observation System Simulation Experiment and GOES' Probability of Detection curve.

5

Methodology in the inverse environment

This chapter presents the existing methodology in the inverse environment, following the green ellipses in Figure 4.2. Section 5.1 introduces how methane enhancements are retrieved from GOES' radiance data. Section 5.3 presents how a plume is separated from the background enhancements. Two different methods to quantify the source rate of a plume are introduced in Section 5.4.

5.1. Methane column retrieval method

This section explains how methane enhancements concentrations $\Delta\Omega$ (molm^{-2}) are retrieved from GOES' TOA SWIR radiance data using the multi-band-multi-pass retrieval method, which uses the multi-band-single-pass retrieval method. Both methods rely on the differences between two spectral measurements of the same location, one with methane absorption and one without, to retrieve vertical column enhancements. Since GOES only observes TOA reflectances, methane enhancements in the entire vertical column are retrieved.

5.1.1. Multi-band-single-pass retrieval

The first part of the methane column concentration retrieval method is the multi-band-single-pass (MBSP) retrieval [42]. The MBSP retrieval derives methane column enhancements from the fractional change in reflected sunlight, known as reflectance, between two spectral band measurements from a single overpass of the same location. The principle behind this approach is to derive methane column concentrations from the differences between the two measurements. Hence, the spectral bands are selected such that one has strong methane absorption properties (due to a high methane absorption cross-section), while the other has low or no methane absorption properties (due to a low methane absorption cross-section). In addition, reflectances due to surface albedo and aerosols (e.g. smoke, dust, particulate matter) vary with wavelength so the spectral bands must be as close to each other as possible to minimize any non-methane-related reflectance differences. Here, GOES' B5 and B6 are used as the methane insensitive and sensitive band, respectively (see Figure 2.13).

Using the reflectances R_5 and R_6 from B5 and B6, respectively, the fractional change in reflectance ΔR is given by:

$$\Delta R_{\mathrm{MBSP}} = \frac{cR_6 - R_5}{R_5}, \tag{5.1}$$

where c is an empirical scaling factor that removes the spectral dependence of surface albedo and is calculated by least-squares fitting all B6 values against all B5 values. Even though the MBSP approach relies on the similarity of albedo and aerosol reflectance between the two spectral band measurements, this scaling prevents any differences caused by these from being interpreted as due to methane absorption. Albedo's spectral dependence is assumed to be uniform across the scene of interest. Since GOES' B5 and B6 have different spatial resolutions (1x1 km^2 and 2x2 km^2 at nadir, respectively), B5 data are coarsened by a factor 4 prior to calculating Equation 5.1.

Next, the methane column enhancement $\Delta\Omega$ is inferred by comparing ΔR_{MBSP} through a lookup table to a simulated ΔR from a radiative transfer model $\mathrm{m_{MBSP}}(\Delta\Omega)$:

$$m_{MBSP}(\Delta\Omega) = \frac{T_6(\Omega + \Delta\Omega) - T_6(\Omega)}{T_6(\Omega)} - \frac{T_5(\Omega + \Delta\Omega) - T_5(\Omega)}{T_5(\Omega)}, \tag{5.2}$$

where $\mathrm{T_N}$ is the modeled TOA reflectance in band N. The purpose of the radiative transfer model is to create a look-up table that maps ΔR to $\Delta\Omega$. The simulated reflectances are sampled at a very high spectral resolution and integrated over GOES' B5 and B6 spectral ranges. The model uses the U.S. Standard Atmosphere for vertical profiles of pressure, temperature, air density, water vapor, carbon dioxide and background methane (0.65 mol m^{-2} in the vertical column) [92, 93]. The absorption spectra of carbon dioxide, carbon monoxide, water vapor, nitrogen dioxide and methane are from the HIgh-resolution TRANsmission molecular absorption database (HITRAN2016) [94]. Incident solar radiance measurements from the Total and Spectral Solar Irradiance Sensor-1 (TSIS-1) satellite mission are used [95] and surface reflectances are assumed to be Lambertian, i.e. equal reflection per area in all directions. The model accounts for variable surface elevation, solar zenith angles and viewing zenith angles but assumes cloud-free conditions as they inhibit reflectances. The effects of aerosols are not taken into account since aerosols are generally not emitted alongside methane.

The final step to retrieve methane column enhancements is to minimize the cost function C($\Delta\Omega$), which is defined as the difference between the fractional change in reflectance ΔR_{MBSP} and the fractional absorption model m($\Delta\Omega$):

$$C(\Delta\Omega) = \Delta R_{\mathrm{MBSP}} - m_{\mathrm{MBSP}}(\Delta\Omega). \tag{5.3}$$

The $\Delta\Omega$ that minimizes C($\Delta\Omega$) is the retrieved methane column enhancement. m_{MBSP} values may be interpolated to minimize C($\Delta\Omega$). This process is repeated for all pixels in the scene of interest.

The MBSP approach has the advantage of using spectral measurements from only a single overpass, which eliminates reflectance differences due to changing solar zenith angles, surface conditions or atmospheric conditions. The disadvantage is that it uses reflectances from spectral bands whose central wavelengths are separated by 635 nm. This separation introduces systematic errors and artefacts (areas that are incorrectly interpreted as methane) in the retrieval, which complicates the quantification of the methane emission.

5.1.2. Multi-band-multi-pass retrieval

To correct for the systematic errors and remove the artefacts from the MBSP retrieval $\Delta\Omega_{\mathrm{MBSP}}$, the multi-band-multi-pass (MBMP) method [42] subtracts a reference MBSP retrieval $\Delta\Omega'_{\mathrm{MBSP}}$ for an overpass without a methane plume:

$$\Delta\Omega_{\mathrm{MBMP}} = \Delta\Omega_{\mathrm{MBSP}} - \Delta\Omega'_{\mathrm{MBSP}} \tag{5.4}$$

Assuming the systematic errors are similar on both overpasses, the subtraction in the MBMP retrieval leaves only the true methane enhancement. The retrieval from the overpass with the plume is called the target retrieval, while the overpass without the plume yields the reference retrieval.

The reference retrieval must contain no methane plume since that absorption would introduce new artefacts in the retrieval. In addition, any changes in surface reflectance between the target and reference retrievals can introduce new artefacts. For example, when the scene of interest contains farmland, a change in verdure due to a rain shower between the target and reference overpasses can cause artefacts in the MBMP retrieval. Selecting a reference day that is as close as possible to the target day is preferable but may be challenging in areas with frequent cloud cover. When the differences between the target and reference days are too significant, the MBSP retrieval may be superior.

To illustrate the MBSP and MBMP retrieval methods, Figure 5.1 shows the difference between them with band 12 and band 11 data from the Sentinel-2A satellite for a methane emission event in Algeria. Even though Sentinel-2A's spectral bands are named differently than GOES', their spectral ranges strongly overlap with GOES' B6 and B5, respectively. The band 12 measurements in (**a**) show a plume emanating from the center of the scene in northward direction. This is not visible in band 11 in (**b**) due to its weaker methane absorption. The MBSP retrieval in (**c**) shows a clear plume in northward direction but also strong artefacts. The MBMP retrieval in (**d**) produces the clearest methane plume and eliminates the most artefacts; this is a highly desirable result for further quantification and analysis. The precision of the column retrieval can be estimated using the standard deviation of the enhancements outside of the plume, assuming the instrument noise is normally distributed and uncorrelated. The precision is 0.31 mol m^{-2} for the MBSP retrieval (48% of the background) and 0.13 mol m^{-2} for the MBMP retrieval (21% of the background); this shows the superiority and finer precision of the MBMP method in this scenario. [42]

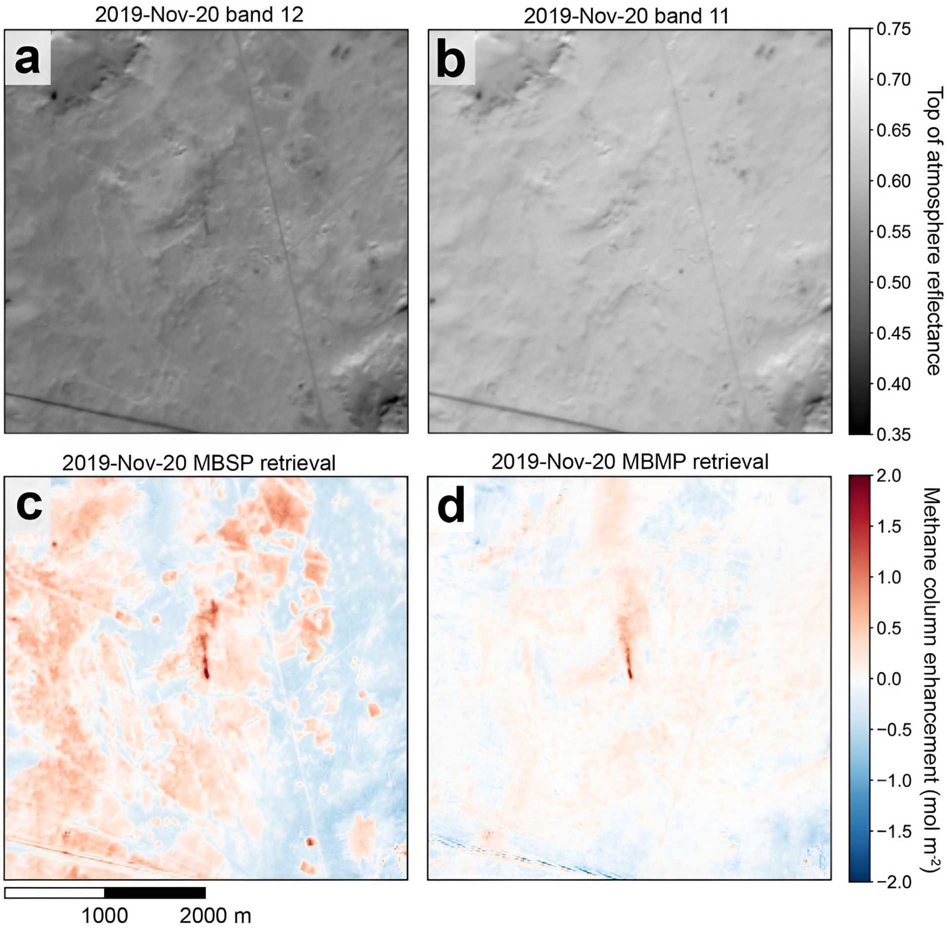

Figure 5.1: Comparison between MBSP and MBMP methane column retrievals for a plume from a point source. Data from ESA's Sentinel-2A satellite in the Hassi Messaoud oil field in the Algerian desert on November 20, 2019. (**a**) and (**b**) show band-12 (2115-2290 nm) and band-11 (1568-1659 nm) TOA radiances. Note the presence of a plume near the center of the scene in band 12 (methane-sensitive band), while it is not present in band 11 (methane-insensitive band). (**c**) and (**d**) show the MBSP and MBMP methane column retrievals, respectively. Adapted from [42].

5.2. Median filter

A median filter is applied to the retrieved enhancements to recenter the distribution around 0 mol m^{-2}. This step is crucial to improve the plume masking (see Section 5.3) since a lower background makes the plume enhancements more apparent and easier to mask. The median filter depends on a square filter size, expressed in a number of pixels. A sensitivity analysis on the filter size and the resulting recentered enhancements showed that 20 pixels was adequately removed the background enhancements while minimizing the effect on the plume. The usefulness of other filter types, such as Gaussian filters, can be investigated in future work.

5.3. Plume masking

In the final step before a plume can be quantified, binary plume masking identifies the methane plume in the retrieved enhancements and separates it from the background by including all pixels above a certain lower enhancement percentile, while ignoring enhancements below it. This method relies on the fact that plume enhancements are outliers compared to the background values. Plume masking is necessary because artefacts and noise in the retrieved enhancements due to clouds, waterbodies or albedo differences make it impossible to calculate the total methane emission by summing all enhancements across the scene. This would only be possible in an ideal retrieval in which no methane enhancements are retrieved anywhere outside of the true plume, but this is made impossible by differences in albedo between the target and reference days (see Section 5.1). This emphasizes the importance of the albedo similarity of the target and reference days.

Plume masking becomes more difficult when there are many artefacts and high noise levels in the retrieval. These originate when the available radiance data does not have a high enough spectral resolution to accurately retrieve methane concentrations. Higher plume enhancements and lower noise levels improve the masking result. As a result, GOES is a very challenging instrument due to its low spectral resolution and methane sensitivity. Determining the full extent of the mask in the retrieved enhancements is thus non-trivial and it is common for studies to manually intervene to improve the plume masking results [1, 62]

The used masking algorithm is explained below per step:

0. It is assumed that the source location is (approximately) known beforehand, but the start time is not. The necessary inputs to the algorithm are **a lower threshold percentile, an upper threshold percentile, a spatial buffer around the source location and the spatial and temporal distributions of retrieved enhancements**.
1. At any timestamp, **an enhancement value is calculated based on the upper threshold percentile**. Since the plume enhancements are outliers compared to the background, a high percentile acts as a cut-off value below which enhancements are not included in the plume. **If there are one or more retrieved pixels inside the variable pixel buffer around the (approximate) source location that exceed the upper threshold value, this means strong enhancements are emitted by the source and so these pixels are included in the binary plume mask** (equated to 1). **All pixels below the threshold are excluded** (equated to 0). If no plume pixels are detected, this step is repeated indefinitely for each timestamp until high enhancements are found around the source location. However, once plume pixels are detected, step 2 is performed
2. If plume pixels are detected around the source location, this means an emission event has started. For each consecutive timestamp, a lower percentile is used as the cut-off value for new pixels to be included in the mask, as defined by a lower threshold percentile. In the case of a single, constant emission, the plume pixels must be connected and are transported by the wind. Hence, **only pixels that exceed the lower threshold and are adjacent to one of the plume pixels in the previous timestamp are also included in the plume mask.** Any pixel that does exceed that threshold but is not connected to the previous mask, is not included to prevent retrieval noise

and artefacts from seeding plume pixels at locations away from the source. This step is repeated for each timestamp.

3. Over time, the dispersion of the plume decreases the concentration of the enhancements until they no longer exceed the background concentration. These pixels can thus no longer be masked.

Figure 5.2 shows an example of plume masking results for retrieved enhancements and demonstrates the sensitivity of the mask to the chosen lower threshold.

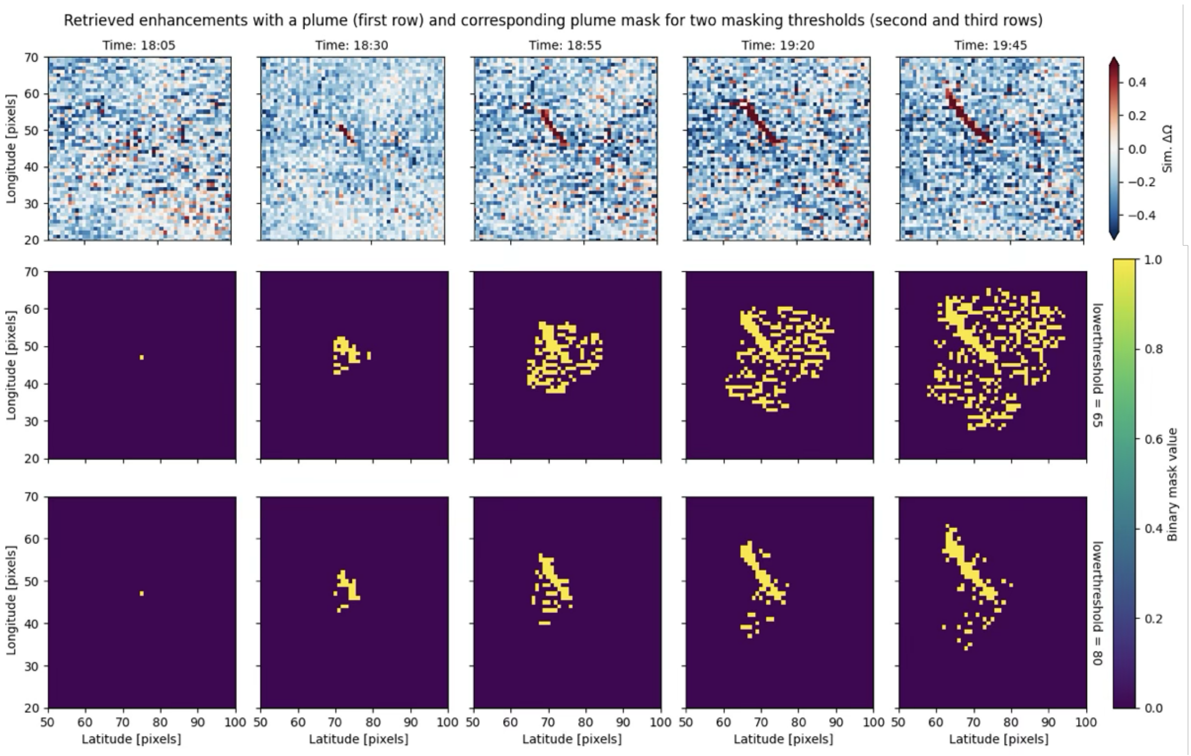

Figure 5.2: Demonstration of the effect of different masking thresholds on the plume mask for retrieved enhancements. The retrieved enhancements span two hours between 18:00 and 20:00 (first row) and originate from a simulated plume at 2000 th^{-1}. The plume is visible by the bright red enhancements and develops over time. The blue and white non-plume pixels are the retrieval artefacts and noise. Two corresponding binary plume masks are shown for a lower masking threshold of the 65th and the 80th percentile in the second and third rows, respectively. The 65th percentile is too low since the mask includes many non-plume pixels. This is improved for the 80th percentile, which contains far fewer non-plume pixels.

5.4. Source rate quantification methods

Quantifying methane emissions can refer to two distinct metrics: (1) the total amount of emitted methane by a source, also called the Integrated Methane Enhancement (IME, t), or (2) the source rate, referred to as Q (t h^{-1}). Two methods to quantify source rates are presented here: the IME method and the d(IME)/dt method, although more quantification methods exist. These methods are described in Section 5.4.1 and Section 5.4.2, respectively, and are based on [96] and [1], respectively.

5.4.1. Integrated mass enhancement method

Generally speaking, a detected plume will cover N pixels of area $\mathrm{A_j}$ [m^2] with enhancements $\Delta\Omega_j$ [mol m^{-2}] (j=1,...,N). In this case, the IME is defined as the sum of the product of each pixel area with its corresponding enhancement, multiplied by methane's molar mass $\mathrm{m_{CH_4}}$:

$$\mathrm{IME} = \mathrm{m}_{\mathrm{CH}_4} \sum_{j=1}^{N} \Delta\Omega_j A_j. \tag{5.5}$$

Note that an instantaneous detection only has a single snapshot of the plume and thus can deduce no information on the variability of the source rate. This IME method thus has to assume a constant source rate during the emission.

Next, the source rate Q is defined by dividing the IME by the residency time τ of methane in the plume:

$$Q = \frac{IME}{\tau} \tag{5.6}$$

τ can be expressed using the effective wind speed $\mathrm{U}_{\mathrm{eff}}$ $[\mathrm{ms}^{-1}]$ and the plume size L [m]:

$$Q = \frac{1}{\tau}\mathrm{IME} = \frac{U_{\mathrm{eff}}}{L}\mathrm{IME} = \frac{\mathrm{m}_{\mathrm{CH}_4}\mathrm{U}_{\mathrm{eff}}}{L} \sum_{j=1}^{N} \Delta\Omega_j A_j \tag{5.7}$$

Plume transport is a non-laminar, turbulent and diffusive process due to vertical atmospheric transport, surface roughness and changing wind directions. This means $\mathrm{U}_{\mathrm{eff}}$ and L cannot have the simple physical meaning of wind speed and plume length since the plume dissipation occurs in all directions (not only in the downwind direction). This effect should be compensated for by introducing $\mathrm{U}_{\mathrm{eff}}$ and L as effective parameters which have the correct dimensions to calculate the source rate but need to be calibrated to account for turbulent plume transport due to plume diffusion in multiple directions.

Part of the calibration process of $\mathrm{U}_{\mathrm{eff}}$ and L is simulating plumes in a large eddy simulation (LES). This aspect is beyond the scope of this thesis; please refer to [96] for more information. The calibration of $\mathrm{U}_{\mathrm{eff}}$ is important and its purpose is to find valid values for $\mathrm{U}_{\mathrm{eff}}$ to account for turbulence in the plume diffusion. The two most important points are:

1. **Plume length L:** L can be expressed as the square root of the plume mask area A_{M}:

   $$L = \sqrt{A_M} \tag{5.8}$$

   The exact definition of L is not important since it is an effective parameter which needs to be consistent with the effective calibration. A different definition of L implies a different calculation of $\mathrm{U}_{\mathrm{eff}}$.

2. **Effective wind speed $\mathbf{U}_{\mathbf{eff}}$:** The effective wind speed can be calibrated against simulated 10-m altitude wind speeds U_{10} at the location of the source from meteorological models. Two possible wind speed data sources are NASA's GEOS-FP wind data [97] and the EU's Copernicus program's ERA5 wind data [98]. The external wind product is a major source of uncertainty in the source rates estimated from instantaneous detections, with wind speed estimation errors ranging from 15% to 50% [96]. During the calibration process, a set of LESs is used to derive the relationship between $\mathrm{U}_{\mathrm{eff}}$ and U_{10}:

   $$U_{\mathrm{eff}} = \alpha_1 \log U_{10} + \alpha_2, \tag{5.9}$$

   where α_1 and α_2 are the result of a logarithmic data fit. This result is shown in Figure 5.3.

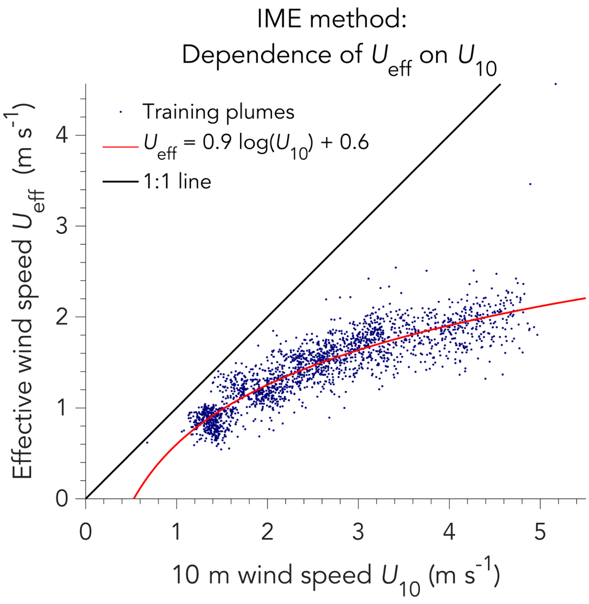

Figure 5.3: Demonstration of the logarithmic dependence between effective wind speed U_{eff} and 10m wind speed in the IME method from simulated LES data. Each point represents a simulated LES plume. The red line shows the least-squares logarithmic fit to the LES data. [96]

With estimates for U_{eff} and L, Equation 5.7 can be used to determine the source rate Q.

5.4.2. d(IME)/dt method

Continuous detections from a geostationary satellite enable an entirely novel source rate quantification method. This subsection introduces this new method and explains how it circumvents a major limitation of the IME method.

Leveraging the five-minute temporal resolution of GOES, variable source rates Q can be determined by computing the rate of change of the IME over time:

$$Q = \frac{\mathrm{d}(IME)}{\mathrm{d}t} \tag{5.10}$$

This method is a very recent development in the field of satellite-based emission detection. The only study to employ this method was published in November 2023. The advantage of this technique is that it does not need an external wind data product to quantify the source rate, and thus eliminates the corresponding wind speed errors (see Section 5.4.1). The downside is that it cannot be applied to instantaneous detections by LEO satellites due to their lack of temporal data. [1]

6

Methodology in the forward environment

This chapter presents the methodologies behind the Observation System Simulation Experiment (OSSE) and the Probability of Detection (POD) curve that were developed in the context of this thesis research in the forward environment. The OSSE, presented in Section 6.1, uses simulated methane plumes to verify the functioning of GOES' methane plume retrieval methodology. The background behind the OSSE is introduced in Section 6.1.1 and Section 6.1.2 explains the methods used to simulate methane plumes, simulate their corresponding radiance values and retrieve back enhancements. The OSSE consists of four cases which collectively aim to demonstrate the correct functioning of the retrieval and quantification pipeline. These cases are described in Section 6.1.3. The POD curve characterizes GOES' probability of detecting methane plumes under varying conditions. Section 6.2.1 explains the mathematical derivation of the POD and the reasons behind creating nine separate POD formulations. Section 6.2.2 and Section 6.2.3 introduce the three locations and three albedo backgrounds that are considered for these formulations.

6.1. Observation System Simulation Experiment

6.1.1. Background

OSSEs are used to test current or future satellite missions and assess the sensitivity of their results to new data. By using simulated data, they can demonstrate the usefulness and value of candidate future missions, prepare the data processing pipeline and study error propagation. The OSSE presented here consists of retrieving methane enhancements from synthetic radiances based on simulated methane plumes. This allows the performance of the retrieval methodology to be assessed by comparing the methane mass and source rate quantifications obtained from the simulated plume to the known input of the simulation.

6.1.2. Methods

The forward environment contains three main methods, as shown by the green ellipses in Figure 4.2:

1. **Atmospheric transport:** HYSPLIT is used as an atmospheric transport modeling tool to simulate methane plumes using meteorological data in the forward environment;
2. **Grid resampling:** Resampling is required to move the simulated methane enhancements from

HYSPLIT's rectangular coordinate grid to GOES' variable pixel-size coordinate grid;

3. **Forward radiative transfer:** This model calculates the integrated synthetic radiances in GOES' B5 and B6 from $\Delta\Omega$ in the forward environment;

6.1.2.1. Atmospheric transport

To create simulated methane plumes, HYSPLIT is used to model the atmospheric transport and dispersion of a plume with known source rate Q_{sim}. HYSPLIT was developed by the Australian Bureau of Meteorology Research Center and NOAA Air Resources Laboratory in 1998. It is a so-called hybrid model because it uses both Eulerian and Lagrangian atmospheric dispersion modeling methods. It requires meteorological data as input with, at a minimum, information on the two-dimensional velocity components in eastward and northward directions, temperature, altitude, pressure and surface pressure [91]. For the mathematical foundations behind the Eulerian and Lagrangian modeling methods, the reader is referred to [99].

Applications and limitations

HYSPLIT is a frequently used tool to model atmospheric processes for research and emergency response purposes. Applications include backtracking emissions to find the emission source, predicting wildfire smoke pollution and forecasting radiological contamination. HYSPLIT has been validated by high-altitude balloon trajectories, ash plumes of volcanic eruptions and radiological contamination from the Chernobyl accident in 1986. [91]

Understanding HYSPLIT's limitations is important to assess the validity of the OSSE set-up. The most important limitations are [100]:

- The coordinate grid of HYSPLIT's output can only be rectangular in latitude-longitude space. This necessitates the grid resampling from the simulation grid to the GOES grid since the pixels in the GOES grid are not rectangular due to its geostationary viewing angle (see Figure 2.11).
- HYSPLIT cannot model time-variable source rates so the source rate is constant during the emission event. In real-life, emissions are often intermittent with variable source rates [101].
- HYSPLIT is unable to model atmospheric chemical reactions. It can model the transport of methane in the atmosphere but it cannot, for example, account for the decay of methane concentration due to oxidation by hydroxyl radicals and dry soils (see Section 2.1.3).

Set-up and inputs

Table 6.1 lists the input settings for HYSPLIT to simulate methane plumes. The source location is in Coahuila, Mexico, which was chosen to overlap with GOES' first published methane plume detection [1]. The starting time is 16:00 UTC, which, on average, coincides with the middle of the day for a two-hour emission duration in Mexico (UTC-5). The starting date, which affects the meteorological data, was chosen for its proximity to GOES' first published methane plume detection. The meteorological data is from ECMWF Reanalysis Version 5 (ERA5) by the European Centre for Medium-Range Weather Forecasts (ECMWF). ERA5 provides estimates for a large number of atmospheric parameters at one-hour temporal resolution, including two-dimensional velocity components in eastward and northward directions at 100-m resolution. Even though the vertical distribution of methane is modeled at six concentration levels, these levels are summed post-simulation to yield the methane column concentrations as observed by GOES.

Table 6.1: HYSPLIT settings for methane plume simulations.

Setting	Value	Setting	Value
Starting location (lat, lon, altitude)	27.82°N, -101.70°E, 10 m	Number of vertical conc. levels	6
Starting time	2019-09-24, 16:00 UTC	Height of each vertical level	10 m, 50 m, 100 m, 200 m 1500 m, 10000 m
Total run time	13 h	Sampling interval	5 min
Meteorological data input	ERA5, 2019-09-24	Number of pollutants	1 (CH_4)
Emission rate Q_{sim}	Variable in t h^{-1}	Deposition	No
Emission duration	2 h	Wet removal	No
Grid span	3° x 3°	Resuspension	No
Grid spacing	0.01° x 0.01°	Radioactive decay	No

Methane has an average lifetime of 9 years [7], which is beyond the scope of the simulation so the effects of atmospheric chemical reactions are negligible. In addition, the simulated area does not have large terrain differences and atmospheric deposition is not simulated. Space-based methane plume observations are only possible in cloud-free conditions so the lack of cloud-modeling in HYSPLIT is also not an issue. Hence, the limitations of HYSPLIT are deemed acceptable in this simulation.

6.1.2.2. Grid resampling

HYSPLIT can only output enhancements on orthogonal grids. Hence, the simulated grid and enhancements must be regridded (also called resampled) to the non-orthogonal, variable-size coordinate grid that GOES observes from its geostationary perspective to assess GOES' quantitative methane leak monitoring capabilities. The spatial resolution of the simulation grid is increased five times before resampling to minimize interpolation errors in the resampled enhancements.

6.1.2.3. Forward radiative transfer

A forward radiative transfer model $\mathrm{T}(\alpha, \lambda, z, \sigma_i, \mathrm{R}_0, \gamma_{SZA}, \gamma_{VZA}, \Delta\Omega)$ is used to convert the methane column enhancements $\Delta\Omega$ into TOA, outgoing radiances $\mathrm{R}(\lambda)$, where α is the surface albedo, λ is the wavelength, σ_i is the absorption coefficient of atmospheric gas i, R_0 is the TOA, incoming solar radiance, γ_{SZA} is the solar zenith angle and γ_{VZA} is the viewing zenith angle. The model assumes Lambertian reflection, the U.S. Standard Atmosphere and no light scattering [92, 93]. All contributions to the TOA outgoing radiance are ignored, other than the backscattered solar radiance.

The variables in the RT model allow retrievals to be made under simplified and real-life conditions. Two variables that dictate how representative simulation conditions are to real-world conditions are the albedo α and the methane enhancement concentration $\Delta\Omega$. The former can be set to a constant value across all wavelengths and the whole scene, creating highly simplified conditions. In reality, surfaces rarely have constant albedos due to vegetation, waterbodies and soil moisture. A representative albedo can be obtained from a non-enhanced scene in real-life GOES data.

6.1.3. OSSE set-up

To verify GOES' retrieval methodology, the OSSE will be split up in four cases. Starting from highly simplified retrieval conditions, the cases become more realistic and verify consecutive steps of the retrieval methodology. Combined, these cases explore the effects of different methane source rates, albedos, solar zenith angles, viewing zenith angles, plume masking thresholds, reference day selection and retrieval settings on the accuracy of the retrieval methodology. Section 6.1.3.1 to Section 6.1.3.4 outline the four cases, their retrieval settings and which step of the retrieval methodology is verified. Section 6.1.3.5 summarizes all cases.

In all cases, a two-hour methane emission event with a variable source rate is simulated using HYSPLIT (see Section 6.1.2.1). The duration is chosen to represent a brief emission, which may be caused by a real-life intermittent source. All simulated source rates are above 100 th^{-1}, such that they are all above GOES' predicted detection limit of 10 to 100 th^{-1} [1]. This ensures the probability of detecting a plume does not influence the verification results. These source rates are also representative of possible (high) source rates by real-life emission events [65]. In cases 1-3, the derived source rate is quantified using GOES' d(IME)/dt method (see Section 5.4.2), and in case 4, an optimal estimation algorithm is used to account for uncertainties in the IME.

6.1.3.1. Case 1: Assessing the consistency of the radiative transfer models

In case 1, plumes for different source rates are simulated using HYSPLIT. For each plume, the simulation outputs a spatial and temporal distribution of methane enhancements on an orthogonal coordinate grid with a 0.01° resolution (approximately $1\mathrm{x}1\mathrm{km}^2$). Following the flow of Figure 4.2, the simulated enhancements are resampled to GOES' coordinate grid. Next, the forward radiative transfer model converts these simulated enhancements to radiances in GOES' B5 and B6, after which the MBMP retrieval (inverse radiative transfer) retrieves back these enhancements on GOES' coordinate grid.

The goals of case 1 are to assess the consistency of the forward and inverse radiative transfer models and verify the accuracy of source rate quantifications under idealized and simplified retrieval conditions.

All retrievals in case 1 are performed under simplified conditions to isolate the effects of the enhancement type and coordinate grids. A uniform albedo is used across the scene, whereas, in reality, scene-wide albedo will vary due to changes in terrain and soil features. This uniformity means that the magnitude of reflectances is constant in areas without methane enhancements. Secondly, the target day (day with methane enhancement) is the same as the reference day (day without methane enhancement) in the MBMP retrieval. This simplification will result in a retrieval without noise or artefacts since the target and reference retrievals nullify outside of the plume.

Next, the empirical scaling factor from the MBSP retrieval on the reference day $\mathrm{c}_{\mathrm{ref}}$ (see Equation 5.1) is also used for the MBSP retrieval on the target day. The principle behind this forced calibration of $\mathrm{c}_{\mathrm{ref}}$ to the target day retrieval is that methane enhancements are more accurately interpreted from a least-squares fit to the radiances of a non-enhanced scene than an enhanced scene if there are no differences between the target day and reference day. The decreased B6 radiance values due to absorption in an enhanced scene will yield a lower slope of the least-squares fit than compared to a non-enhanced scene with absorption, which slightly biases the interpreted enhancements low. Under realistic conditions, when $\mathrm{c}_{\mathrm{ref}}$ and $\mathrm{c}_{\mathrm{target}}$ are used to remove scene-wide differences in surface albedo between B5 and B6, it is more accurate to interpret the enhancements from the least-squares fit on the target day because the spectral dependence of the albedo is more significant than the radiance differences due to the absorption. However, since the only difference between the target and reference days is the plume in this simplified case, it is more accurate to interpret enhancements from the non-enhanced scene and thus use $\mathrm{c}_{\mathrm{ref}}$ in the target day retrieval.

Furthermore, since the MBMP retrieval under these simplified conditions will contain no noise or artefacts and only one source is present in the scene, plume masking is not required and the source rate can be quantified by summing the methane enhancements across the entire scene.

Lastly, to assess the accuracy of the IME and derived source rate at different stages of the retrieval methodology, they are computed from the methane enhancements (simulated or retrieved) of one plume simulation at 500 th^{-1} on both coordinate grids (simulated or GOES). At these different stages, the IME is denoted by $\mathrm{IME}_{enh./grid}$, where *enh.* and *grid* are the type of enhancement and coordinate grid, respectively. The same holds for the derived source rate $\hat{\mathrm{Q}}$. For both IME and $\hat{\mathrm{Q}}$, three different combinations of enhancement and grid are considered at different stages of the retrieval methodology, as explained below and visualized in Figure 6.1:

1. **Simulated enhancements on the simulated grid ($\hat{\mathbf{Q}}_{\mathbf{sim/sim}}$):** Source rate quantification from simulated enhancements on the simulated grid after atmospheric transport.
2. **Simulated enhancement on GOES' coordinate grid ($\hat{\mathbf{Q}}_{\mathbf{sim/GOES}}$):** Source rate quantification after resampling the simulated enhancements from the simulated coordinate grid to GOES' coordinate grid.
3. **Retrieved enhancement on GOES' coordinate grid ($\hat{\mathbf{Q}}_{\mathbf{ret/GOES}}$):** Source rate quantification after the simulated enhancements are converted to radiances (forward radiative transfer) and the enhancements are retrieved back (inverse radiative transfer).

Quantifying the source rate from retrieved enhancements on the simulated grid $\hat{\mathbf{Q}}_{\mathbf{ret/sim}}$ is not useful since it would exclude the effect of resampling, making it unrepresentative of real-life retrievals. Hence, it is not considered here.

Figure 6.1: Definition of three source rate metrics for OSSE case 1.

6.1.3.2. Case 2: Effect of source rate and airmass on derived source rate

The goal of case 2 is to investigate the effect of different simulated source rates and airmasses (determined by the solar zenith and viewing zenith angles, see Equation 2.2) on derived source rate accuracy is investigated. To this end, source rates are derived from retrieved enhancements of plumes with varying simulated source rates and airmasses on GOES' coordinate grid ($\hat{Q}_{\text{ret,GOES}}$). Since the simulated source rates are known, they can be compared to the derived source rates to assess their effects. All retrieval settings are the same as for case 1 and the source rate is still quantified by summing all enhancements across the scene.

Source rate simulations range between 100 and 500 th^{-1}. Solar zenith angles and viewing zenith angles range between 0° to 60°, resulting in airmasses between 2 and 4. $\gamma_{VZA} = 60°$ has been chosen as the upper limit to stay below GOES' maximum radiance performance requirement of $\gamma_{VZA} \leq 70°$ [102]. This ensures that degradation of the radiance due to low viewing zenith angles does not influence the verification results. In total, fifteen source rates and fifteen airmasses are simulated, resulting in 225 simulations to assess the effects of the simulated source rate and airmass of the derived source rate.

6.1.3.3. Case 3: Effect of non-constant albedo on derived source rate

The goal of case 3 is to investigate the effect of a realistic scene-wide albedo on the accuracy of the derived source rate quantification. 225 plumes are again simulated with varying source rates and airmasses but, unlike case 2, non-enhanced GOES B5 and B6 radiance data is used to model a variable albedo. This albedo can be considered as the canvas upon which the simulated plume is "painted" before the forward radiative transfer model calculates the radiances. The variable albedo affects the synthetic radiances and, thereby, the retrieved enhancements and the plume quantification. This case investigates the magnitude of this effect. Except for the albedo, all retrieval settings are the same as for case 1 and the source rate is still quantified by summing all enhancements across the scene.

6.1.3.4. Case 4: Derived source rate quantifications under realistic conditions

The goal of case 4 is to investigate the accuracy of derived source rate quantifications under realistic retrieval conditions. This means that the albedo is calculated using real GOES data, a different reference day than target day is used and the empirical scaling factors c_{ref} and c_{target} are no longer equal since the albedo's spectral dependence is more significant than the radiance differences between the target and reference days caused by the plume.

Since the target and reference days are different, noise and artefacts will be present in the retrieval. This means that the source rate can no longer be quantified by summing all enhancements across the scene but a binary plume mask must be used to separate the plume pixels from the surrounding scene. Only the enhancements inside the mask are used to quantify the plume's mass and derive the corresponding source rate.

Assessing the derived source rate quantifications requires an uncertainty estimate. Under realistic retrieval conditions, three main parameters influence the calculated IME and, thereby, the derived source rate: the reference day, the plume masking thresholds and the retrieval noise.

Reference day uncertainty

Differences between the reference day and the target day create artefacts in the retrieval, which affects the plume masking and the IME quantification. The reference day uncertainty of the IME is quantified by using an ensemble of three suitable, cloud-free reference days. The retrieval is performed for each reference day and the IME over time is quantified for each. The reference day uncertainty is calculated as the standard deviation across the subsequent IME results at each timestamp.

Plume masking thresholds uncertainty

The plume masking thresholds directly determine the magnitude of the enhancements that are included in the plume mask. Hence, the IME results at each timestamp depend on the selected plume masking threshold. The plume mask threshold uncertainty of the IME is quantified by using an ensemble of four thresholds. The plume is quantified with each of these thresholds, and the plume mask threshold uncertainty is calculated as the standard deviation across the subsequent IME results at each timestamp.

Retrieval noise uncertainty

For any given retrieval, the enhancement concentration $\Delta\Omega$ in each plume pixel can be considered to be the sum of two constituents: 1) a constant "base" retrieved concentration $\Delta\Omega_{\text{base}}$, and 2) a randomly distributed retrieval noise concentration $\Delta\Omega_{\varepsilon}$. Deriving the contribution of the retrieval noise to the IME uncertainty is based on separating the contributions of these two concentrations into IME_{base} and $\text{IME}_{\text{noise}}$. For a plume of N pixels, $\text{IME}_{\text{noise}}$ is derived as follows:

$$
\begin{aligned}
\text{IME} &= m_{CH_4} \sum_{i=1}^{N} (\Delta\Omega A_i) \\
&= m_{CH_4} \sum_{i=1}^{N} (\Delta\Omega_{\text{base}} + \Delta\Omega_{\varepsilon})\, A_i \\
&= m_{CH_4} \sum_{i=1}^{N} (\Delta\Omega_{\text{base}} A_i) + m_{CH_4} \sum_{i=1}^{N} (\Delta\Omega_{\varepsilon} A_i) \\
&= m_{CH_4} \sum_{i=1}^{N} (\Delta\Omega_{\text{base}} A_i) + m_{CH_4} \bar{A} \sum_{i=1}^{N} \Delta\Omega_{\varepsilon} \\
&\equiv \text{IME}_{\text{base}} + \text{IME}_{\text{noise}},
\end{aligned}
\tag{6.1}
$$

where $\bar{A}$ is the mean pixel area of the plume pixels. Since plumes are very small compared to the spatial scales affecting pixel area, this simplification will introduce negligible error. According to Equation 6.1, the contribution of the retrieval noise to the IME depends on the sum of the randomly distributed noise concentrations across all plume pixels. Assuming the noise concentration of each plume pixel is a normally-distributed independent random variable E with zero mean and standard deviation σ, this yields $E_i \sim \mathcal{N}(0, \sigma_{noise_i})$ for i=1, .., N. Using the property that variances sum quadratically, this yields:

$$\sum_{i=1}^{N} \Delta X_{\varepsilon} \sim \mathcal{N}\left(0, \sqrt{\sigma^2_{\text{noise,0}} + ... + \sigma^2_{\text{noise,N}}}\right) = \mathcal{N}\left(0, \sqrt{N\sigma^2_{\text{noise,i}}}\right) = \mathcal{N}\left(0, \sqrt{N}\sigma_{\text{noise,i}}\right) \tag{6.2}$$

This yields an expression for the uncertainty contribution of retrieval noise to the IME:

$$\sigma_{\text{IME,noise}} = m_{CH_4}\bar{A}\sqrt{N}\sigma_{\text{noise}}, \tag{6.3}$$

where σ_{noise} is defined as the standard deviation of the retrieved enhancements outside the plume mask, so as not to bias the retrieval noise with the plume enhancements.

Combining uncertainties

The contributions to the IME uncertainties of the reference day, the plume mask threshold and the retrieval noise are combined by taking the square root of the sum of their variances:

$$\sigma_{\text{IME,total}} = \sqrt{(\sigma_{\text{IME,refday}})^2 + (\sigma_{\text{IME,threshold}})^2 + (\sigma_{\text{IME,noise}})^2} \tag{6.4}$$

Using this approach results in an estimate of the IME uncertainty at each timestamp by considering how the IME results change due to retrieval noise and different input variables. An advantage of this approach is its simplicity. Other uncertainty propagation techniques, such as Monte Carlo simulations, are more computationally expensive and require prior knowledge of the possible/likely magnitudes of input variables to perform a grid search. In this scenario, the magnitudes of input variables, such as the plume mask thresholds, depend on the retrieval, which makes a Monte Carlo simulation impractical. An important downside of this approach is that it assumes that changes in the IME quantification due to the plume mask thresholds and selected reference day are independent since these variables are varied separately instead of simultaneously. This assumption may be weak and would need to be investigated in further detail to confirm or reject.

Source rate quantification

Since the simulated source rate is constant, the derived source rate can be calculated from a linear fit to the quantified IME at each timestamp using a least-squares algorithm. This also allows the IME uncertainties to be used to calculate the derived source rate uncertainties, which is necessary to quantify GOES' quantification accuracy. For an emission event of t timestamps, the least-squares algorithm is defined as [103]:

$$\hat{\mathbf{x}} = \hat{\mathbf{S}}\left(\mathbf{K}^T\mathbf{S}_{\epsilon}^{-1}\mathbf{y}\right) \text{ with } \hat{\mathbf{S}} = \left(\mathbf{K}^T\mathbf{S}_{\epsilon}^{-1}\mathbf{K}\right)^{-1}, \tag{6.5}$$

where $\hat{\mathbf{x}}$ is a 1×1 (constant) derived source rate, $\hat{\mathbf{S}}$ is the 1×1 covariance of the derived source rate, $\mathbf{K}$ is the 1×t time vector, $\mathbf{S}_{\epsilon}$ is the t×t error covariance matrix of the IME and $\mathbf{y}$ is the 1×t IME vector. In practice, the first entry of the IME covariance matrix will always be zero since there is no emitted methane at the first timestamp of the simulation. This causes a derived source rate of 0 th^{-1}. This problem is solved by replacing the uncertainty with the second-smallest uncertainty in the simulation (usually of the second timestamp).

6.1.3.5. Overview of cases

Table 6.2 presents a summary of the four cases in the OSSE with their settings and a brief description. Collectively, these cases aim to demonstrate the correct functioning of the GOES retrieval and plume quantification pipeline.

Table 6.2: List of different OSSE cases for final verification.

Case	Title	OSSE settings			Number of simulation runs	Objective
		Albedo	Airmass	$c_{ref} = c_{tar}$		
1	Assessing the consistency of the radiative transfer models	Constant	Constant	True	1 source rate x 1 airmass = 1 simulation	Verify quantification accuracy for simplified conditions and assesses inherent biases. along various stages of the OSSE.
2	Effect of source rate and airmass on derived source rate	Constant	Variable	True	15 source rates x 15 airmasses = 225 simulations	Quantify the effects of different simulated source rates and airmasses.
3	Effect of non-constant albedo on derived source rate	Realistic	Variable	True	15 source rates x 15 airmasses = 225 simulations	Quantify the effects of realistic albedo (estimated from non-enhanced GOES radiance data).
4	Derived source rate quantifications under realistic conditions	Realistic	Variable	False	20 source rates x 4 airmasses = 80 simulations	Assess the effects of different ref. days and masking thresholds on source rate quantification accuracy

6.2. Probability of Detection

GOES was not originally designed to detect methane plumes. However, previous research has shown that GOES is capable of detecting large plumes above bright backgrounds [42]. One objective of this thesis is to characterize the general methane sensitivity of GOES and assess under which conditions it can be successfully used to detect and quantify methane emissions. To this end, a continuous probability of detection (POD) function will be derived that captures the probability that GOES can detect methane plumes under certain conditions. This curve is essential to understand which plumes can and cannot be detected in the real world and how GOES can be used to help mitigate methane emissions. No POD curve for GOES has been published so this thesis will provide the first generalized characterization of its methane detection capabilities.

6.2.1. Deriving probability of detection functions

The mathematical approach behind deriving a continuous POD function for GOES is based on [25], although the implementation differs. [25] published POD curves for three airplane-mounted detection technologies based on available controlled-release campaign data. Since no controlled-release campaigns exist with large enough emissions for GOES' hypothesized 10-100 th^{-1} detection limit, this thesis relies on simulated methane plumes to create a synthetic POD formulation. [42] This synthetic POD is validated by real-world detections of TROPOMI-detected methane plumes in North America.

A POD function represents the likelihood of a successful detection of a methane plume for a given set of conditions during a single observation. In general, the parameters that affect the detection probability depend on the detection technology. In the case of GOES, a plume's detectability depends on the source rate Q, the wind speed U, which drives plume dispersion, and the signal-to-noise ratio. The signal-to-noise ratio of GOES' retrievals itself depends on the spatial resolution (pixel size) z at a given location and the scene-wide albedo α. Drone- and airplane-mounted detection technologies are also affected by their altitude above the methane enhancements, which affects the intensity of the reflectances through the inverse square law, but this is not the case for GOES due to its geostationary orbit. Another relevant parameter to the probability of detection is the altitude of the plume since plume dispersion is height-dependent [25]. However, since the altitude is undefined for a non-detected plume, this parameter is not considered here.

Using these relevant parameters, a GOES-specific POD function can be derived that depends on $\boldsymbol{x} = [\mathrm{Q}, \mathrm{U}_{10}, \mathrm{z}, \alpha]^T$, where U_{10} is the wind speed at 10 meters altitude. However, unlike airborne detection methods or LEO satellites, GOES' spatial resolution (see Figure 2.14) and potential albedo background will vary significantly per plume location due to its geostationary field of view (FOV).

Hence, instead of deriving a singular POD formulation for the entire range of possible pixel sizes and albedos, separate sub-formulations will be derived that hold for a specific range of pixel sizes and albedos, such that $\boldsymbol{x} = [\mathrm{Q}, \mathrm{U}_{10}]^T$ for a specific combination of location and albedo background. This way, each formulation will be optimized for a specific range of locations in GOES' FOV, rather than trying to cover all pixel sizes and albedos at once.

For each pixel size m, determined by the location, and albedo background n, the POD sub-formulations will be derived by binary regression on a set of simulated plumes under different source rates and wind speeds. The objective of the detection is to model a dependent variable $\mathrm{D}_{\mathrm{m,n}}$ that indicates whether a plume was detected (1) or not detected (0), which follows a Bernoulli distribution with $\mathrm{POD}(\boldsymbol{x})$ as its parameter:

$$\mathrm{D}_{\mathrm{m,n}} \sim \mathrm{Bernoulli}(\mathrm{POD}(\boldsymbol{x})_{m,n}) \tag{6.6}$$

The functions $\mathrm{POD}(\boldsymbol{x})_{m,n}$ are modeled as composites of a predictor function $g(\boldsymbol{x}; \boldsymbol{\phi}_{m,n})$ with variables $\boldsymbol{x}$ and coefficients $\boldsymbol{\phi}_{m,n}$, and a continuous inverse link function $F(g(\boldsymbol{x}; \boldsymbol{\phi}_{m,n}), \boldsymbol{\theta})$ with variables g and coefficients $\boldsymbol{\theta}$:

$$\mathrm{POD}(\boldsymbol{x})_{m,n} \equiv F(g(\boldsymbol{x}; \boldsymbol{\phi}_{m,n}), \boldsymbol{\theta}) \tag{6.7}$$

The purpose of the predictor function is to provide a non-negative output that increases with source rate and decreases with wind speed. The inverse link function maps this output to a continuous probability between 0 and 1 to indicate the probability of detection. The coefficients $\boldsymbol{\phi}_{m,n}$ that parametrize the predictor function are solved by maximum likelihood estimation (MLE). MLE is a commonly used statistical method that estimates a model's parameters based on maximizing a likelihood function such that the model is most probable under some observed data points [104]. In this case, the parameters are the coefficients $\boldsymbol{\phi}_{m,n}$ and the observed data points are the detection results (1 for a successful detection, 0 for a missed detection) of simulated plumes. Solving for $\boldsymbol{\phi}_{m,n}$ is achieved by minimizing the loglikelihood function of the Bernoulli distribution:

$$\ell(\boldsymbol{\phi}_{m,n}, \boldsymbol{\theta}) = \sum_i - \left(D_{i,m,n} \ln F_{i,m,n} + (1 - D_{i,m,n}) \ln (1 - F_{i,m,n}) \right), \tag{6.8}$$

where $F_{i,m,n} = F(g(\boldsymbol{x_i}; \boldsymbol{\phi_{m,n}}), \boldsymbol{\theta})$ for each simulated plume i at location m and background albedo n. The resulting coefficients $\boldsymbol{\phi}_{m,n}$ thus scale the predictor function such that the observed detectability results of the simulated plumes are most probable. The minimization is achieved using a Nelder-Mead optimization algorithm [105]. To prevent over-determination of the minimization problem, the coefficients of the inverse link function $\boldsymbol{\theta}$ are constrained to yield a unit mean and unit variance [25].

For a given probability of detection p, the POD of location m and albedo background n can be inverted to calculate a critical source rate that depends on the wind speed: $\mathrm{Q}_{\mathrm{p,m,n}}(\mathrm{U}_{10}; \mathrm{p}, \mathrm{m}, \mathrm{n})$. This directly states the required source rate at a certain wind speed for a p% probability of detection.

Different candidate predictor and inverse link functions can be considered depending on the elements considered in $\boldsymbol{x}$. Using a linear formulation of the predictor function, such that $g(\boldsymbol{x}) = \boldsymbol{\phi}^T_{\boldsymbol{m,n}} \boldsymbol{x}$, results in a detection probability that tends to zero as the wind speed tends to zero, which implies that an infinitesimally small emitter could be detected at $\mathrm{U}_{10} = 0\ \mathrm{ms}^{-1}$. This is impossible for a real detection system. To avoid this, a candidate predictor function must be non-linear and non-negative (since Q and U_{10} cannot be negative). Candidate inverse link functions that map to between 0 and 1 are cumulative distribution functions (CDF) of any distribution for positive-only values. Examples of these functions are the Fréchet, Burr and lognormal CDFs. [25]

6.2.2. Location selection

To assess the effect of the plume location on the POD, three locations with a different mean pixel area will be investigated. These locations are shown by the three markers in Figure 6.2. The coordinates of the locations and their mean pixel area is given in Table 6.3. Each location is sampled from a pixel area range in CONUS and is selected to be near the boundary to an adjacent range to represent the coarsest pixel area that locations in that range can attain.

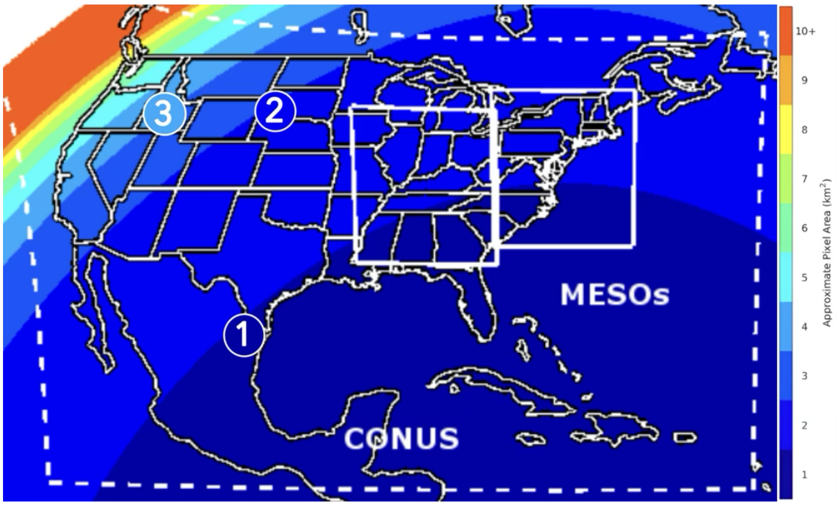

Figure 6.2: Locations of three selected POD locations and their B5 pixel areas. Adapted from [90].

Table 6.3: Characteristics of the three POD locations.

#	Location	Coordinates	Mean pixel area	Difference wrt Mexico
1	Coahuila, Mexico	28°N, 101°W	6.0 km^2	-
2	South Dakota, US	43°N, 101°W	8.3 km^2	+38%
3	Idaho, US	43°N, 116°W	11.0 km^2	+83%

Figure 6.3 shows the pixel size distribution throughout the scene of interest for the three POD locations. The scenes become increasingly tilted as their location shifts further to the northwest. This is due to GOES' geostationary perspective of these locations and the curvature of the Earth. The pixel size is always the smallest in the lower right corner of the scene since this is closest to GOES' nadir point and hence is observed at the finest spatial resolution.

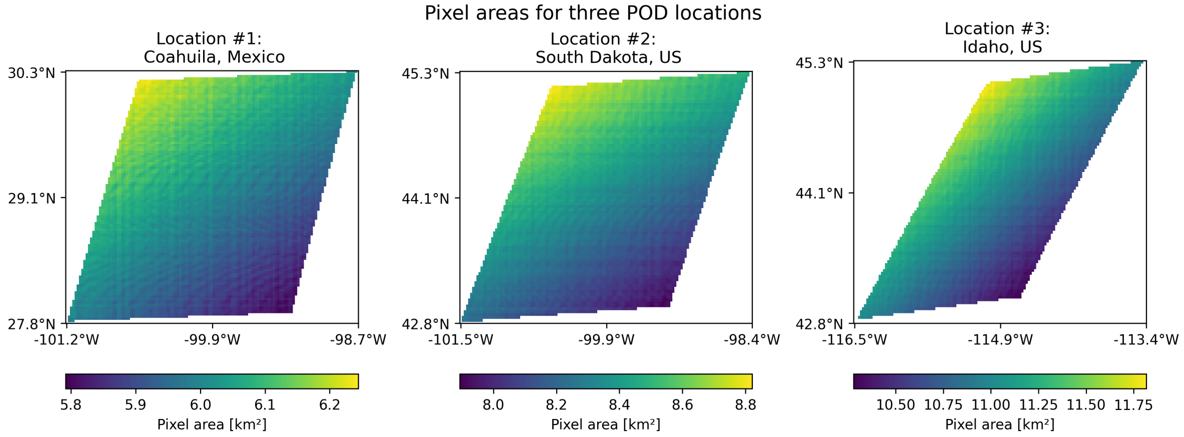

Figure 6.3: Pixel area distribution for three different POD locations in CONUS.

For simplicity, all methane plume simulations are performed on the same location (coordinate grid) in Coahuila, Mexico (location #1). For the other two locations, the simulation grid is shifted to the desired location by adding offsets to the latitude and longitude values. When moving the simulation grid to the North in the Northern hemisphere, the spacing between the longitude values decreases. This would compress the shape of the plume in the simulation so this effect must be nullified by applying the inverse of the compression. This way, the shape of the plume is retained, even after moving the simulation grid to a different location. Latitude lines are not compressed when moving North since their spacing remains constant. After the simulation grid has been shifted to the desired location, it is resampled to the local GOES coordinate grid (see Figure 4.2).

6.2.3. Albedo background selection

The number of photons that are absorbed or reflected by the Earth's surface determines the spectral albedo. A higher albedo means more photons are reflected, resulting in a higher signal-to-noise ratio. Hence, the albedo is an important parameter that will affect GOES' PODs. To investigate this effect, three representative albedo types were selected from CONUS scenes: desert, farmland and forest. These albedo types are shown in Figure 6.4 and further details on the location, mean albedo and respective differences are given in Table 6.4.

Combined across categories, desert, farmland and forest albedo types constituted 88% of total US surface area in 2017 [106]. Most US states with large-scale O&G industries, such as Texas, New Mexico, North Dakota and Colorado, largely fall in one of these three categories so these albedos are representative of most real-life methane plume backgrounds. Urban areas are not considered here due to their small overall size and low probability of methane leaks caused by the absence of large-scale O&G infrastructure. Wetlands are also not considered here since water strongly absorbs SWIR radiation, complicating methane plume retrieval.

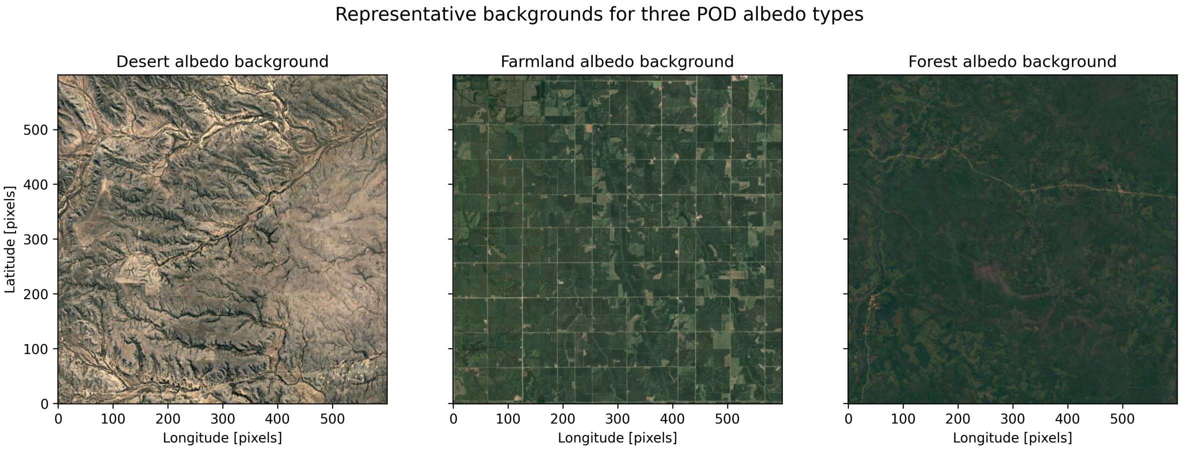

Figure 6.4: Approximate background images of three selected POD albedo types. Longitudes and latitudes are given in pixels because the actual background size depends on POD location. Imagery from Google, ©2024 TerraMetrics, ©2024 Airbus and Maxar Technologies.

Table 6.4: Characteristics of the three POD albedo types.

#	Albedo type	Approx. location	Mean albedo across space and time [-]	Difference wrt desert
1	Desert (high)	Coahuila, Mexico	B5: 0.25, B6: 0.16	-
2	Farmland (medium)	Iowa, US	B5: 0.22, B6: 0.12	B5: -12%, B6: -25%
3	Forest (low)	Mississippi, US	B5: 0.13, B6: 0.07	B5: -48%, B6: -56%

Albedo is depends on wavelength so radiances will vary per spectral band. This is shown in Figure 6.5 for the three albedo scenes. In total, two hours of albedo scenes are cropped from cloud-free GOES B5 and B6 data to match the two-hour emission simulation. The selected dates of GOES data vary per albedo type since cloud conditions vary per location but all scenes are taken at the same time of day.

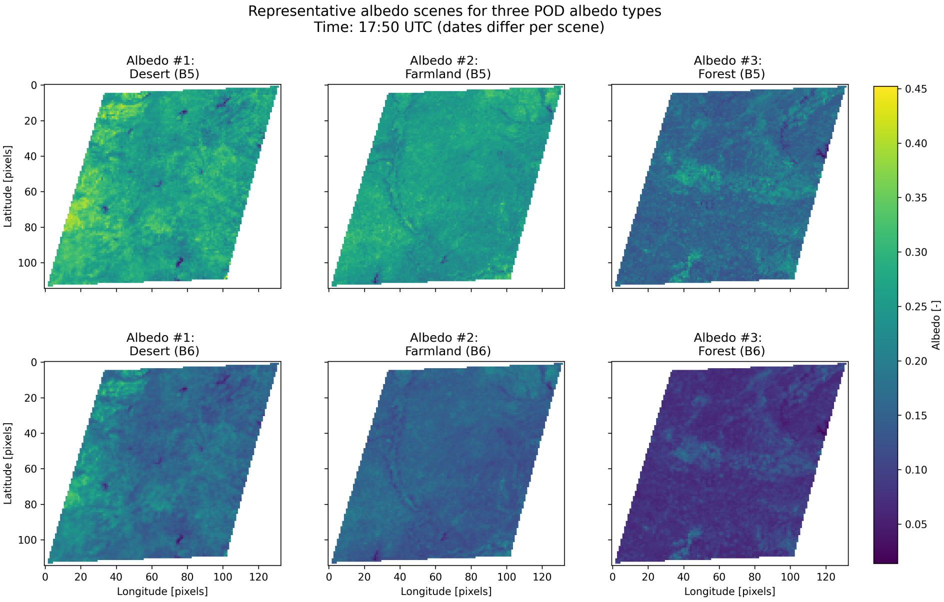

Figure 6.5: Representative albedo values for three different POD albedo types for B5 and B6 spectral bands. Values are calculated from real-life GOES B5 and B6 data. Longitudes and latitudes are given in pixels because actual size depends on POD location.

Part III

Results

7

Verification by Observation System Simulation Experiment

This chapter presents the OSSE results for the four different cases that were described in Section 6.1.3.

7.1. Case 1: Assessing the consistency of the radiative transfer models

The goal of the first case is to verify the consistency of the radiative transfer models and verify the accuracy of the quantification if all circumstances are idealized and simplified, thereby defining the benchmark for the accuracy of the quantification algorithm. The retrieval settings are summarized in Table 6.2. Figure 7.1 shows the simulated methane plume at a simulated source rate of 500 $\mathrm{t\,h^{-1}}$. The inverse radiative transfer model is applied to this plume, resulting in GOES' B5 and B6 synthetic radiances. These radiances are then used to retrieve back the enhancements. These intermediate results are shown in Figure 7.2a–f.

Figure 7.2g compares the simulated and retrieved $\Delta\Omega$ values for all scene pixels. The gray points fall exactly on the parity line, indicating that the simulated enhancements are retrieved without error (bias is zero) under these simplified conditions.

The results of the three IME and derived source rate quantifications, as defined in Figure 6.1, are shown in Figure 7.3. The biases for the IME and derived source rates (reported in the top and bottom plots, respectively) show only a small deviation (always less than 1%) from the simulated source rate for all three results. This is an expected result due to the simplified conditions. Importantly, the bias for $\hat{\mathrm{Q}}_{\mathrm{sim,sim}}$ is non-zero, as shown by the difference between the purple and orange lines in the bottom plot. This means that the true simulated source rate deviates from HYSPLIT's set source rate. The reasons for this error are the numerical rounding errors and interpolation errors, which arise when HYSPLIT regrids the enhancements to the user-defined spatial resolution (see Table 6.1). Since HYSPLIT is used is used for all OSSE cases, the 0.7±0.0% error will be the smallest possible error.

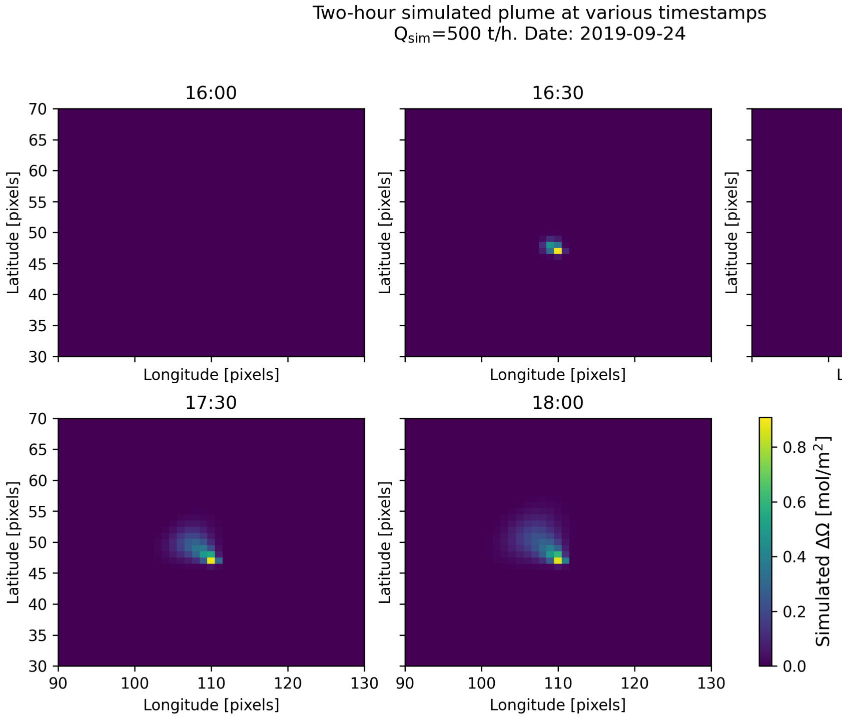

Figure 7.1: Two-hour simulated methane plume at four different timestamps. Simulation between 16:00-18:00 UTC with a 500 th^{-1} source rate.

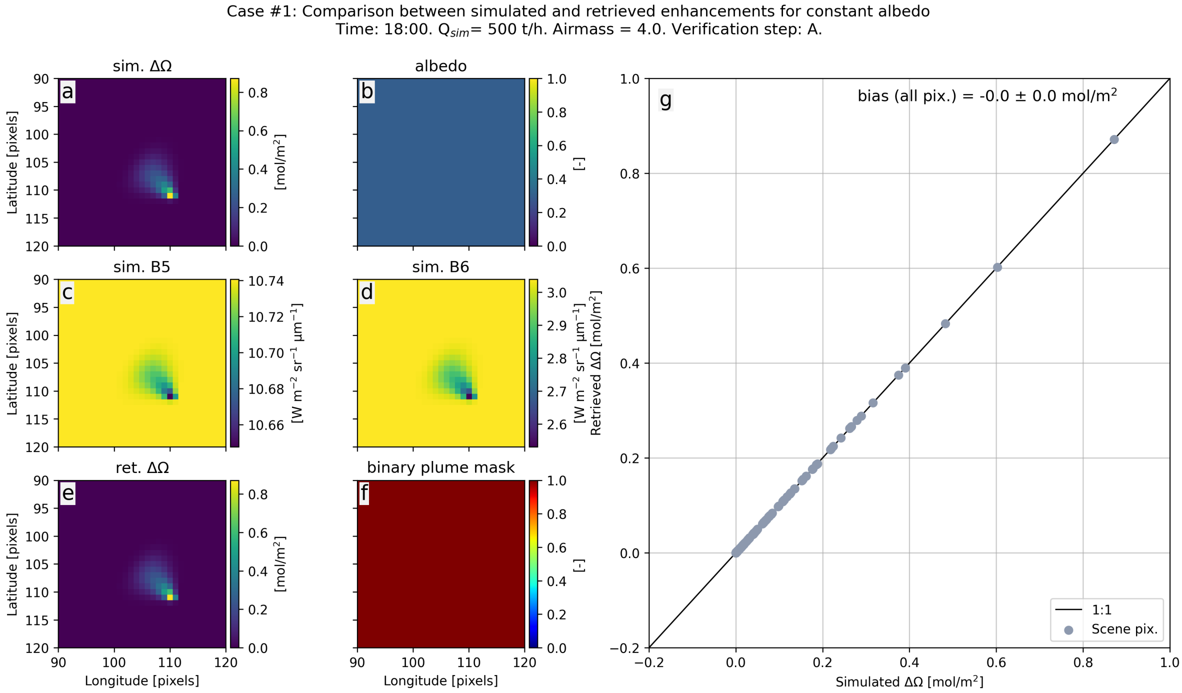

Figure 7.2: Simulated plume and radiances for constant albedo with comparison between simulated and retrieved enhancements. Plume shown at the end of the simulation. (**a**) shows resampled simulated methane concentrations. (**b**) is the scene's albedo map, which is constant (0.3). (**c**) and (**d**) are the B5 and B6 radiances that result from the forward radiative transfer step. (**e**) shows the retrieved enhancements after the inverse radiative transfer step. (**f**) is the scene's binary plume mask. No noise or artefacts are present in the retrieval so the plume mask is unity across the scene. (**g**) is a parity plot with retrieved against simulated enhancements as part of verification step A. The black line is the parity line and each marker represents one scene pixel. The bias of all scene pixels is reported as the mean and standard deviation of the difference between the simulated and retrieved enhancements. Spatial dimensions are in pixels.

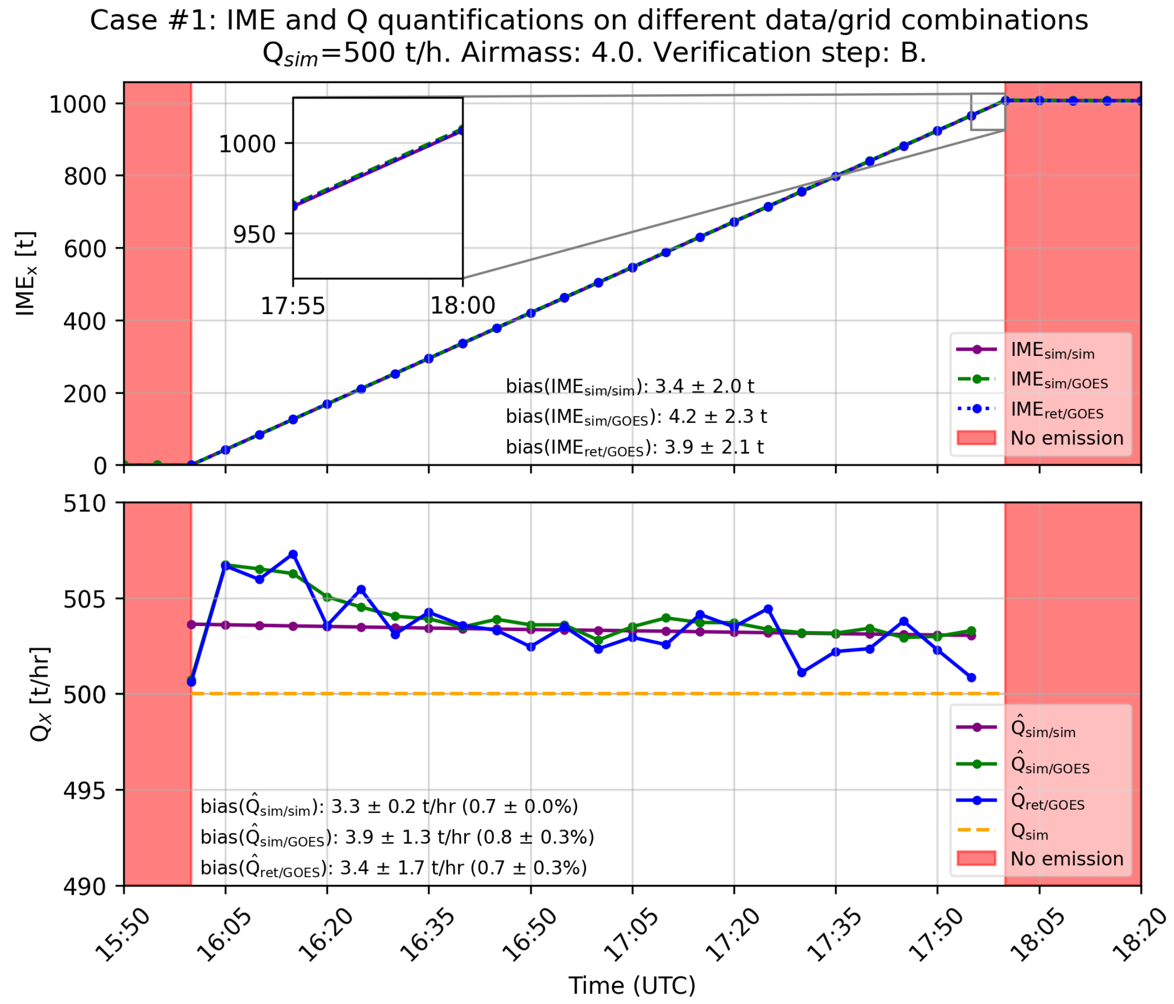

Figure 7.3: IME and derived source rate quantifications on different data/grid combinations. The top plot shows the quantifications of IME over time for the three different data/grid combinations. The red shaded areas indicate no emission. The top inset emphasizes the similarity between the three combinations for the final five minutes of the simulation. The bottom plot shows the derived source rate quantifications over time and the constant simulated source rate as part of verification step B. Biases are also expressed as percentages of the simulated source rate.

7.2. Case 2: Effect of source rate air airmass on derived source rates

Figure 7.4 shows the source rate quantifications obtained from retrieved enhancements after resampling ($\hat{Q}_{\mathrm{ret/goes}}$) for an ensemble of 225 simulations with different source rates and airmasses. All quantifications for different airmasses fall almost on the parity line. The bias is the same as for OSSE case 1 (+0.7%) because the retrieval conditions are the same. This shows that the source rate and airmass do not affect the derived source rate quantification under these retrieval conditions.

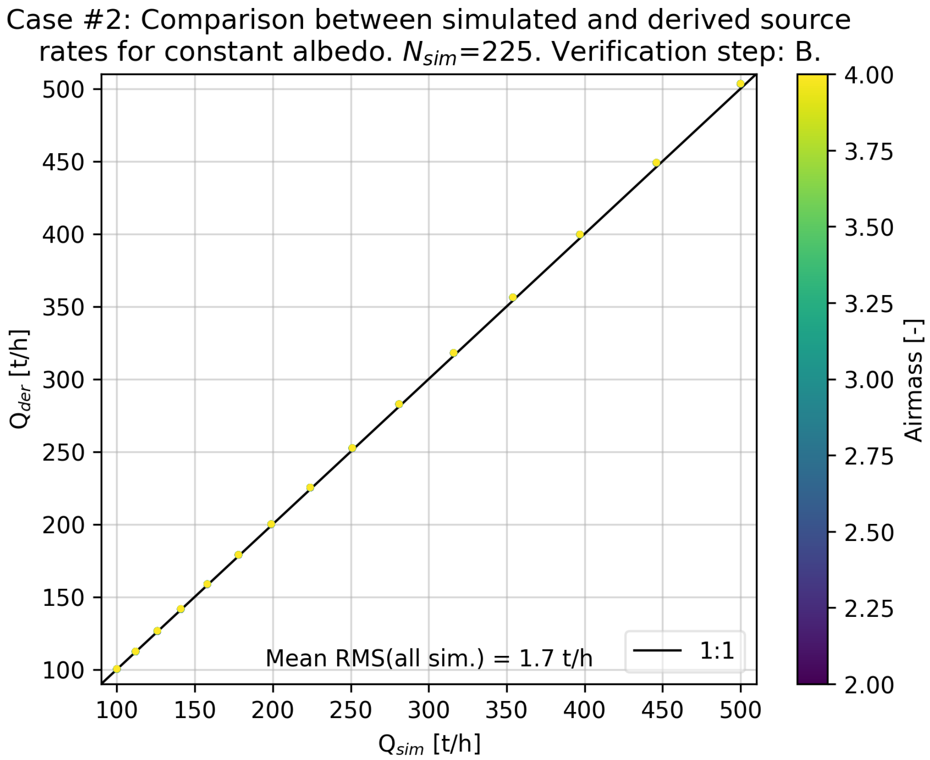

Figure 7.4: Source rate quantifications of 225 simulations with different simulated source rates and airmasses. The black line shows the 1:1 line and the insets show the source rates at the minimum and maximum simulated source rates.

7.3. Case 3: Effect of realistic albedo on derived source rates

The goal of the third case is to investigate the effects of a realistic albedo across the scene. Figure 7.5 shows the comparison between the simulated and retrieved enhancements when a realistic albedo is used. The albedo was calculated from non-enhanced GOES data at the simulation location. The parity plot shows that the retrieved enhancements slightly exceed the simulated enhancements, especially for pixels with high enhancements. The reason for the differences is an interplay between the HYSPLIT error of case 1 and an inherent error in the MBSP retrieval method for integrated spectral bands [62].

To investigate the effect of the realistic albedo, the same ensemble as case 2 was used with the albedo scene from Figure 7.5. The source rate quantification results are shown in Figure 7.6. It shows that the derived source rates have a larger error than in case 2, as caused by the realistic albedo. The largest error is 4.8% and occurs at the highest simulated source rate. This is as expected because retrieved enhancements scale linearly with source rate.

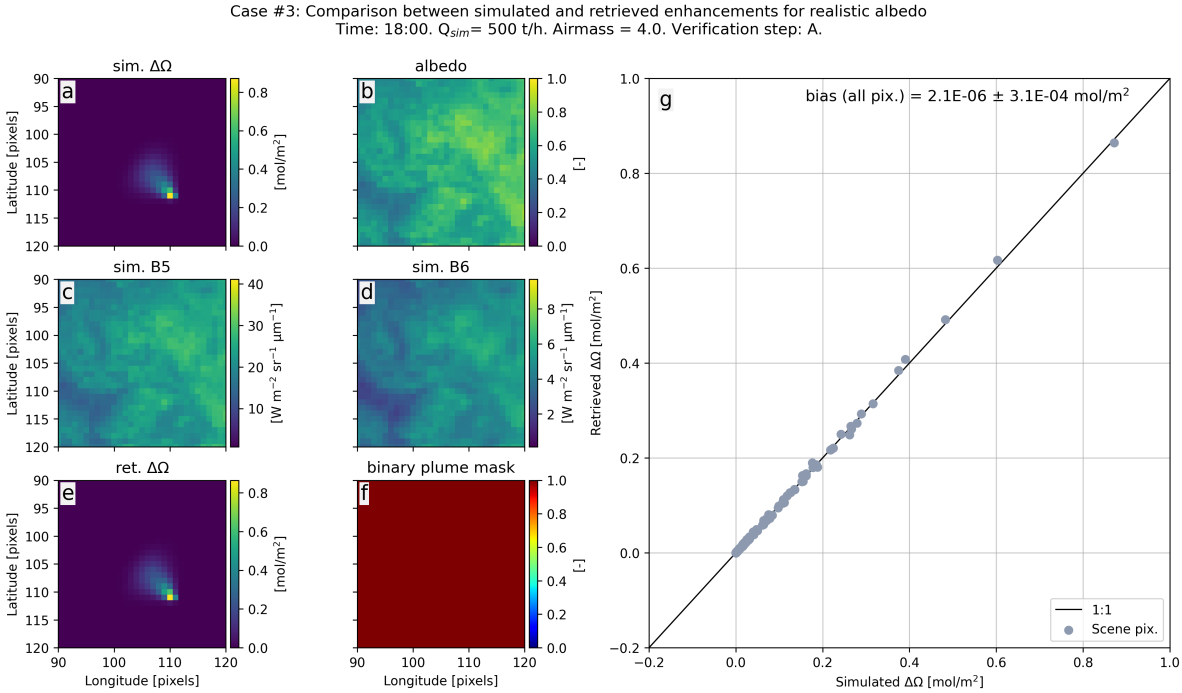

Figure 7.5: Simulated plume and radiances for realistic albedo with comparison between simulated and retrieved enhancements. (**b**) shows the realistic albedo obtained from non-enhanced radiance data. (**c**) and (**d**) show the resulting synthetic radiances.

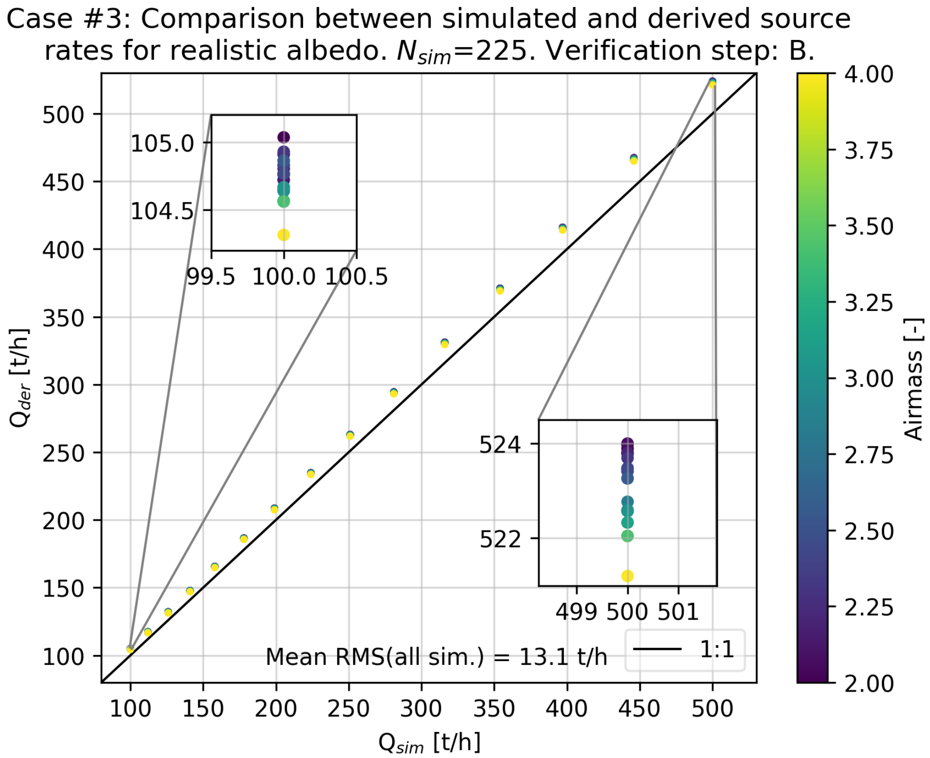

Figure 7.6: Source rate quantifications of 225 simulations with realistic albedos. The albedo is estimated from non-enhanced GOES radiance data. The black line shows the 1:1 line and the inset shows the source rates at the minimum simulated source rates.

7.4. Case 4: Derived source rate quantifications under realistic conditions.

The goal of case 4 is to quantify the accuracy of the IME and source rate simulations for realistic retrieval conditions. Most importantly, a different reference day than the target day is now selected for the first time. This introduces artefacts and noise in the retrieval, necessitating a plume mask to separate the plume from the background before quantification.

Figure 7.7 shows the retrieval results for this realistic scenario. Figure 7.7f shows the binary plume mask based on a lower mask threshold of 75th percentile and an upper mask threshold of 85th percentile. These percentiles are a result of a sensitivity analysis on the masking thresholds and were found to accurately mask the plume in the retrieved enhancements. The parity plot (Figure 7.7g) shows that non-enhanced simulation pixels are not retrieved with zero enhancements due to retrieval noise and that the plume pixels (shown in red) approximately follow the 1:1 line. This is an important result because it means that the pixels in the plume mask can be used to quantify the IME and the source rate, which would not have been the case if those pixels had large errors. To better understand the vertical line of gray scene pixels in Figure 7.7g, Figure 7.8 plots the distribution of the mean retrieved enhancements of the non-enhanced plume pixels. It shows that the mean is close to zero and that the spread (standard deviation) is small. This spread is due to the retrieval noise. It is an important result that the spread is small because it means the pixels with zero input enhancements are retrieved as pixels with (almost) zero enhancements.

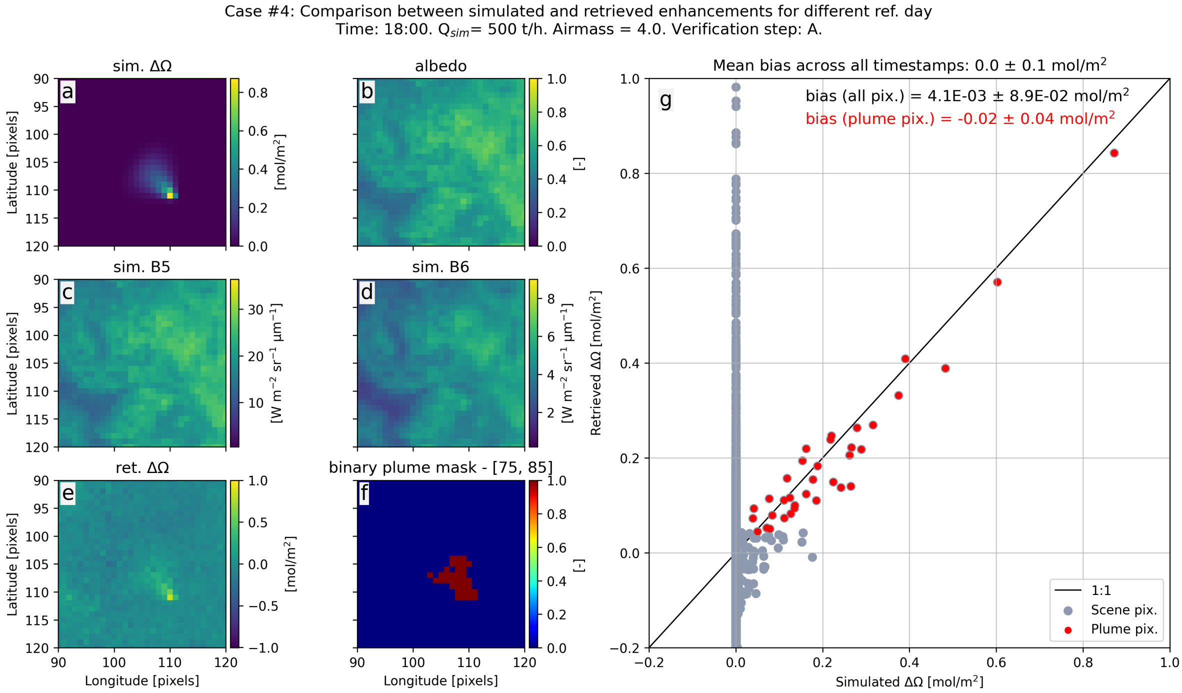

Figure 7.7: Simulated plume and radiances for realistic retrieval conditions with comparison between simulated and retrieved plume pixel enhancements. (**f**) shows the binary plume mask with a lower mask threshold of 75th percentile and the upper mask threshold of 85th percentile. (**g**) shows the distribution of simulated and retrieved enhancements for all scene pixels (gray) and plume pixels (red). The biases for both types are annotated as the mean and standard deviation of the differences between the simulated and retrieved enhancements. The mean bias across all timestamps is given in the subplot title.

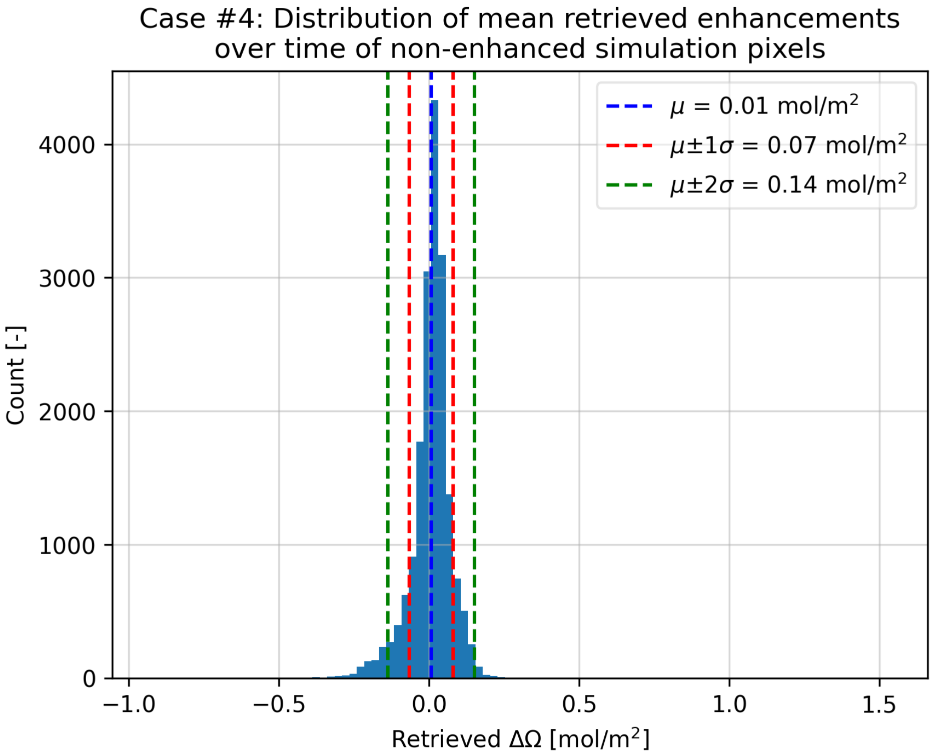

Figure 7.8: Distribution of time-averaged retrieved enhancement of non-enhanced simulation pixels for the case 4 simulation. The non-enhanced simulation pixels also constitute the vertical line of gray markers in Figure 7.7. The distribution is almost centered around 0, indicating the non-enhanced simulation pixels are also retrieved with zero enhancements. The standard deviation is also small, showing that 95% of enhancements are within 0.14 molm^{-2} of the mean.

To perform the IME uncertainty quantification, the retrieval is repeated three times with different reference days. To select suitable, cloud-free reference days, GOES' cloud data is used to plot the cloud fractions at the simulation area for possible reference days around the leak date. These results are shown in Figure 7.9. The best reference days are the ones with the lowest (whitest) cloud fractions during the whole simulation event. The leak date is only used for meteorological input data and does not influence the retrieval. The target date is created by selecting a date for an albedo scene to which the plume simulation is added to represent an emission above a realistic albedo background. 2019-10-19 is selected as the target date, while 2019-10-18, 2019-10-20 and 2019-10-21 are selected as reference days due to their proximity to the target day (small differences in albedo) and minimal cloud cover.

Repeating the retrieval for different reference days and the masking with different masking thresholds, and adding the uncertainty due to the retrieval noise, yields the total IME uncertainties per timestamp. Applying a linear fit (Equation 6.5) to the IME yields the derived source rate and its uncertainty, as shown in Figure 7.10. It shows that the derived source rate quantification results are within 1-sigma uncertainties because the error bars always include the simulated source rate.

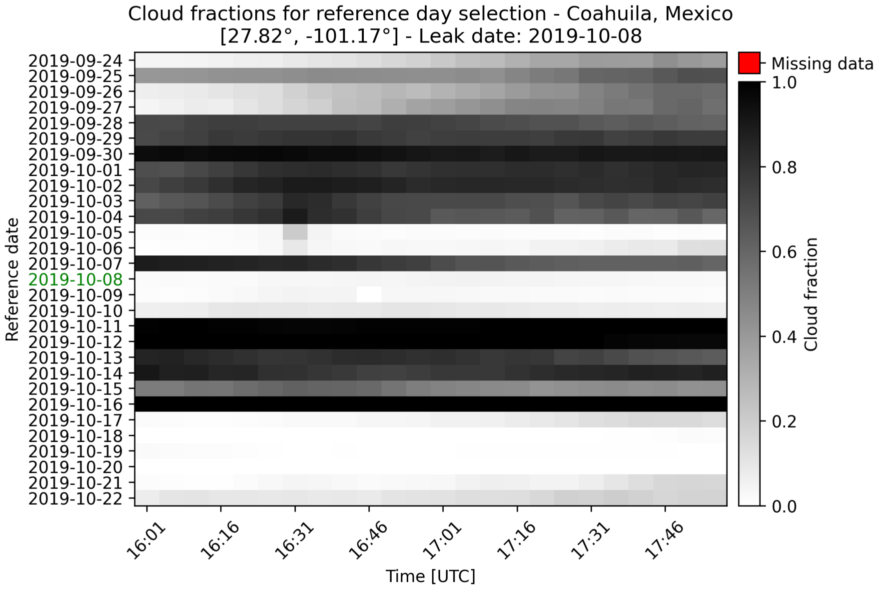

Figure 7.9: Cloud cover fractions at the simulated location on dates near the leak date to select suitable reference days. Cloud cover fractions are quantified using GOES' cloud data product. Four weeks of possible reference days are investigated around the simulated leak date (indicated in green on the vertical axis). Low cloud fractions indicate near-cloud-free conditions, which is essential for the selected reference day. High cloud fractions indicate overcast conditions, which is undesirable for the reference day.

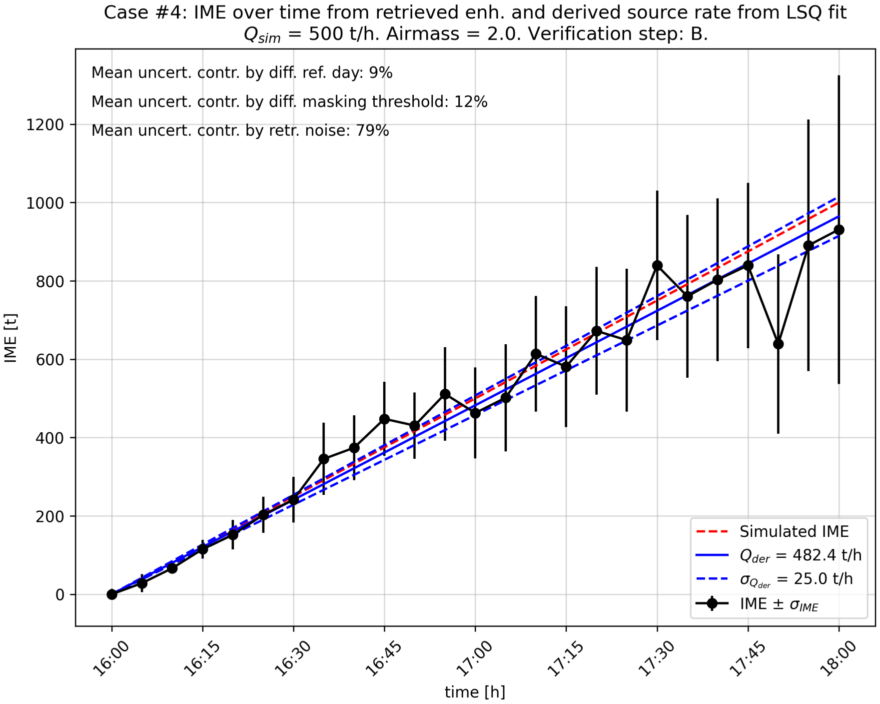

Figure 7.10: Quantification results of the IME over time, its uncertainties, the derived source rate and its uncertainties for one simulated plume. The simulated IME (red dashed line) is calculated by multiplying the simulated source rate with time. The derived source rate (blue line) results from a least-squares fit to the IME and its uncertainties. Its one-sigma uncertainties (blue dashed lines) include the simulated IME line. The uncertainties in the IME are calculated from an ensemble of different reference days and plume masking thresholds, to which the retrieval noise contribution is added. The mean contributions of these three parameters to the IME uncertainty over time is reported as a percentage.

Repeating this process for 80 different plumes with varying source rates and airmasses yields the total uncertainties in the derived source rates for varying conditions. The uncertainties for the airmasses 2.0 and 2.3 (for example, γ_{SZA}=γ_{VZA}=30°) are small enough to include the 1:1 line in the 1-sigma range. The errors increase for larger airmasses but remain small. This confirms GOES' quantification accuracy for different source rates and airmasses.

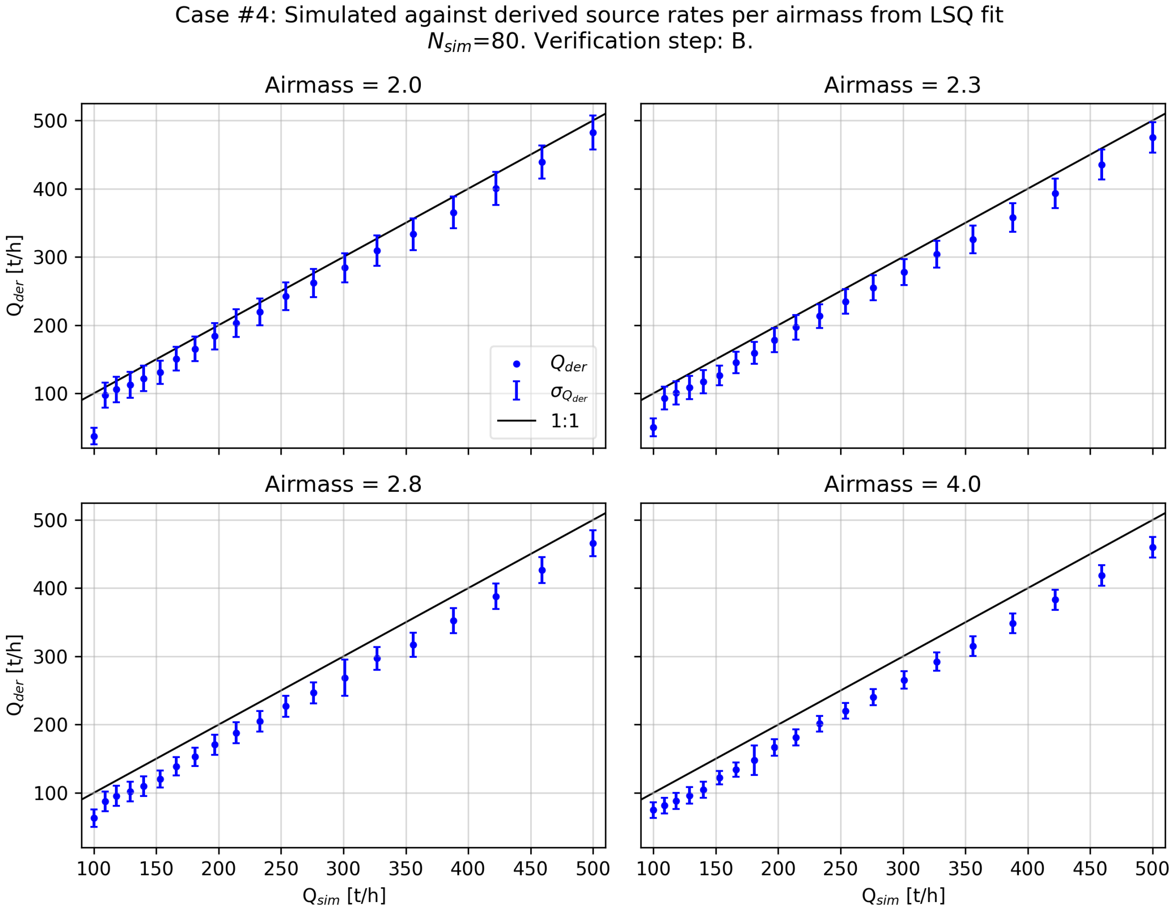

Figure 7.11: Comparison between simulated and derived source rates per airmass for twenty different source rates. The 1:1 line falls within the 1-sigma uncertainty for the airmasses 2.0 and 2.3, but the errors increase slightly for higher airmasses.

8

Probability of detection

This chapter presents the results of the probability of detection functions for the nine combinations of pixel sizes and albedo scenes. Section 8.1 describes the derivation of the synthetic PODs using simulated methane plumes and Section 8.2 describes the validation of the synthetic PODs.

8.1. Synthetic POD

The variables that influence the detection probability are source rate, wind speed, location (which affects pixel size) and albedo. Since the possible range of pixel sizes and albedos is large in the CONUS, the synthetic POD has been split up into nine cases for three pixel sizes and three albedos. For each of these cases, methane plumes were simulated at six meteorological conditions and twenty source rates. This results in 1080 plume simulations to derive the nine POD functions. The forward radiative transfer model is applied to each of these plumes and they are retrieved under realistic conditions (same as OSSE case 4, see Table 6.2).

8.1.1. Simulated methane plumes

Methane plumes are simulated with six different meteorological conditions with spatiotemporal mean wind speeds that vary from 1.8 to 6.8 ms^{-1} (6.5 - 24.5 kmh^{-1}, 2-4 on Beaufort's wind scale). This represents a realistic range of possible wind speeds. The twenty selected source rates range between 1 and 2000 th^{-1} and are selected to cover a wide range of possible source rates. The lower limit was chosen below GOES' estimated detection limit of 10 th^{-1} to assess whether those source rates are indeed too small to be detected [1]. The upper limit was chosen as an exceedingly strong and rare emission compared to TROPOMI source rate estimates between 2018 and 2023 [65]. GOES' low methane sensitivity means it generally can detect only large emission events, making these high source rates interesting for the POD curves.

Figure 8.1 shows the resulting plumes at each meteorological condition with a source rate of 2000 th^{-1} at the end of the two-hour simulation. For the simulations with wind speeds 5.0 and 6.8 ms^{-1}, low concentrations of methane outside of the main plume are observed due to different wind directions at different altitudes in the input wind data. These plumes emphasize the large variability in possible enhancements, shapes and lengths for different meteorological conditions, which may affect the POD. The spatiotemporal mean wind speeds are used to characterize and easily compare the six meteorological conditions. However, this classification is not fully representative of the complex behavior of the full three-dimensional wind field, which is difficult to characterize. Other differences between the meteorological conditions, such as time dependence, wind vorticity, wind gradients and air pressure, may affect the POD but their influence is not considered here. An improvement that could be considered in future work is to utilize more properties of the wind field for comparison, such as the standard deviation of the wind speed, the atmospheric vorticity or the wind gradient. This would add an additional dimension to the POD formulations and further curate them to specific environmental conditions. For instance, if three classifications of wind field vorticity magnitude were added alongside the pixel sizes and albedo backgrounds, 27 POD formulations can be calculated as a function of Q and U_{10}.

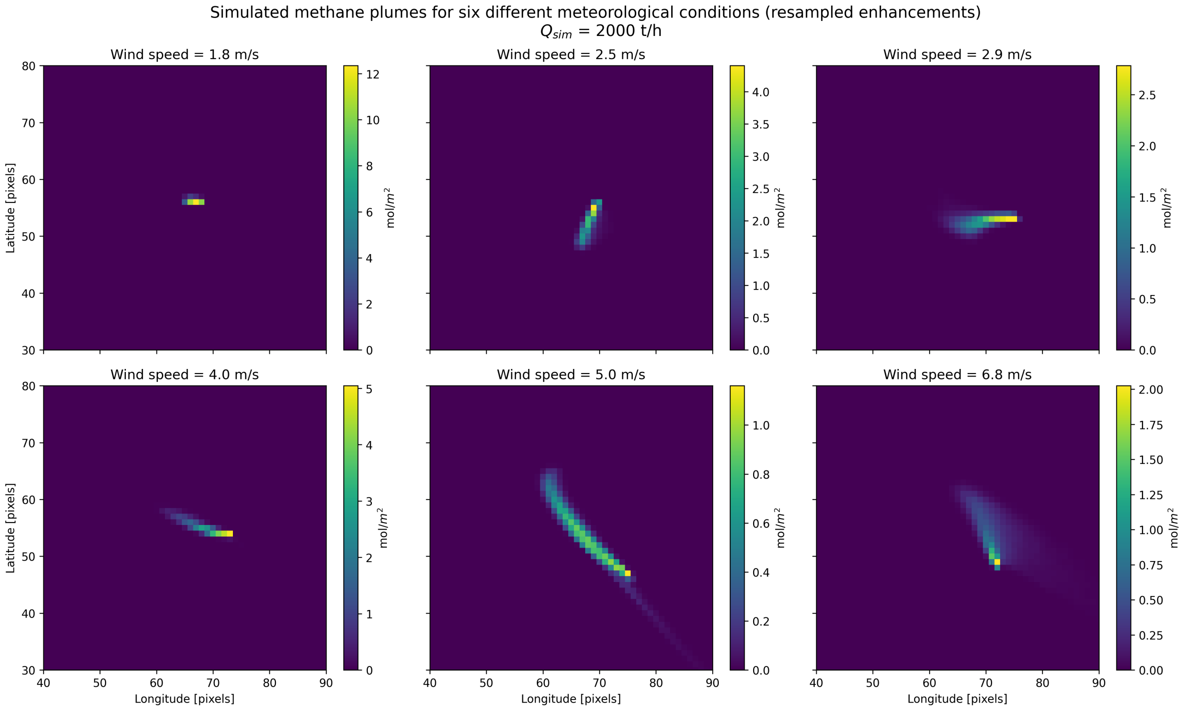

Figure 8.1: Set of simulated methane plumes for six different meteorological conditions. Meteorological conditions are classified by the spatiotemporal mean of the wind speed. Plumes at the end of the two-hour simulation at 2000 th^{-1}. The plume dispersion depends on the wind speed, resulting in plumes of different sizes. HYSPLIT simulates the plume at different height levels, which are summed vertically to create the methane column enhancements that GOES observes. Variable wind speed and direction at different altitudes may result in non-aligned enhancements. Meteorological input data is from ERA5.

8.1.2. Plume detectability metrics

The IME and source rate are derived from the retrieved enhancements of each simulated plume. Based on these quantifications, a set of empirically derived plume detectability metrics is devised. The goal of these metrics is to create a first attempt at automatically distinguishing successful detections from missed detections to determine a plume's binary detectability result. The detectability metrics provide the binary detection success (1/0) for each plume i at location m and albedo n $D_{i,m,n}$ (see Equation 6.6). Automated detection results can provide a fast and scalable approach to detecting methane plumes in GOES data without relying on reference detections from other satellite instruments and are crucial to unlocking GOES' full potential in methane plume detections. Another method to determine detection results is by visual inspection but this approach lacks the speed and scalability of the automated approach, and hence is not suitable for finding plumes in GOES data on a large scale.

The four plume detectability metrics are:

1. **Minimum number of non-zero plume masks:** The ensemble of reference days (3) and masking thresholds (5) contains fifteen different plume masks for each simulated plume. A reference day is considered valid by this metric if it has at least one non-zero plume mask at the simulation's final timestamp. Hence, the minimum number of non-zero plume masks ranges between 0 and 3. At least one valid reference day is required for a successful detection.

2. **Measure of the fit of the derived source rate to the quantified IME:** This metric is calculated by summing the differences between the quantified IME and the derived source rate multiplied by time at each timestamp, and dividing by the derived source rate. This yields a normalized measure of the fit of the derived source rate to the quantified IME. After analyzing many IME and derived source rate quantifications for different pixel size and albedo combinations and comparing the fit metrics to the retrieved enhancements, an empirically-derived threshold of 25 (unit is hour, but not relevant for the discussion) was established, below which detections are successful (1) and above which detections are missed (0).

3. **Measure of the fit of the simulated source rate to the quantified IME:** This metric is similar to the second, but the sum of the differences is normalized by the simulated source rate instead of the derived source rate. This yields a normalized measure of the fit of the simulated source rate to the quantified IME. The same threshold of 25 is used to distinguish detections from non-detections.

4. **Upper threshold on the derived source rate error:** Retrieval artefacts can cause significant errors in the plume mask, which leads to large errors in the quantified IME and large uncertainties. In these cases, the error of the derived source rate from the LSQ fit may exceed 100%. Cases that exceed 100% error are automatically considered missed detections.

Metrics 3 and 4 were defined by exploring the quantification results for different meteorological conditions, pixel sizes, albedos and simulated source rates. Their threshold was selected by comparing quantifications of visually inspected detections to missed detections. If the IME and derived source rate quantifications satisfy all of four metrics, the plume is considered successfully detected. Otherwise, the plume is considered a missed detection.

Figure 8.2 shows the IME and derived source rate quantifications for retrieved enhancements with a small pixel size and medium albedo at meteorological conditions with a spatiotemporal mean wind speed of 5.0 ms^{-1}. Each plot shows a different simulated source rate and the four detectability metrics are indicated for each quantification.

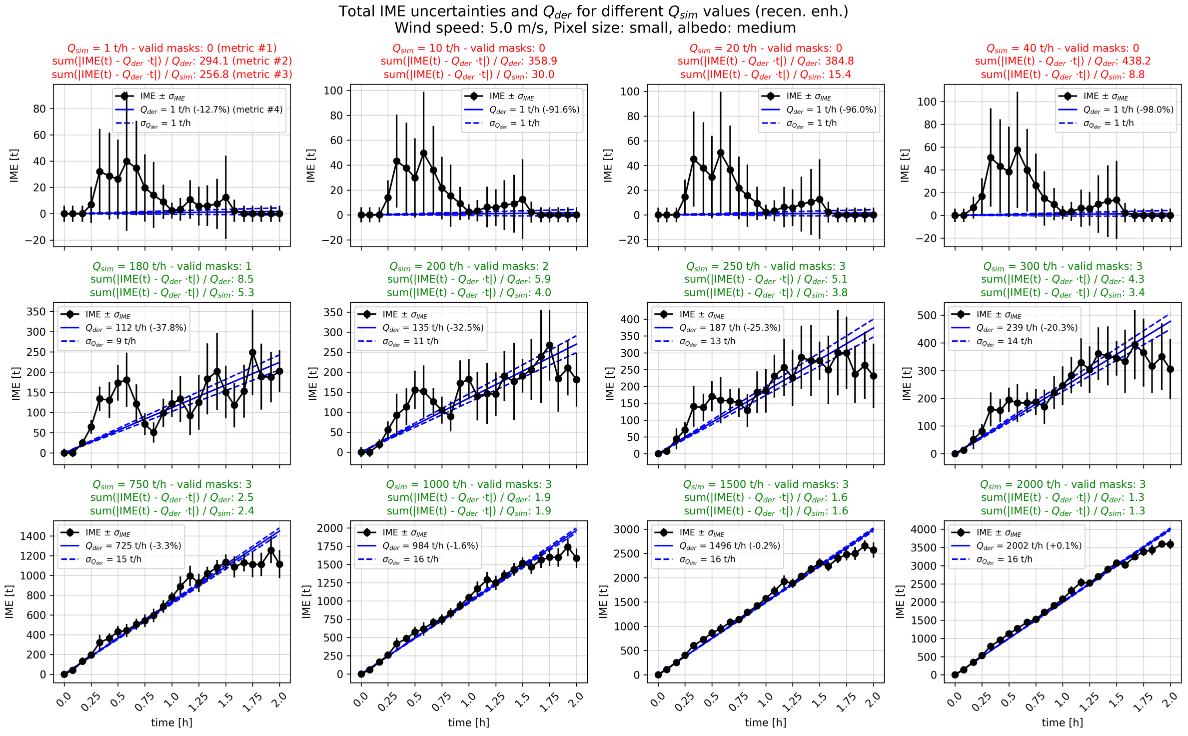

Figure 8.2: IME and derived source rate quantifications for a subset of the simulated source rates, including the four empirically derived detectability metrics. As indicated for $\mathrm{Q_{sim}}$=1 th^{-1}, they are given in the subplots' titles (metrics 1, 2 and 3) and legends (metric 4). A red title color indicates a missed detection (at least one of the four metrics is exceeded), and a green title color indicates a successful detection (all four metrics are satisfied).

The IME points reported in Figure 8.2 are the mean across the ensemble of different reference days and plume masking thresholds. They show that the source rate quantification accuracy increases with increasing simulated source rate. This is expected since higher source rates result in higher enhancements. For lower source rates ($<$100 th^{-1}), the IME quantifications are much less accurate. The large deviations are caused by retrieval artefacts and noise pixels inside the plume mask. The plume masking is particularly difficult for low source rates since the plume enhancements are only marginally above the noise level. Visual inspection of retrieved enhancements confirms the presence of retrieval artefacts for all three albedos. This emphasizes the importance of cloud-free reference days as close as possible to the target day. The presence of waterbodies in the scene also results in artefacts so retrieval conditions are optimal for homogeneous and high albedos.

The automated detection successes based on the detectability metrics are shown on the left sides of Figure 8.3 and Figure 8.4 for the small pixel size and medium albedo and the medium pixel size and bright albedo, respectively. Figure 8.3 shows that detectability success increases with increasing source rate for all meteorological conditions classified by their spatiotemporal mean wind speed and that higher wind speeds require higher source rates for a successful detection. This is expected since higher wind speeds increase plume dissipation, making it more difficult to mask these plumes in the retrieved enhancements. However, there are also outliers from this relationship as shown by Q_{sim}=160 th^{-1} at 4.0 ms^{-1} (indicated by the red square). It is not a detected plume even though its neighboring source rates (140 & 180 th^{-1}) are detected. Visual inspection of the retrieved and recentered enhancements confirms that a plume is visible in this case. Figure 8.4 shows that the performance of the metrics depends strongly on the selected pixel size and albedo since they influence the noise levels and artefacts in the retrieval. No relationship between the detection success and meteorological conditions or simulated source rates is visible here. This demonstrates the plume detectability metrics can incorrectly assess the detectability of a plume.

To improve the detectability results, all retrieved enhancements were inspected and their detectability success was assessed manually. These manually-determined detectability results are shown on the right sides of Figure 8.3 and Figure 8.4. The manually-determined results show a clear trend between the detection success and meteorological conditions or simulated source rates in both figures. In Figure 8.3, the manual results show a strong similarity to the automated results, indicating that the automated metrics perform well in this case. However, in Figure 8.4, large differences between the automated and manual results are visible, indicating that the automated metrics cannot be used in the medium:bright case.

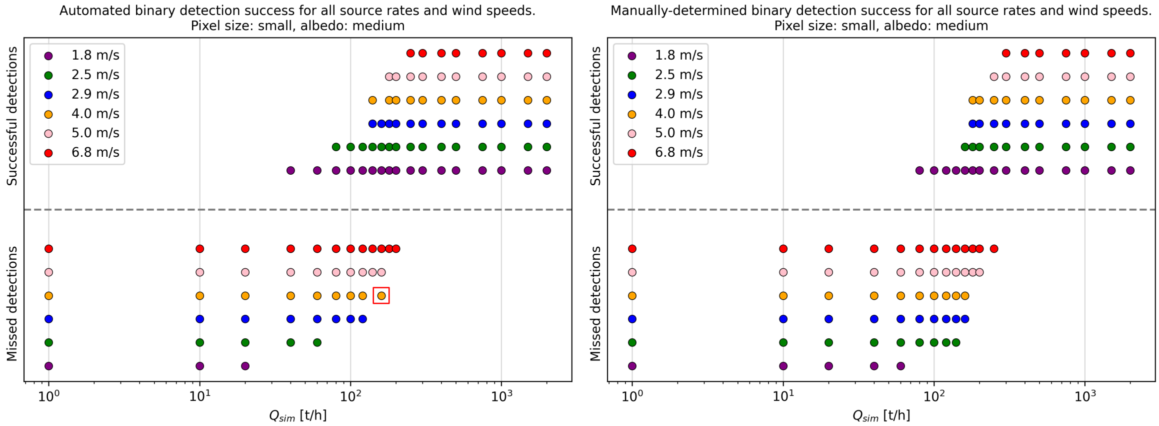

Figure 8.3: Automated (left) and manual (right) classification of binary detection success per simulated plume for small pixel size and medium albedo. Different colors indicate different meteorological conditions, classified by their spatiotemporal mean wind speed. The vertical axes qualitatively separate successful detections from missed detections. The red square is discussed in the text.

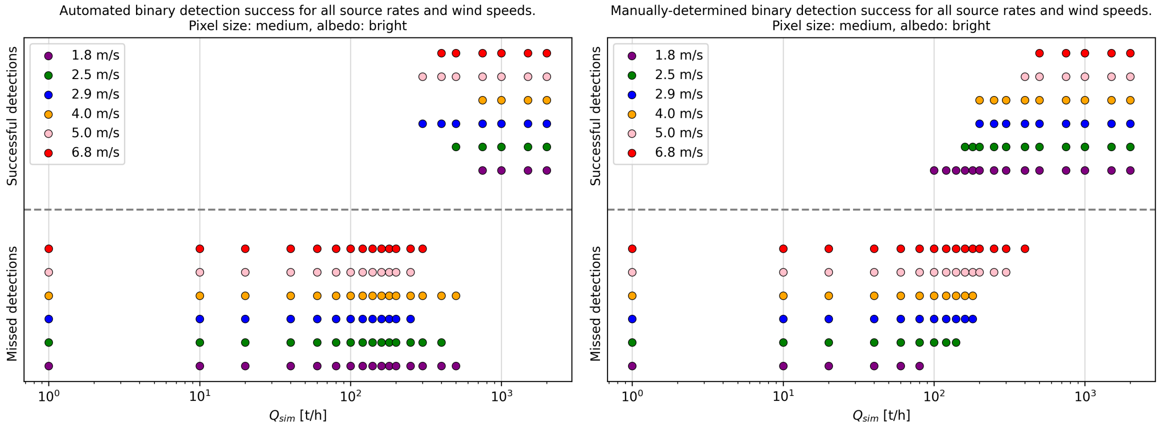

Figure 8.4: Automated (left) and manual (right) classification of binary detection success per simulated plume for medium pixel size and bright albedo.

8.1.3. Optimized predictor and inverse link functions

As presented in Section 6.2.1, the $\mathrm{POD}(\boldsymbol{x})_{m,n}$ functions are modeled as composites of a predictor function $g(\boldsymbol{x};\boldsymbol{\phi}_{m,n})$ and a continuous inverse link function $F(g(\boldsymbol{x};\boldsymbol{\phi}_{m,n}),\boldsymbol{\theta})$.

The purpose of the predictor function is to provide a non-negative output that increases with source rate and decreases with wind speed. This could be achieved with a linear formulation as a function of source rate and wind speed, such as $g(\boldsymbol{x};\boldsymbol{\phi}_{m,n}) = \phi_{0,m,n}Q + \phi_{1,m,n}U$ or $g(\boldsymbol{x};\boldsymbol{\phi}_{m,n}) = \frac{\phi_{0,m,n}Q}{\phi_{1,m,n}U}$. These formulations would result in lines of constant POD that converge to zero at zero wind speed ($\mathrm{Q} = \mathrm{U}_{10} = 0$). This means that an infinitesimally small source rate could be detected for zero wind speed [25]. This is impossible since GOES has a noise level that will always exceed an infinitesimally small enhancement. Hence, the function should be non-linear to avoid the convergence at the origin. The following generalized, non-linear form is considered for location (pixel size) m and albedo background n as a function of source rate and wind speed:

$$g(\boldsymbol{x};\boldsymbol{\phi}_{m,n}) = \phi_{0,m,n}\frac{\left(Q_{[\mathrm{th}^{-1}]} - \phi_{1,m,n}\right)^{\phi_{2,m,n}}}{\left(U_{[\mathrm{ms}^{-1}]} - \phi_{3,m,n}\right)^{\phi_{4,m,n}}}, \tag{8.1}$$

where the required units of the variables are stated in square brackets. Regardless of pixel size and albedo, coefficients ϕ_1 and ϕ_3 must be negative to ensure a physical (positive) POD at zero wind speed and zero source rate, which is required for the inverse link function since CDFs are only defined between 0 and 1. This formulation meets the requirements that it increases with source rate and decreases with wind speed. Other candidate functions that fulfill these requirements could be considered. As a result of splitting up the POD formulations into nine separate cases, the albedo and pixel size are not variables in $g(\boldsymbol{x};\boldsymbol{\phi}_{m,n})$, meaning fewer coefficients $\boldsymbol{\phi}$ are required in the minimization. The solar zenith and viewing zenith angles are not included here since the airmass causes very little error in the derived source rates that is not caused by the MBSP effect (see Section 7.3 and Figure 7.11).

The inverse link function maps the output of the predictor function to a continuous probability between 0 and 1 to indicate the probability of detection. For the inverse link function, the Burr CDF was selected [25]:

$$F(g,\boldsymbol{\theta}) = 1 - \left(1 + g^{\theta_0}\right)^{-\theta_1}, \tag{8.2}$$

which is independent of the pixel size or albedo. Preventing over-determination of the minimization problem (see Section 6.2.1) yields:

$$F(g, \boldsymbol{\theta}) = 1 - \left(1 + g^2\right)^{-1.5}. \tag{8.3}$$

[25] first discussed the use of the Burr CDF in airborne data. [107] analyzed different candidate inverse link functions proposed by [25] (such as Fréchet, Gamma, and Loglogistic distributions) to satellite data and found little difference in their results. Within the scope of this first attempt at deriving a POD for GOES, the conclusions of [107] were followed and the Burr CDF was selected. In further work, other formulations can be tested to verify this holds for GOES.

Using the binary detection results (1/0) based on the detectability metrics, minimizing the loglikelihood function of the Bernoulli distribution (see Equation 6.8) with a Nelder-Mead minimization algorithm results in the optimized predictor function coefficients $\phi_{m,n}$. Combining these with the inverse link function yields the optimized POD formulations for each combination of location and albedo. These are reported in Table 8.1.

Table 8.1: Optimized POD formulations for each combination of location and albedo using automated detection results.

Location & albedo	Optimized POD function
Coahuila, Mexico & desert	$\mathrm{POD} = 1 - \left(1 + \left(1.372 \cdot 10^{-5} \frac{\left(Q+6.364\cdot 10^{-2}\right)^{2.188}}{(U_{10}-2.380\cdot 10^{-2})^{8.990\cdot 10^{-2}}}\right)^2\right)^{-1.5}$
Coahuila, Mexico & farmland	$\mathrm{POD} = 1 - \left(1 + \left(2.210 \cdot 10^{-5} \frac{\left(Q+4.733\cdot 10^{-2}\right)^{3.254}}{(U_{10}+7.310\cdot 10^{-3})^{4.000}}\right)^2\right)^{-1.5}$
Coahuila, Mexico & forest	$\mathrm{POD} = 1 - \left(1 + \left(2.044 \cdot 10^{-6} \frac{\left(Q-1.261\cdot 10^{-2}\right)^{3.043}}{(U_{10}+1.383\cdot 10^{-2})^{2.755}}\right)^2\right)^{-1.5}$
South Dakota, US & desert	$\mathrm{POD} = 1 - \left(1 + \left(6.037 \cdot 10^{-9} \frac{\left(Q+1.107\cdot 10^{-2}\right)^{2.902}}{(U_{10}-7.727\cdot 10^{-3})^{-9.856\cdot 10^{-1}}}\right)^2\right)^{-1.5}$
South Dakota, US & farmland	$\mathrm{POD} = 1 - \left(1 + \left(1.081 \cdot 10^{-2} \frac{\left(Q-5.760\cdot 10^{-3}\right)^{1.485}}{(U_{10}+4.107\cdot 10^{-3})^{2.230}}\right)^2\right)^{-1.5}$
South Dakota, US & forest	$\mathrm{POD} = 1 - \left(1 + \left(5.229 \cdot 10^{-8} \frac{\left(Q+3.221\cdot 10^{-2}\right)^{3.110}}{(U_{10}-5.016\cdot 10^{-2})^{-3.450\cdot 10^{-1}}}\right)^2\right)^{-1.5}$
Idaho, US & desert	$\mathrm{POD} = 1 - \left(1 + \left(7.507 \cdot 10^{-9} \frac{\left(Q-7.354\cdot 10^{-3}\right)^{2.511}}{(U_{10}-1.021\cdot 10^{-2})^{-6.000\cdot 10^{-1}}}\right)^2\right)^{-1.5}$
Idaho, US & farmland	$\mathrm{POD} = 1 - \left(1 + \left(2.405 \cdot 10^{-3} \frac{\left(Q+1.798\cdot 10^{-2}\right)^{1.177}}{(U_{10}-1.842\cdot 10^{-2})^{3.733\cdot 10^{-1}}}\right)^2\right)^{-1.5}$
Idaho, US & forest	$\mathrm{POD} = 1 - \left(1 + \left(1.103 \cdot 10^{-7} \frac{\left(Q+4.310\cdot 10^{-3}\right)^{2.586}}{(U_{10}+5.344\cdot 10^{-4})^{1.228}}\right)^2\right)^{-1.5}$

8.1.4. Results and discussion

Figure 8.5 visualizes the POD functions of Table 8.1 in the Q-U_{10} domain for all nine combinations of pixel size and background albedo using the automated detection results. Figure 8.6 visualizes the POD functions using the manually-confirmed detection results. Both figures provide continuous probabilities of detection for a given source rate and wind speed. The black dashed lines indicate the contours of constant POD; 50%, 90% and 98% were selected as relevant percentages. Using the automated detection results, GOES has, for instance, a 50% POD to detect an emission rate of 115 th^{-1} at 1.8 ms^{-1} at locations with small pixel size and dark albedo, and a 98% POD to detect an emission rate of 770 th^{-1} at 5 ms^{-1} at locations with large pixel size and medium albedo. Source rates of hundreds of tonnes per hour are large and but have been detected by TROPOMI [65].

Figure 8.5 shows that the POD increases with increasing source rate for all combinations. This is expected since higher source rates result in higher enhancements above the background noise, which facilitates detection. For the pixel size and albedo combinations of small:medium, small:dark, medium:medium, large:medium and large:dark, lower wind speeds result in a higher POD. This is also as expected since low wind speeds lead to slower atmospheric dispersion and higher enhancements, which facilitates detection. However, there are large differences between the nine combinations. For medium:bright, medium:dark and large:bright, the POD decreases for decreasing wind speed. This is unexpected and non-physical behavior since lower wind speeds result in higher enhancements. The vertical dotted lines indicate the minimum and maximum wind speeds that were considered in the optimization of the predictor and inverse link functions (1.8–6.8 ms^{-1}). Hence, data points outside of this range are unconstrained and may not accurately capture the true behavior of those regions, especially if the POD variability is high (e.g. for medium pixel size and bright albedo). In future work, additional meteorological conditions with lower and higher spatiotemporal mean wind speeds could be added to constrain more data points.

The non-physical POD curves based on automated detectability results demonstrate the difficulty of using GOES for methane detections, which is expected from its low methane sensitivity. It also emphasizes that significant improvements and developments are required before GOES can provide a fully operational, near-real-time plume detection capability for strong methane leaks in North and South America without relying on reference detections by other instruments.

The POD curves based on manually-determined detections are shown in Figure 8.6. It shows that the manually-determined detection results cause large differences in POD compared to the automated detections, further emphasizing the need for a sensitivity analysis of the detection metrics. The non-physical behavior of decreasing POD with decreasing wind speed has disappeared. Compared to the automated case, the manual detection results show a 50% POD to detect an emission rate of 127 th^{-1} at 1.8 ms^{-1} at locations with a small pixel size and dark albedo, and a 98% POD to detect an emission rate of 775 th^{-1} at 5 ms^{-1} at locations with a large pixel size and medium albedo.

Like the automated detections, the manually-determined PODs also show the trend of increasing POD with increasing source rate for all combinations. However, unlike the automated detections, these POD curves also show a trend of decreasing POD for increasing pixel size for each albedo (the three columns), as shown by the increasing source rates for the three contour lines from small to large pixel sizes. This means that higher source rates are required to detect plumes near the edges of GOES' FOV (see Figure 2.14), which is as expected since larger pixel sizes mean plumes occupy fewer pixels and contain lower enhancements due to the dilution of the plume enhancements in a pixel by the surrounding noise.

A similar trend is not observed for increasingly dark albedos (the three rows). Even though the contour lines reach higher source rates when comparing only the bright and dark albedos, the medium albedo deviates from this trend since its contour lines are lower than bright and dark albedos for all three pixel sizes. This is unexpected since a darker albedo reflects less sunlight than a brighter albedo and should thus yield a higher retrieval noise level, which complicates plume detection. This deviation is likely caused by the medium albedo background selection. Farmland in Iowa, US was selected as the medium albedo and, since crops require water, the albedo scene contains multiple streams and rivers. This is shown by the dark, meandering lines in the farmland scene in Figure 6.5. Water strongly absorbs SWIR and thus creates retrieval artefacts, which complicates the detection. In addition, even though the selected reference days for the medium albedo are all within four days of each other, cloudy conditions between the reference days may bring precipitation, which affects the albedo of crops. The selected reference days in September (2021) are part of the harvest season, meaning that many crops will be fully grown and the albedo will be more sensitive to precipitation than at the start of the growing season. Hence, finding a homogeneous albedo background for a farmland scene for multiple reference days is difficult. These effects make the medium albedo a challenging scene for retrieving methane enhancements and plume detection. The effect of different stages of crop growth and precipitation on the albedo scene and plume detectability can be further investigated in future work.

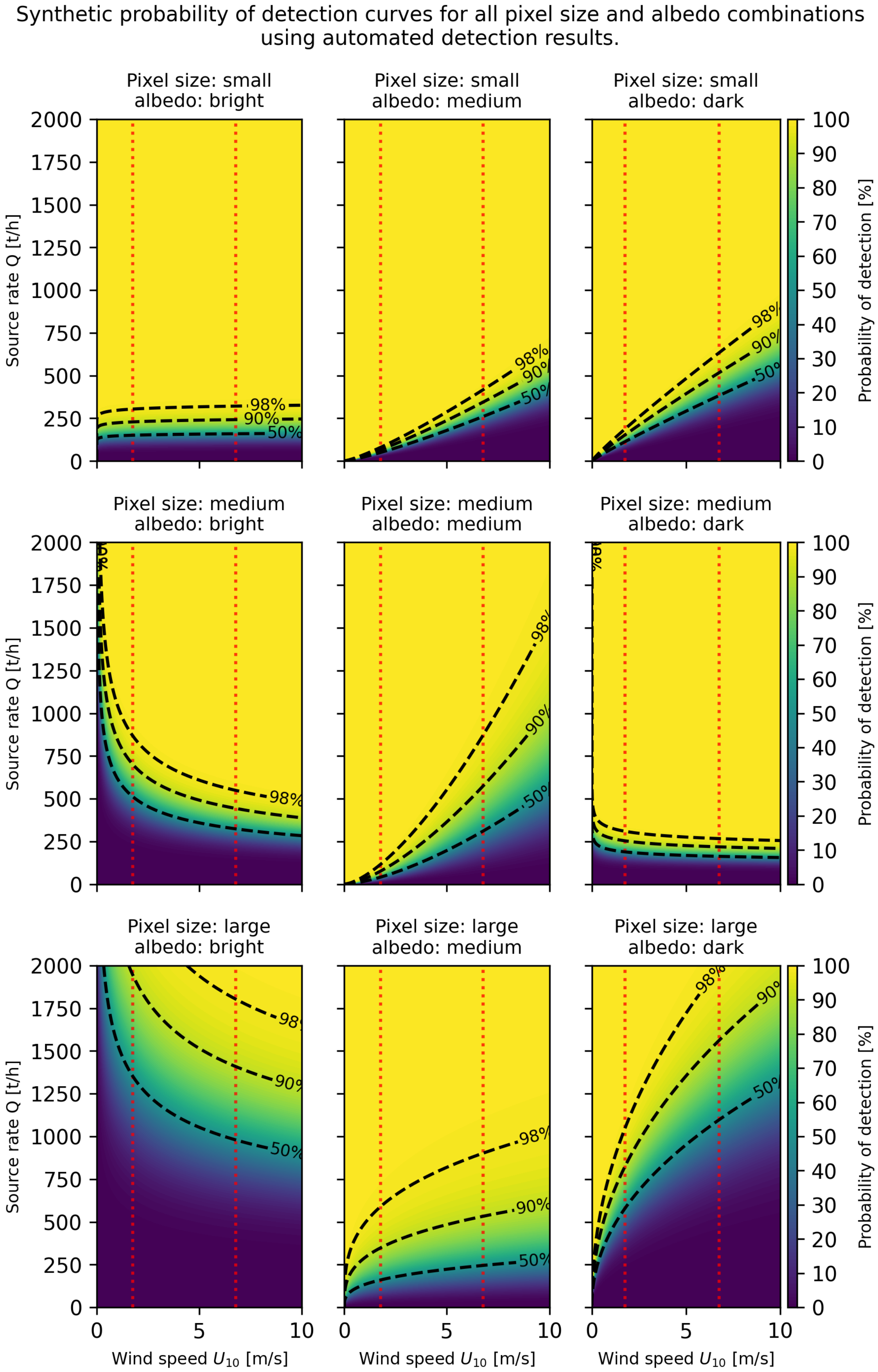

Figure 8.5: GOES' synthetic probability of detection functions using automated detection results. Probabilities as a function of 10-m wind speed and source rate at nine combinations of pixel size and albedo. Black dashed lines show contours of constant probability for 50%, 90% and 98%. Red dotted lines indicate the minimum and maximum wind speeds that constrain the PODs.

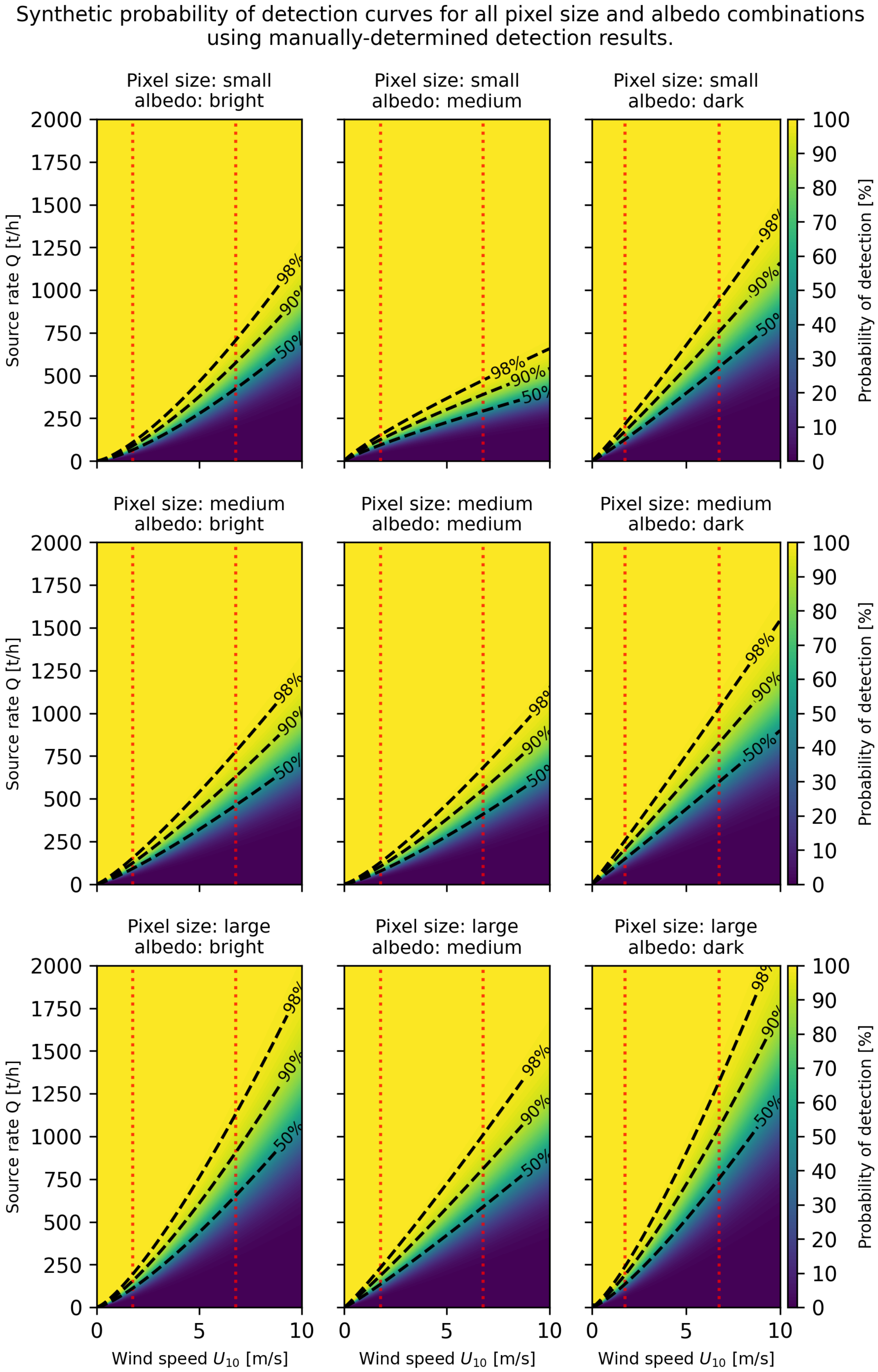

Figure 8.6: GOES' synthetic probability of detection functions using manually-confirmed detection results. Unlike the POD curves based on automated detection results, these curves show a clear trend of decreasing POD with increasing pixel size.

8.2. Validation of the synthetic PODs

In this section, the manually-determined, synthetic POD results are validated by comparing them to TROPOMI's source rate quantifications of reference detections based on the IME method and to previously published GOES quantifications [1]. In general, validation data should have small uncertainties to provide confidence that the data is the best approximation of the truth. Controlled methane release campaigns have been used for validate other methane-sensing instruments but, since these do not exist for GOES, a comparison to TROPOMI and existing quantifications was selected as the best validation strategy. The comparisons to TROPOMI and existing GOES quantifications are presented in Section 8.2.1 and Section 8.2.2, respectively.

8.2.1. Validation using TROPOMI reference detections

TROPOMI is very sensitive to methane emissions and its data has been used to detect methane plumes worldwide using a machine-learning detection algorithm at SRON [65]. TROPOMI reference detections can be used to check if GOES also detects a plume at the same time and location. GOES' methane sensitivity is low so the reference detections with the highest chance of being visible in GOES retrievals will have high enhancements because those cause strong methane absorption. Figure 8.7 shows a scatter plot of the TROPOMI-estimated plume lengths against the maximum enhancement for all TROPOMI detections in GOES CONUS FOV since 2018. Enhancements increase with decreasing plume length so suitable reference detections will thus be situated in the top-left corner. Two empirically defined thresholds are used to select suitable reference detections: an upper limit of 30 km for the plume length and a lower limit of 190 ppb for the maximum enhancement. This results in 17 reference detections that will be investigated with GOES. These thresholds could be lowered to include more detections.

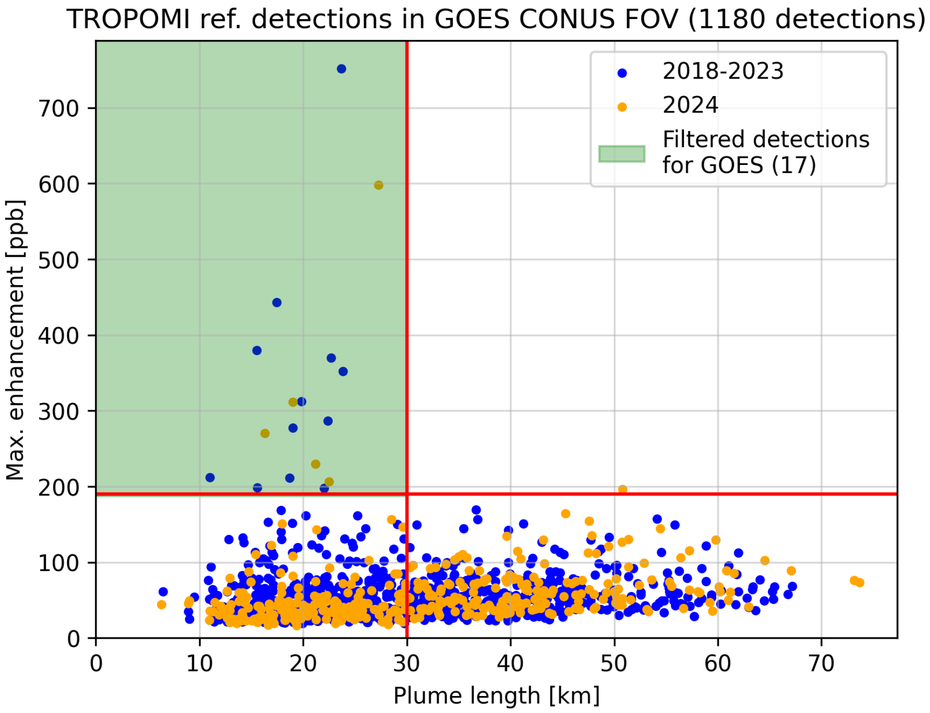

Figure 8.7: Filtering of TROPOMI reference detections in CONUS FOV for GOES retrievals. Final selection includes 17 reference detections based on empirically-defined thresholds for plume length and maximum enhancements. TROPOMI data from [65].

Figure 8.8 and Figure 8.9 provide an example of a successful and unsuccessful GOES detection of a reference plume from this set of 17 reference detections, respectively. Each row shows the recentered enhancements for a different reference day in the MBMP retrieval and each column is a different timestamp. The fourth column is closest to TROPOMI's detection time and shows the outline of the TROPOMI plume mask [65]. TROPOMI's source rate quantification using the IME method is given in the title. Figure 8.8 is a successful detection because the plume is clearly visible and TROPOMI's plume mask matches the plume. Figure 8.9 is an unsuccessful detection because no plume is visible above the noise near TROPOMI's plume mask. In total, 9 reference plumes were successfully detected, with TROPOMI-estimated source rates between 31 and 271 th^{-1}, and six plumes were not detected. For two plumes, the GOES detectability could not be determined due to proximity to large waterbodies or lack of radiance data. Most TROPOMI detections were in the medium pixel size and dark albedo category since this is the most common combination of pixel size and albedo across CONUS.

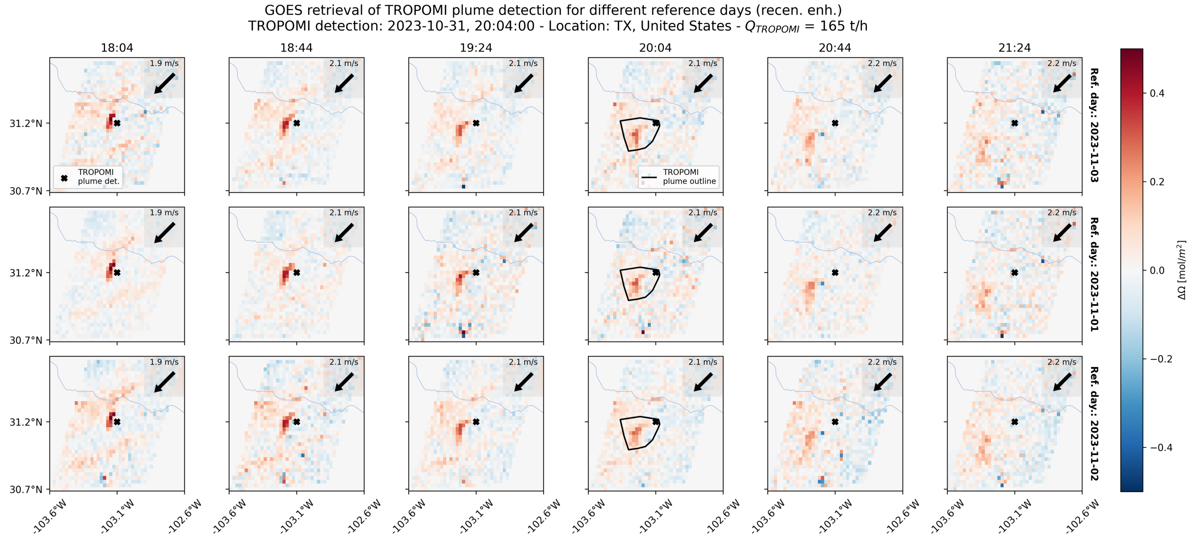

Figure 8.8: Demonstration of a successfully detected methane plume based on a TROPOMI reference detection. TROPOMI detection in Texas, US on October 31, 2023 at 20:04 UTC. Each row represents a different reference day in GOES' MBMP retrieval and each column is a different timestamp. The black cross indicates the detected plume location by TROPOMI and the black line outlines TROPOMI's plume mask [65]. Map data is plotted in the background. The spatiotemporal mean wind speed and direction are shown in the top right. Wind data from ERA5.

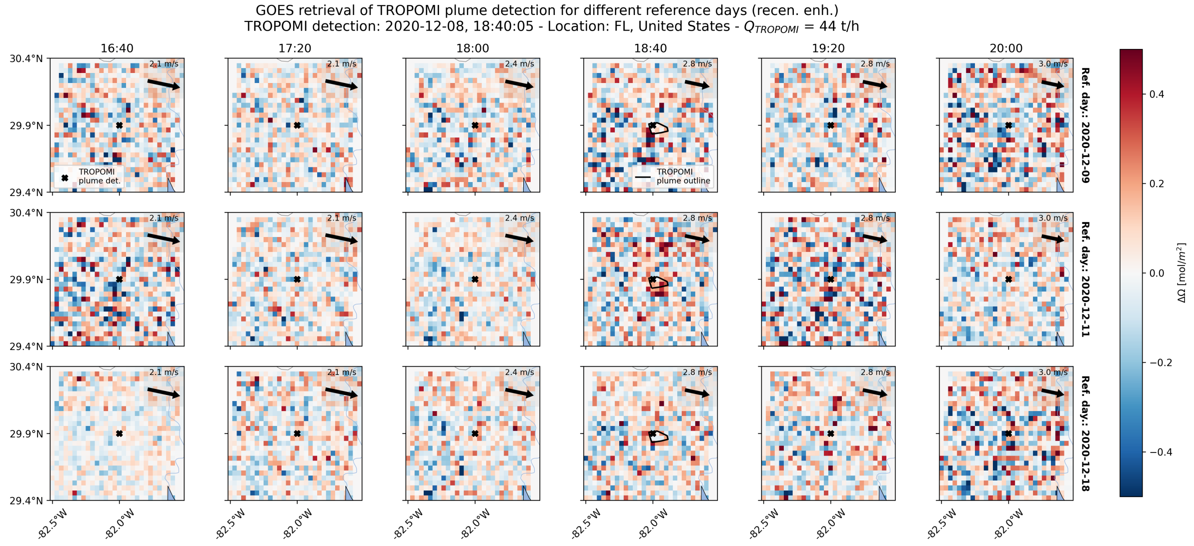

Figure 8.9: Demonstration of an unsuccessfully detected methane plume based on a TROPOMI reference detection. TROPOMI detection in Illinois, US on August 13, 2020 at 18:37 UTC.

TROPOMI has one overpass per day (except at high latitudes, where it has multiple) without temporal resolution so the IME method is the usual choice of source rate quantification method. The IME method relies on the total methane mass in the plume (integrated mass enhancement, IME) and external wind data for its quantification (see Section 5.4.1). Due to TROPOMI's high spectral resolution, the methane mass in the plume can be calculated with high certainty. The wind data, however, causes high uncertainties in the source rate quantification. In addition, the IME method implicitly assumes that the plume is still being emitted during the overpass since (in most cases) the actual emission duration is unknown [96]. This results in strongly biased source rate quantifications for short and intermittent emissions events, which are most suitable for detection by GOES. The next two paragraphs introduce two real-life emission events whose emission duration is known from reports to demonstrate this bias.

Pipeline blowout in Idaho, US

On October 12, 2023 at 10:30 local time, a natural gas pipeline was ruptured due to construction work in Idaho, US. According to a local news report, the leak lasted 25 minutes before the pipeline was shut off [108]. TROPOMI observed the resulting plume three hours after the end of the leak and quantified the total methane mass (IME) as 665 t. Ignoring any methane that dispersed from the plume below TROPOMI's masking threshold, this means the true source rate was almost 1600 th^{-1}. However, TROPOMI's source rate quantification using the IME method was 229 th^{-1}. [65]

Pipeline blowdown experiment in New Mexico, US

On October 8, 2024 at 17:26 local time, NOAA conducted a controlled release experiment with a blowdown (intentional venting) of a natural gas pipeline in New Mexico, US. The release lasted approximately one hour [109]. TROPOMI observed the resulting plume two hours after the start of the leak and quantified the total methane mass (IME) as 241 t. Ignoring dispersion, this means the true source rate was approximately 240 th^{-1}. However, TROPOMI calculated a source rate of 80 th^{-1}. [65]

These two emission events show that the source rate reported by the IME method cannot always be trusted and the true source rate can be multiple times higher. This complicates the validation strategy and prevents a direct comparison between TROPOMI's IME method source rate quantifications and the POD curves. To improve the comparison, a range of possible source rates is used for different hypothetical emission durations.

Figure 8.10 shows three manually-determined POD curves with the detection results of TROPOMI reference detection and ranges of possible source rate quantifications. The range is determined by assuming the accurate TROPOMI IME (the mass, not the method) is emitted in 1 hour and 30 minutes, based on the Idaho blowout and New Mexico blowdown cases. These POD curves were selected for comparison because their pixel size and albedo combination most closely resembles the most reference detections. The results show no successful reference detections with low PODs or unsuccessful reference detections with high PODs. This indicates a high probability that there are no strong signs of inconsistency between the POD curves and the reference detections. In addition, the left-most detection on the left POD curve shows a high POD ($\sim$90%) across its range of possible source rates. The Idaho blowout was successfully detected and shows a high POD ($>$98%) near its true source rate ($\sim$1600 th^{-1}). The New Mexico blowdown was also detected and has a POD around 60% at its true source rate ($\sim$240 th^{-1}). The unsuccessful detection at 2.5 ms^{-1} on the center curve has a low POD ($<$50%) across its range of hypothetical source rates. Collectively, these four cases demonstrate a high probability of consistency between the POD curves and the reference detections. In conclusion, the comparison shows no signs of strong inconsistency and multiple signs of strong consistency between the POD curves and the reference detections.

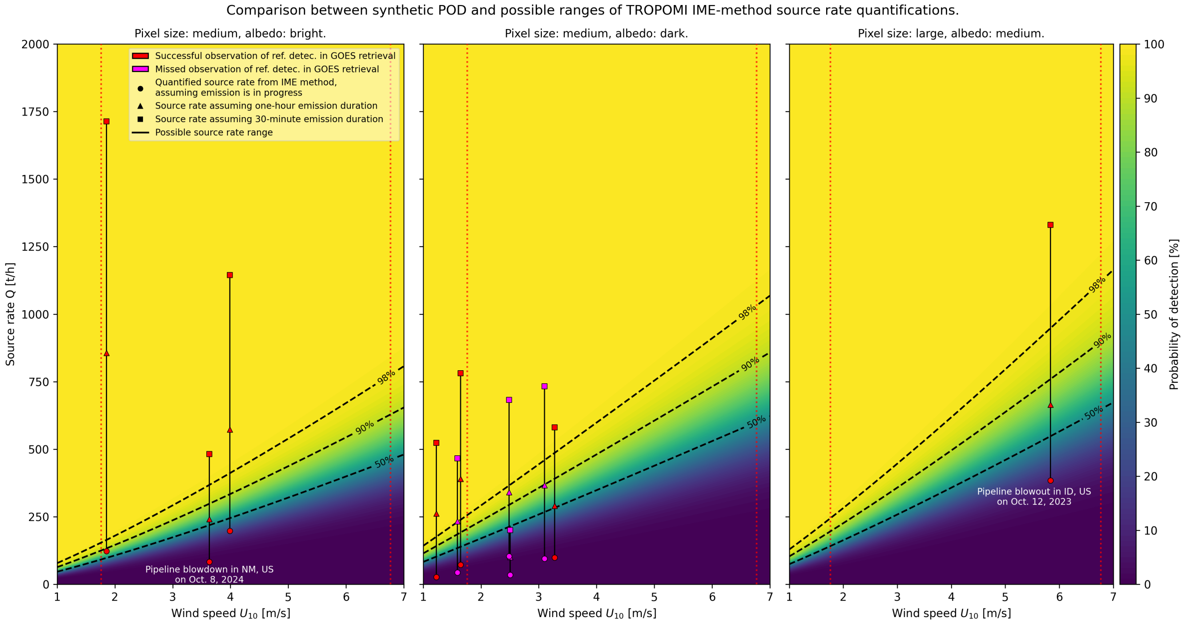

Figure 8.10: Comparison between synthetic POD curves and TROPOMI reference detections. Successful (red) and unsuccessful (magenta) GOES observations of TROPOMI reference detections for a range of hypothetical source rates (black vertical line). The Idaho blowout and the New Mexico blowdown are annotated on their respective POD curves.

8.2.2. Validation with published GOES source rate quantifications

In November 2023, [1] published seven GOES source rate quantifications of natural gas pipeline leaks in desert of Mexico in 2019. These quantifications are compared to the corresponding POD curve in Figure 8.11.

The comparison shows strong consistency for five of the seven reference quantifications because their PODs are above 99%, including for the full range of the one-sigma uncertainty of the main publication's quantification (no uncertainties are provided in the supplement). The other two quantifications show lower PODs (17 % 25%), notably for higher wind speeds. This could be caused by the difference between the reference days in the publication and the selected reference days to derive this POD curve, which are more than four years apart. Changes to surface types or albedo features that arose in that time may have decreased the POD. Another possibility is an underestimation of the source rate quantification. Further research is required to determine the underlying reason. In conclusion, the previously published GOES quantifications show a close match to the synthetic POD.

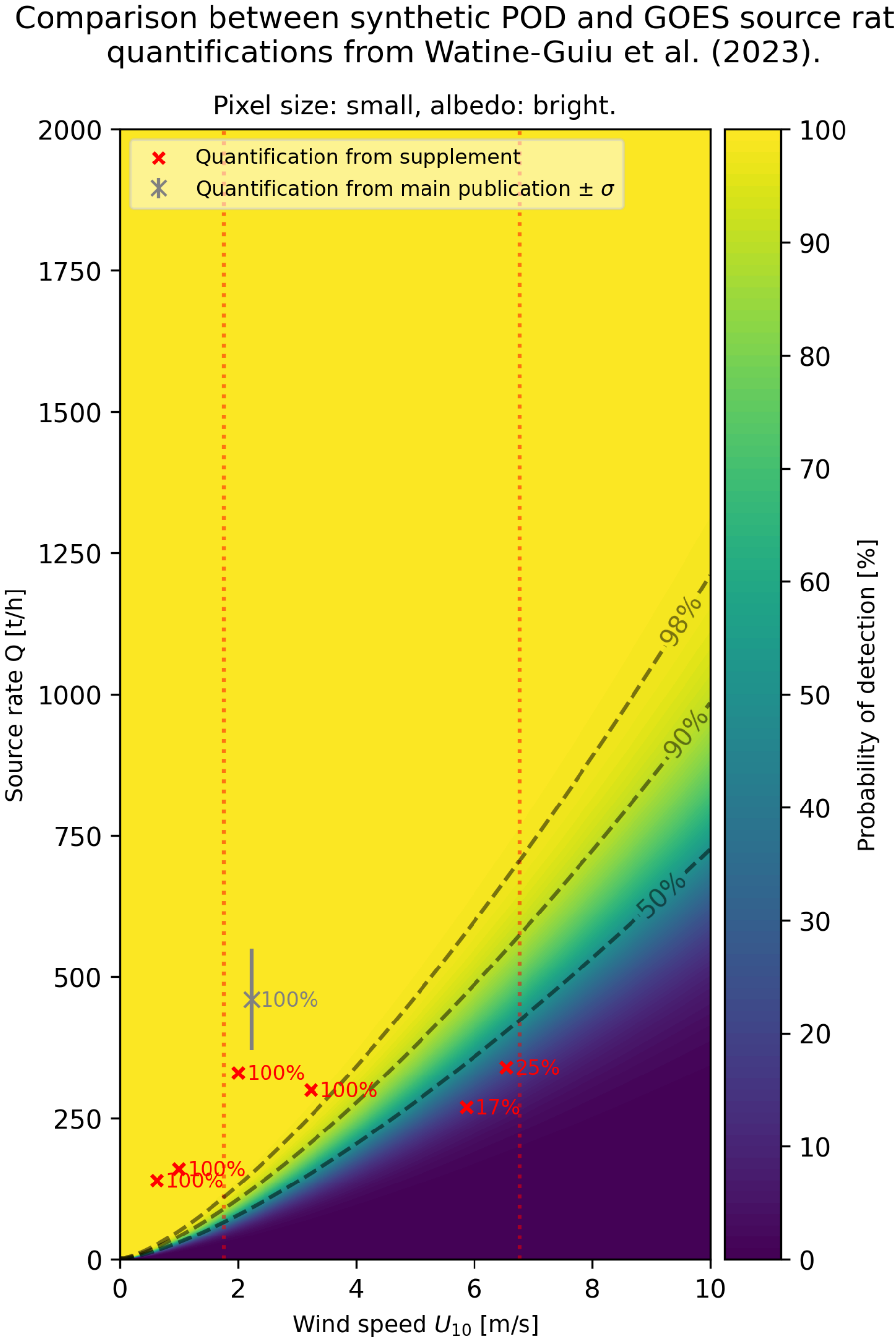

Figure 8.11: Comparison of synthetic POD curve to previously published GOES source rate quantifications. The crosses indicate GOES source rate quantifications from natural gas pipeline leaks in the Mexican desert in 2019 [1]. The percentages next to the markers indicate the derived POD of each quantification. The gray marker and error bar is the quantification from the main publication and the red markers are the quantifications from the publication's supplement.

Part IV

Closure

9

Conclusions

The goal of this thesis was to characterize and assess the capabilities of geostationary satellite data to monitor and quantify methane leaks. Methane is a potent greenhouse gas with a short lifetime and can be emitted in large quantities from oil & gas infrastructure. Methane leak monitoring and detection presents an effective opportunity for near-term climate change mitigation. The capabilities of the geostationary weather satellite GOES-16 (GOES) were investigated in this thesis due to its coverage of North and South America. A comprehensive assessment of GOES' quantitative methane leak monitoring capabilities did not exist before this thesis.

A probability of detection (POD) function was derived using simulated methane plumes under varying environmental conditions in a synthetic framework to assess the probability that GOES can detect a plume, thereby characterizing GOES' quantitative methane leak monitoring capabilities. POD functions based on manually-determined, binary detection results showed a trend of decreasing POD with increasing pixel size. This is as expected because plumes occupy fewer pixels when pixel sizes are large and the enhancements in those pixels will be lower due to the presence of more retrieval noise. Both of these effects complicate plume detection. A similar trend was not observed for increasingly dark albedo. Even though the POD did decrease between bright and dark albedo scenes (desert and forest backgrounds, respectively), the medium albedo scene (farmland background) showed higher PODs than both. This behavior is likely due to the presence of rivers and streams in the albedo scene, which cause retrieval artefacts and complicate detection.

Validation of the manually-determined, synthetic PODs was performed by comparing them to possible ranges of source rate quantifications of TROPOMI reference detections based on the IME method and to previously-published GOES source rate quantifications of methane leaks [1]. The range of source rates allowed for an improved comparison between the PODs and TROPOMI's source rate quantifications since the IME method is known to underestimate source rates of short intermittent. The comparison showed no signs of strong inconsistencies and multiple signs of strong consistencies between the POD curves and the reference detections.

Besides the manually determined detectability results, a first attempt at automatically determining plume detectability was devised using a set of metrics source rate quantifications. The resulting PODs showed highly variable and sometimes non-physical results with no clear trends in pixel size or albedo. The presence of artefacts and high noise levels in the methane column retrievals, caused by GOES' low methane sensitivity, significantly complicates the detection and quantification of plumes. A sensitivity analysis is needed to investigate the effect of changing the plume detectability metrics and improve their detectability results. Improvements to the retrieval methodology and plume masking are also required to reduce the sensitivity of the quantification results to the input data (see Chapter 10). This attempt demonstrated the complexity of automated plume detections across varying environmental conditions and highlighted the necessary improvements before GOES can be used to detect methane leaks without a priori reference data.

The work in this thesis has contributed to an improved understanding of the quantitative methane leak monitoring capabilities of GOES and has assessed the probability of successfully detecting methane plumes under varying environmental conditions. This characterization provides insight into when, where and under which conditions GOES can be used to provide plume detections at a unique temporal resolution to contribute to an improved understanding of large methane emissions. Until a dedicated geostationary satellite mission is launched, GOES forms a useful addition to the methane-sensing satellite constellation and a unique asset in the near-real-time detection of large methane emissions.

10

Recommendations and Future Work

This thesis has presented promising first results to characterize and assess the capabilities of geostationary satellite data to improve quantitative methane leak monitoring. Possibilities for improving the plume quantification and detection results remain. These improvements create opportunities for additional research questions to be answered to more robustly develop generalisable POD functions under varying locations and albedos. This chapter briefly discusses two improvements and three research directions that could be explored in future work to continue extending the capabilities of quantitative methane leak monitoring capabilities using GOES.

The first opportunity to improve GOES' methane retrievals is to reduce the effects of individually selected reference days. This thesis has shown the sensitivity of retrievals to differences in albedo between the target and reference days, and this remains one of the reasons why plume masking is particularly difficult with GOES. One possibility to decrease the sensitivity to the reference day is to collect an ensemble of suitable (cloud-free) reference days around a plume detection and create a synthetic reference day scene from the median per pixel of all reference days in the ensemble. This approach prevents individual albedo artefacts in the selected reference day from causing subsequent retrieval artefacts by using the most common albedo value across multiple reference days, thereby eliminating albedo outliers. Periods with persistent cloud cover make finding a suitable reference day very difficult because of the differences in albedo that occur due to precipitation and seasonal terrain changes. This problem would be circumvented by using a synthetic reference day. A second improvement opportunity is the calibration of the empirical c parameter in the MBSP retrieval for different surface types. Since the albedo is spectrally dependent, this calibration has the potential to improve the retrieval and reduce artefacts. A third improvement opportunity is to ensure that the observation window size is always as small as possible around the full extent of the plume to reduce the chances of albedo artefacts in the scene.

The first opportunity to improve GOES' plume quantification results lies in plume masking. Due to GOES' low methane sensitivity, the retrieval noise is often only slightly lower than the retrieved plume enhancements, making plume masking an inherently difficult problem. In addition, this thesis has shown the sensitivity of the quantification results to the plume masking thresholds. This strongly motivates that plume masking is an important area of improvement for more robust quantification results. One opportunity to improve the masking is by first applying a Gaussian filter to the retrieved enhancements. Similar to the application of the median filter, the Gaussian filter serves to smooth out enhancement artefacts and make the plume more pronounced. The masking thresholds could also be defined as a certain number of standard deviations above the mean instead of a percentile. This can reduce the sensitivity of the selected plume masking thresholds. Another possibility for improving the quantification is to apply a combination of binary erosion and/or dilation techniques to eliminate individual disconnected plume mask pixels from the main plume and fill in missing pixels that are fully surrounded by plume mask pixels. These techniques have been attempted to improve plume masking in this thesis but no generalisable combination was found.

A logical next research step to explore is the comparison of plume quantifications between GOES and TROPOMI or other LEO methane-observing satellites. Multiple aspects of these quantifications are interesting to compare. The first is a comparison of the total methane mass quantification (IME) between GOES and a LEO satellite. Both satellites' data should be used to retrieve the column enhancements and quantify the IME in the plume at the LEO satellite's overpass time. Since GOES has near-continuous coverage of CONUS, it can observe the plume dynamics continuously, in contrast to a LEO satellite's single overpass. A second comparison is of the source rate quantification. The source rate can be quantified using different methods, such as the IME method, the CSF method, the Gaussian plume inversion method and the source pixel method [96]. In the case of GOES, the source rate can be quantified using the d(IME)/dt method. The same methods can be applied to both satellites and their rate quantification results compared at the LEO satellite's overpass time. A third comparison is between the results of the separate source rate quantification methods. Here, a different method can be used by both satellites and their respective results compared. Since the d(IME)/dt method is novel and unique to GOES, comparing its result to other source rate quantification methods is a clear next step. The methodology and code pipeline that was developed in this thesis can serve as an efficient starting point for all three of these comparisons.

A second and more challenging research step is to investigate GOES' extensive data record to explore methods to search for methane leaks without relying on a priori reference detections by TROPOMI. Some of the challenges include the computationally-intensive processing of large amounts of GOES radiance data, automatically detecting plumes among significant retrieval artefacts caused by GOES' low methane sensitivity and masking the plume enhancements that may be only marginally above the background without a priori information on the source location. To this end, training a convolutional neural network can be a scalable and effective approach, as demonstrated by [65] with TROPOMI data. Developing this methodology into an operational-level data product would be highly desirable since it would allow near-real-time detections of methane plumes (that are detectable under the POD) in North and South America, but significant further research is required to improve the methodology to achieve this.

GOES has proven itself to be a uniquely positioned instrument to detect large and concentrated methane plumes at a high temporal resolution. Even though significant challenges remain and further research is required, further developing the GOES retrieval and quantification methodology can lead to a fully operational, near-real-time plume detection capability for strong plumes in North and South America.

Reference List

[1] M. Watine-Guiu et al. “Geostationary satellite observations of extreme and transient methane emissions from oil and gas infrastructure”. In: *Proceedings of the National Academy of Sciences of the United States of America* 120.52 (2023). DOI: 10.1073/pnas.2310797120.

[2] K. Calvin et al. *IPCC, 2023: Climate Change 2023: Synthesis Report. Contribution of Working Groups I, II and III to the Sixth Assessment Report of the Intergovernmental Panel on Climate Change [Core Writing Team, H. Lee and J. Romero (eds.)]. IPCC, Geneva, Switzerland.* Tech. rep. Intergovernmental Panel on Climate Change, July 2023. DOI: 10.59327/IPCC/AR6-9789291691647.

[3] IPCC. “Summary for Policymakers”. In: *Climate Change 2021: The Physical Science Basis. Contribution of Working Group I to the Sixth Assessment Report of the Intergovernmental Panel on Climate Change.* Ed. by V. Masson-Delmotte et al. Cambridge, United Kingdom and New York, NY, USA: Cambridge University Press, 2021, 3-32. DOI: 10.1017/9781009157896.001.

[4] Intergovernmental Panel on Climate Change. *Climate Change 2021 – The Physical Science Basis.* Tech. rep. Intergovernmental Panel on Climate Change, July 2023. DOI: 10.1017/9781009157896.

[5] E. Dlugokencky et al. “The growth rate and distribution of atmospheric methane”. In: *Journal of Geophysical Research: Atmospheres* 99.D8 (1994), pp. 17021–17043. DOI: https://doi.org/10.1029/94JD01245.

[6] T. F. Stocker et al. “Climate Change 2013 – The Physical Science Basis: Working Group I Contribution to the Fifth Assessment Report of the Intergovernmental Panel on Climate Change”. In: *Climate Change 2013 the Physical Science Basis: Working Group I Contribution to the Fifth Assessment Report of the Intergovernmental Panel on Climate Change* 9781107057999 (Jan. 2014), pp. 1–1535. DOI: 10.1017/CBO9781107415324.

[7] M. J. Prather, C. D. Holmes, and J. Hsu. “Reactive greenhouse gas scenarios: Systematic exploration of uncertainties and the role of atmospheric chemistry”. In: *Geophysical Research Letters* 39.9 (May 2012), p. 9803. DOI: 10.1029/2012GL051440.

[8] D. A. Malashock et al. “Global trends in ozone concentration and attributable mortality for urban, peri-urban, and rural areas between 2000 and 2019: a modelling study”. In: *The Lancet Planetary Health* 6.12 (Dec. 2022), e958–e967. DOI: 10.1016/S2542-5196(22)00260-1.

[9] A. Krol. *What makes methane a more potent greenhouse gas than carbon dioxide?* Dec. 2023.

[10] D. Shindell et al. *Anthropogenic and Natural Radiative Forcing. In: Climate Change 2013: The Physical Science Basis. Contribution of Working Group I.* Tech. rep. Cambridge, UK: IPCC, 2013.

[11] J. S. Levine, W. R. Cofer III, and J. P. Pinto. *Biomass Burning.* Tech. rep. Hampton: NASA Langley Research Center, 1993.

[12] Z. Lyu et al. “Methanogenesis”. In: *Current biology : CB* 28.13 (July 2018), R727–R732. DOI: 10.1016/J.CUB.2018.05.021.

[13] A. R. Moss, J. P. Jouany, and J. Newbold. “Methane production by ruminants: its contribution to global warming”. In: *Annales de Zootechnie* 49.3 (May 2000), pp. 231–253. DOI: 10.1051/ANIMRES:2000119.

[14] K. Minami and H. U. Neue. “Rice paddies as a methane source”. In: *Climatic Change* 27.1 (May 1994), pp. 13–26. DOI: 10.1007/BF01098470/METRICS.

[15] R. A. Alvarez et al. “Assessment of methane emissions from the U.S. oil and gas supply chain”. In: *Science* 361.6398 (July 2018), pp. 186–188. DOI: 10.1126/science.aar7204.

[16] The World Bank. *Global Flaring and Methane Reduction Partnership (GFMR).*

[17] International Energy Agency. *Methane Tracker 2020.* 2020.

[18] US EPA. *Greenhouse Gas Equivalencies Calculator.* 2024.

[19] Katja Riedel and Keith Lassey. “"Detergent of the atmosphere" | NIWA”. In: *Water & Atmosphere* 16.1 (2008).

[20] R. V. Blundell et al. "Rates of radical reactions in methane oxidation". In: *Symposium (International) on Combustion* 10.1 (1965), pp. 445–452. DOI: `https://doi.org/10.1016/S0082-0784(65)80191-6`.

[21] O. Boucher et al. "The indirect global warming potential and global temperature change potential due to methane oxidation". In: *Environmental Research Letters* 4.4 (2009). DOI: `10.1088/1748-9326/4/4/044007`.

[22] D. T. Allen. "Methane emissions from natural gas production and use: reconciling bottom-up and top-down measurements". In: *Current Opinion in Chemical Engineering* 5 (2014), pp. 78–83. DOI: `https://doi.org/10.1016/j.coche.2014.05.004`.

[23] M. Dogniaux. "Suivi de la concentration atmosphérique de CO2 par satellite: performances et sensibilités des prochains concepts d'observation dans le proche infrarouge". PhD thesis. Paris: École doctorale de l'Institut polytechnique de Paris, Dec. 2021.

[24] B. Chen, J. M. Chen, and D. E. Worthy. "Interannual variability in the atmospheric CO2 rectification over a boreal forest region". In: *Journal of Geophysical Research: Atmospheres* 110.D16 (Aug. 2005), pp. 1–12. DOI: `10.1029/2004JD005546`.

[25] B. M. Conrad, D. R. Tyner, and M. R. Johnson. "Robust probabilities of detection and quantification uncertainty for aerial methane detection: Examples for three airborne technologies". In: *Remote Sensing of Environment* 288 (Apr. 2023), p. 113499. DOI: `10.1016/J.RSE.2023.113499`.

[26] I. B. Ocko et al. "Acting rapidly to deploy readily available methane mitigation measures by sector can immediately slow global warming". In: *Environmental Research Letters* 16.5 (May 2021), p. 54042. DOI: `10.1088/1748-9326/abf9c8`.

[27] D. Zavala-Araiza et al. "Methane emissions from oil and gas production sites in Alberta, Canada". In: *Elementa* 6 (Jan. 2018). DOI: `10.1525/ELEMENTA.284/112796`.

[28] International Energy Agency (IEA). *World Energy Outlook*. Tech. rep. 2017.

[29] L. Höglund-Isaksson et al. "Technical potentials and costs for reducing global anthropogenic methane emissions in the 2050 timeframe –results from the GAINS model". In: *Environmental Research Communications* 2.2 (Feb. 2020), p. 025004. DOI: `10.1088/2515-7620/AB7457`.

[30] I. Karakurt, G. Aydin, and K. Aydiner. "Mine ventilation air methane as a sustainable energy source". In: *Renewable and Sustainable Energy Reviews* 15.2 (2011), pp. 1042–1049. DOI: `https://doi.org/10.1016/j.rser.2010.11.030`.

[31] V. Baca-González et al. "Are Vaccines the Solution for Methane Emissions from Ruminants? A Systematic Review". In: *Vaccines* 8.3 (2020), p. 460. DOI: `10.3390/VACCINES8030460`.

[32] G. C. Waghorn and R. S. Hegarty. "Lowering ruminant methane emissions through improved feed conversion efficiency". In: *Animal Feed Science and Technology* 166-167 (2011), pp. 291–301. DOI: `https://doi.org/10.1016/j.anifeedsci.2011.04.019`.

[33] Environmental Protection Agency (EPA). *Global Non-CO2 Greenhouse Gas Emission Projections & Mitigation: 2015–2050*. Tech. rep. Washington, DC: EPA, Oct. 2019.

[34] B. C. Ball, A. Scott, and J. P. Parker. "Field N2O, CO2 and CH4 fluxes in relation to tillage, compaction and soil quality in Scotland". In: *Soil and Tillage Research* 53.1 (1999), pp. 29–39. DOI: `https://doi.org/10.1016/S0167-1987(99)00074-4`.

[35] S. Kirschke et al. "Three decades of global methane sources and sinks". In: *Nature Geoscience 2013 6:10* 6.10 (Sept. 2013), pp. 813–823. DOI: `10.1038/ngeo1955`.

[36] J. F. Dooley et al. "A new aerial approach for quantifying and attributing methane emissions: implementation and validation". In: *Atmospheric Measurement Techniques* 17.17 (Sept. 2024), pp. 5091–5111. DOI: `10.5194/AMT-17-5091-2024`.

[37] A. Karion et al. "Methane emissions estimate from airborne measurements over a western United States natural gas field". In: *Geophysical Research Letters* 40.16 (Aug. 2013), pp. 4393–4397. DOI: `10.1002/GRL.50811`.

[38] B. Schrader. "General survey of vibrational spectroscopy". In: *Infrared and Raman Spectroscopy*. John Wiley & Sons, Ltd, 1995. Chap. 2, pp. 7–61. DOI: `https://doi.org/10.1002/9783527615438.ch02`.

[39] Jon Chui. *Spectroscopy Overview*. Jan. 2011.

[40] D. J. Jacob et al. "Satellite observations of atmospheric methane and their value for quantifying methane emissions". In: *Atmospheric Chemistry and Physics* 16.22 (Nov. 2016), pp. 14371–14396. DOI: `10.5194/ACP-16-14371-2016`.

[41] D. Li, M. Saito, and P. Yang. “Time-Dependent Systematic Biases in Inferring Ice Cloud Properties from Geostationary Satellite Observations”. In: *Remote Sensing* 15.3 (2023). DOI: `10.3390/rs15030855`.

[42] D. J. Varon et al. “High-frequency monitoring of anomalous methane point sources with multispectral Sentinel-2 satellite observations”. In: *Atmospheric Measurement Techniques* 14.4 (Apr. 2021), pp. 2771–2785. DOI: `10.5194/amt-14-2771-2021`.

[43] D. J. Jacob et al. *Quantifying methane emissions from the global scale down to point sources using satellite observations of atmospheric methane*. July 2022. DOI: `10.5194/acp-22-9617-2022`.

[44] J. R. Worden et al. “Quantifying lower tropospheric methane concentrations using GOSAT near-IR and TES thermal IR measurements”. In: *Atmospheric Measurement Techniques* 8.8 (2015), pp. 3433–3445. DOI: `10.5194/amt-8-3433-2015`.

[45] H. Petetin et al. “Potential of TROPOMI for understanding spatio-temporal variations in surface NO 2 and their dependencies upon land use over the Iberian Peninsula”. In: *Atmos. Chem. Phys* 23 (2023), pp. 3905–3935. DOI: `10.5194/acp-23-3905-2023`.

[46] I. Aben. “Methane Emissions Detection Using Satellites Assessment”. In: ().

[47] World Meteorological Organization. *WMO OSCAR | Satellite: GHGSat*. Nov. 2023.

[48] ESA. *GHGSat - Earth Online*.

[49] GHGSat Inc. *2022 GHGSAT METHANE EMISSIONS REPORT*. Tech. rep. Houston: GHGSat, 2022.

[50] D. Jervis et al. “The GHGSat-D imaging spectrometer”. In: *Atmospheric Measurement Techniques* 14.3 (2021), pp. 2127–2140.

[51] World Meteorological Organization. *WMO OSCAR | Satellite: MethaneSAT*.

[52] T. E. Taylor et al. “An 11-year record of XCO_2 estimates derived from GOSAT measurements using the NASA ACOS version 9 retrieval algorithm”. In: *Earth System Science Data* 14.1 (2022), pp. 325–360. DOI: `10.5194/essd-14-325-2022`.

[53] World Meteorological Organization. *WMO OSCAR | Satellite: PRISMA*.

[54] L. Guanter et al. “Mapping methane point emissions with the PRISMA spaceborne imaging spectrometer”. In: *Remote Sensing of Environment* 265 (2021), p. 112671. DOI: `https://doi.org/10.1016/j.rse.2021.112671`.

[55] K. F. Huemmrich et al. “ISS as a Platform for Optical Remote Sensing of Ecosystem Carbon Fluxes: A Case Study Using HICO”. In: *IEEE Journal of Selected Topics in Applied Earth Observations and Remote Sensing* 10.10 (Oct. 2017), pp. 4360–4375. DOI: `10.1109/JSTARS.2017.2725825`.

[56] IEA. *Progress on data and lingering uncertainties – Global Methane Tracker 2024*.

[57] N2YO. *Satellite details - Object 149AR*.

[58] World Meteorological Organization. *WMO OSCAR | Satellite: EnMAP*.

[59] *Landsat 8 | Landsat Science*.

[60] T. Ehret et al. “Global Tracking and Quantification of Oil and Gas Methane Emissions from Recurrent Sentinel-2 Imagery”. In: (2022).

[61] R. Binet et al. “Accurate Sentinel-2 inter-band time delays”. In: *ISPRS Annals of the Photogrammetry, Remote Sensing and Spatial Information Sciences* V-1-2022.1 (May 2022), pp. 57–66. DOI: `10.5194/ISPRS-ANNALS-V-1-2022-57-2022`.

[62] T. A. de Jong et al. “Daily global methane super-emitter detection and source identification with sub-daily tracking”. In: *Geophysical Research Letters* (Feb. 2024). DOI: `10.31223/X51M5T`.

[63] World Meteorological Organization. *WMO OSCAR | Details for Instrument VIIRS*. Oct. 2022.

[64] *Tobias de Jong, SRON, personal communication, December 2024*.

[65] B. J. Schuit et al. “Automated detection and monitoring of methane super-emitters using satellite data”. In: *Atmospheric Chemistry and Physics* 23.16 (2023), pp. 9071–9098. DOI: `10.5194/acp-23-9071-2023`.

[66] I. Irakulis-Loitxate et al. “Satellites Detect a Methane Ultra-emission Event from an Offshore Platform in the Gulf of Mexico”. In: *Environmental Science and Technology Letters* 9.6 (June 2022), pp. 520–525. DOI: `10.1021/acs.estlett.2c00225`.

[67] I. Irakulis-Loitxate et al. “Satellites Detect Abatable Super-Emissions in One of the World’s Largest Methane Hotspot Regions”. In: *Environmental Science and Technology* 56.4 (Feb. 2022), pp. 2143–2152. DOI: `10.1021/acs.est.1c04873`.

[68] M. Dogniaux et al. “Report on Landsat 8 and Sentinel-2B observations of the Nord Stream 2 pipeline methane leak”. In: *Atmospheric Measurement Techniques* 17.9 (2024), pp. 2777–2787. DOI: `10.5194/amt-17-2777-2024`.

[69] I. Ialongo et al. "Comparison of TROPOMI/Sentinel-5 Precursor NO_2 observations with ground-based measurements in Helsinki". In: *Atmospheric Measurement Techniques* 13.1 (2020), pp. 205–218. DOI: `10.5194/amt-13-205-2020`.

[70] ESA and ATG media. *Sentinel 5P.* June 2017.

[71] Pepijn Veefkind, Arno Keppens, and Johan de Haan. *TROPOMI ATBD Ozone Profile.* Tech. rep. 1.0.0. Royal Netherlands Meteorological Institute, Oct. 2021.

[72] European Space Agency (ESA). *Sentinel-5 Precursor Level 1B Radiances - Sentinel Online.*

[73] M. Bauwens et al. "Impact of Coronavirus Outbreak on NO2 Pollution Assessed Using TROPOMI and OMI Observations". In: *Geophysical Research Letters* 47.11 (2020), e2020GL087978. DOI: `https://doi.org/10.1029/2020GL087978`.

[74] N. Theys et al. "Sulfur dioxide retrievals from TROPOMI onboard Sentinel-5 Precursor: algorithm theoretical basis". In: *Atmospheric Measurement Techniques* 10.1 (2017), pp. 119–153. DOI: `10.5194/amt-10-119-2017`.

[75] Z. Qu et al. "Global distribution of methane emissions: a comparative inverse analysis of observations from the TROPOMI and GOSAT satellite instruments". In: *Atmospheric Chemistry and Physics* 21.18 (2021), pp. 14159–14175. DOI: `10.5194/acp-21-14159-2021`.

[76] Z. Chen et al. "Methane emissions from China: a high-resolution inversion of TROPOMI satellite observations". In: *Atmospheric Chemistry and Physics* 22.16 (2022), pp. 10809–10826. DOI: `10.5194/acp-22-10809-2022`.

[77] Y. Zhang et al. "Quantifying methane emissions from the largest oil-producing basin in the United States from space". In: *Science Advances* 6.17 (2020), eaaz5120. DOI: `10.1126/sciadv.aaz5120`.

[78] J. A. de Gouw et al. "Daily Satellite Observations of Methane from Oil and Gas Production Regions in the United States". In: *Scientific Reports* 10.1 (2020), p. 1379. DOI: `10.1038/s41598-020-57678-4`.

[79] O. Schneising et al. "Remote sensing of methane leakage from natural gas and petroleum systems revisited". In: *Atmospheric Chemistry and Physics* 20.15 (2020), pp. 9169–9182. DOI: `10.5194/acp-20-9169-2020`.

[80] S. Pandey et al. "Satellite observations reveal extreme methane leakage from a natural gas well blowout". In: *Proceedings of the National Academy of Sciences* 116.52 (2019), pp. 26376–26381. DOI: `10.1073/pnas.1908712116`.

[81] J. D. Maasakkers et al. "Reconstructing and quantifying methane emissions from the full duration of a 38-day natural gas well blowout using space-based observations". In: *Remote Sensing of Environment* 270 (2022), p. 112755. DOI: `https://doi.org/10.1016/j.rse.2021.112755`.

[82] J. D. Maasakkers et al. "Using satellites to uncover large methane emissions from landfills". In: *Science Advances* 8.32 (2022), eabn9683. DOI: `10.1126/sciadv.abn9683`.

[83] SRON Earth Team. *Methane Plume Maps - SRON Earth.* 2024.

[84] NOAA Satellite Information System. *GOES Overview.*

[85] T. J. Schmit et al. "Applications of the 16 spectral bands on the Advanced Baseline Imager (ABI)". In: *J. Operational Meteor* 6.4 (2018), pp. 33–46. DOI: `10.15191/nwajom.2018.0604`.

[86] NOAA and NASA. *GOES-R Series Instruments: Advance Baseline Imager (ABI).*

[87] NOAA. *Transforming Energy into Imagery: How Satellite Data Becomes Stunning Views of Earth | NESDIS.* Mar. 2020.

[88] International US Energy Information Administration (EIA). *What countries are the top producers and consumers of oil?* Sept. 2023.

[89] T. J. Schmit et al. "A Closer Look at the ABI on the GOES-R Series". In: *Bulletin of the American Meteorological Society* 98.4 (Apr. 2017), pp. 681–698. DOI: `10.1175/BAMS-D-15-00230.1`.

[90] Alexis Benz et al. *GOES-R Series Data Book.* Tech. rep. Greenbelt, Maryland: National Aeronautics and Space Administration, GOES-R Series Program Office, Goddard Space Flight Center, Apr. 2019.

[91] R. R. Draxler et al. "An Overview of the HYSPLIT 4 Modelling System for Trajectories, Dispersion, and Deposition". In: *Australian Meteorological Magazine* 47 (1998), pp. 295–308.

[92] National Oceanic and Atmospheric Administration, National Aeronautics and Space Administration, and US Air Force. *U.S. Standard Atmosphere, 1976.* 1976.

[93] G. P. Anderson et al. *AFGL (Air Force Geophysical Laboratory) atmospheric constituent profiles (0-120km).* Tech. rep. Hanscom AFB, MA (USA): Air Force Geophysics Lab, 1986.

[94] I. E. Gordon et al. “The HITRAN2016 molecular spectroscopic database”. In: *Journal of Quantitative Spectroscopy and Radiative Transfer* 203 (2017), pp. 3–69. DOI: https://doi.org/10.1016/j.jqsrt.2017.06.038.

[95] O. M. Coddington et al. “The TSIS-1 Hybrid Solar Reference Spectrum”. In: *Geophysical Research Letters* 48.12 (2021), e2020GL091709. DOI: https://doi.org/10.1029/2020GL091709.

[96] D. J. Varon et al. “Quantifying methane point sources from fine-scale satellite observations of atmospheric methane plumes”. In: *Atmospheric Measurement Techniques* 11.10 (Oct. 2018), pp. 5673–5686. DOI: 10.5194/amt-11-5673-2018.

[97] Robert Lucchesi. *File Specification for GEOS FP*. Tech. rep. Global Modeling and Assimilation Office, 2018.

[98] H. Hersbach et al. *ERA5 hourly data on single levels from 1940 to present*. June 2018. DOI: 10.24381/cds.adbb2d47.

[99] R. Draxler et al. *HYSPLIT USER’s GUIDE*. Tech. rep. National Oceanic and Atmospheric Administration (NOAA), Nov. 2023.

[100] National Oceanic and Atmospheric Administration. *HYSPLIT Limitations*.

[101] D. H. Cusworth et al. “Intermittency of Large Methane Emitters in the Permian Basin”. In: *Environmental Science & Technology Letters* 8.7 (July 2021), pp. 567–573. DOI: 10.1021/acs.estlett.1c00173.

[102] U.S. Department of Commerce (DOC) et al. *GOES R SERIES PRODUCT DEFINITION AND USERS’ GUIDE*. Tech. rep. NOAA, Dec. 2019.

[103] C. D. Rodgers. *Inverse Methods for Atmospheric Sounding: Theory and Practice*. Series on atmospheric, oceanic and planetary physics. World Scientific, 2000.

[104] S. R. Eliason. *Maximum Likelihood Estimation: Logic and Practice*. Maximum Likelihood Estimation no. 96. SAGE Publications, 1993.

[105] F. Gao and L. Han. “Implementing the Nelder-Mead simplex algorithm with adaptive parameters”. In: *Computational Optimization and Applications* 51.1 (2012), pp. 259–277. DOI: 10.1007/s10589-010-9329-3.

[106] C. Winters-Michaud et al. *Major uses of land in the United States, 2017*. Washington, D.C, Sept. 2024. DOI: 10113/8633522.

[107] A. K. Ayasse et al. “Probability of Detection and Multi-Sensor Persistence of Methane Emissions from Coincident Airborne and Satellite Observations”. In: *Environment Science & Technology* (July 2024). DOI: 10.31223/X5012H.

[108] R. Spacek and A. Brizee. “Middleton gas line explodes; shelter-in-place order lifted”. In: *Idaho Statesman* (Oct. 2023).

[109] NESDIS. *NOAA’s GOES Satellites Can Provide Quicker Detection of Large Methane Emissions*. Dec. 2024.

A

Research plan

This appendix serves to reflect on the research plan of this thesis by evaluating how the plan evolved over time, analyzing deviations from the original timeline, and identifying lessons learned.

At the start of this thesis project, the research plan was centered on answering three research subquestions:

1. What is the methane leak detection threshold of GOES-16 by using TROPOMI reference detections?
2. How do GOES-16's source rate quantifications compare to current quantification methods that only use a single observation?
3. How can methane leaks be detected in GOES' extensive data record without relying on previous LEO-based detections as a reference?

The initial plan focused on using GOES quantifications of TROPOMI reference detections to answer the first and second subquestions, as shown in the original Gantt chart in Figure A.1. Based on supervisor feedback in the fifth month of the thesis, the focus shifted to using simulated plumes in a synthetic environment to verify GOES' retrieval and quantification methodologies with an OSSE. As a result, these simulated plumes were also used to determine GOES' PODs. This was a positive result of the addition of the OSSE to the thesis since the synthetic environment allows for controlled conditions, which was not possible by focusing solely on TROPOMI reference detections.

The OSSE was added to the research plan during the thesis. This lead to two one-month extensions of the thesis, from eleven to thirteen months. In the end, the OSSE and the first subquestion were completed and a first attempt at automated plume detection for subquestion 3 was made. The second subquestion was left as a recommendation for future work.

This thesis has been a valuable learning experience that underscored the importance of stakeholder management, effective planning and thorough literature reviews. The key lessons learned are:

1. Break down complex problems into their elementary constituents and tackle them one at a time.
2. Do not spend time solving problems that do need need to be solved.
3. Clearly define the scope of the research and communicate this with stakeholders
4. Be critical of results and investigate whether they make sense.
5. Small steps lead to big progress.

While this project deviated from the initial plan in several areas, these challenges turned out to be valuable learning experiences. The experiences from this thesis will certainly benefit me in my future career as an engineer or elsewhere.

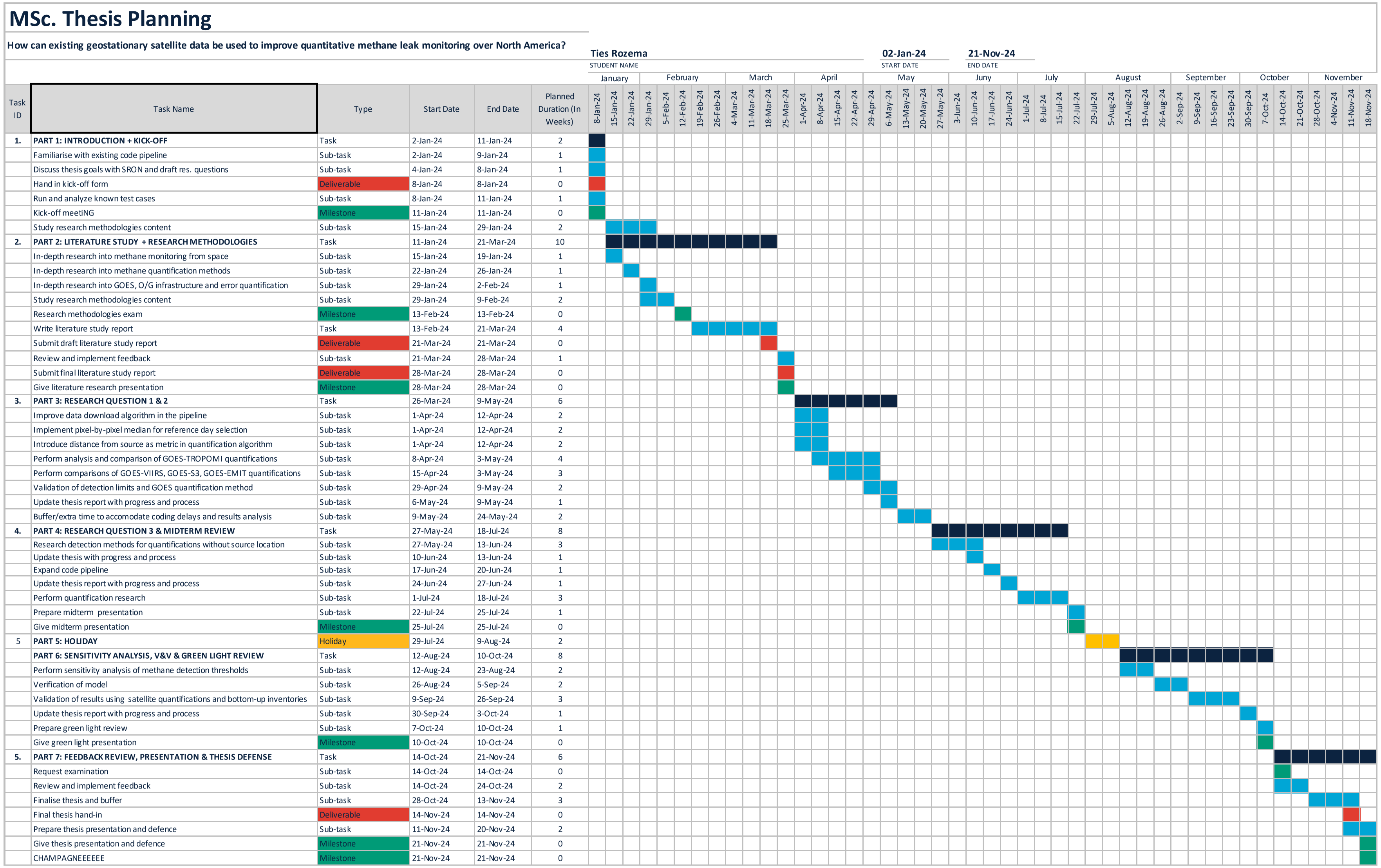

MSc. Thesis Planning

How can existing geostationary satellite data be used to improve quantitative methane leak monitoring over North America?

Ties Rozema
STUDENT NAME

02-Jan-24
START DATE

21-Nov-24
END DATE

Task ID	Task Name	Type	Start Date	End Date	Planned Duration (In Weeks)
1.	**PART 1: INTRODUCTION + KICK-OFF**	Task	2-Jan-24	11-Jan-24	2
	Familiarise with existing code pipeline	Sub-task	2-Jan-24	9-Jan-24	1
	Discuss thesis goals with SRON and draft res. questions	Sub-task	4-Jan-24	8-Jan-24	1
	Hand in kick-off form	Deliverable	8-Jan-24	8-Jan-24	0
	Run and analyze known test cases	Sub-task	8-Jan-24	11-Jan-24	1
	Kick-off meetiNG	Milestone	11-Jan-24	11-Jan-24	0
	Study research methodologies content	Sub-task	15-Jan-24	29-Jan-24	2
2.	**PART 2: LITERATURE STUDY + RESEARCH METHODOLOGIES**	Task	11-Jan-24	21-Mar-24	10
	In-depth research into methane monitoring from space	Sub-task	15-Jan-24	19-Jan-24	1
	In-depth research into methane quantification methods	Sub-task	22-Jan-24	26-Jan-24	1
	In-depth research into GOES, O/G infrastructure and error quantification	Sub-task	29-Jan-24	2-Feb-24	1
	Study research methodologies content	Sub-task	29-Jan-24	9-Feb-24	2
	Research methodologies exam	Milestone	13-Feb-24	13-Feb-24	0
	Write literature study report	Task	13-Feb-24	21-Mar-24	4
	Submit draft literature study report	Deliverable	21-Mar-24	21-Mar-24	0
	Review and implement feedback	Sub-task	21-Mar-24	28-Mar-24	1
	Submit final literature study report	Deliverable	28-Mar-24	28-Mar-24	0
	Give literature research presentation	Milestone	28-Mar-24	28-Mar-24	0
3.	**PART 3: RESEARCH QUESTION 1 & 2**	Task	26-Mar-24	9-May-24	6
	Improve data download algorithm in the pipeline	Sub-task	1-Apr-24	12-Apr-24	2
	Implement pixel-by-pixel median for reference day selection	Sub-task	1-Apr-24	12-Apr-24	2
	Introduce distance from source as metric in quantification algorithm	Sub-task	1-Apr-24	12-Apr-24	2
	Perform analysis and comparison of GOES-TROPOMI quantifications	Sub-task	8-Apr-24	3-May-24	4
	Perform comparisons of GOES-VIIRS, GOES-S3, GOES-EMIT quantifications	Sub-task	15-Apr-24	3-May-24	3
	Validation of detection limits and GOES quantification method	Sub-task	29-Apr-24	9-May-24	2
	Update thesis report with progress and process	Sub-task	6-May-24	9-May-24	1
	Buffer/extra time to accomodate coding delays and results analysis	Sub-task	9-May-24	24-May-24	2
4.	**PART 4: RESEARCH QUESTION 3 & MIDTERM REVIEW**	Task	27-May-24	18-Jul-24	8
	Research detection methods for quantifications without source location	Sub-task	27-May-24	13-Jun-24	3
	Update thesis with progress and process	Sub-task	10-Jun-24	13-Jun-24	1
	Expand code pipeline	Sub-task	17-Jun-24	20-Jun-24	1
	Update thesis report with progress and process	Sub-task	24-Jun-24	27-Jun-24	1
	Perform quantification research	Sub-task	1-Jul-24	18-Jul-24	3
	Prepare midterm presentation	Sub-task	22-Jul-24	25-Jul-24	1
	Give midterm presentation	Milestone	25-Jul-24	25-Jul-24	0
5	**PART 5: HOLIDAY**	Holiday	29-Jul-24	9-Aug-24	2
	PART 6: SENSITIVITY ANALYSIS, V&V & GREEN LIGHT REVIEW	Task	12-Aug-24	10-Oct-24	8
	Perform sensitivity analysis of methane detection thresholds	Sub-task	12-Aug-24	23-Aug-24	2
	Verification of model	Sub-task	26-Aug-24	5-Sep-24	2
	Validation of results using satellite quantifications and bottom-up inventories	Sub-task	9-Sep-24	26-Sep-24	3
	Update thesis report with progress and process	Sub-task	30-Sep-24	3-Oct-24	1
	Prepare green light review	Sub-task	7-Oct-24	10-Oct-24	1
	Give green light presentation	Milestone	10-Oct-24	10-Oct-24	0
5.	**PART 7: FEEDBACK REVIEW, PRESENTATION & THESIS DEFENSE**	Task	14-Oct-24	21-Nov-24	6
	Request examination	Sub-task	14-Oct-24	14-Oct-24	0
	Review and implement feedback	Sub-task	14-Oct-24	24-Oct-24	2
	Finalise thesis and buffer	Sub-task	28-Oct-24	13-Nov-24	3
	Final thesis hand-in	Deliverable	14-Nov-24	14-Nov-24	0
	Prepare thesis presentation and defence	Sub-task	11-Nov-24	20-Nov-24	2
	Give thesis presentation and defence	Milestone	21-Nov-24	21-Nov-24	0
	CHAMPAGNEEEEEE	Milestone	21-Nov-24	21-Nov-24	0

Figure A.1: Original thesis Gantt chart. The original planning was eleven months, which was extended during the thesis to thirteen months.